HADRON-HADRON PRODUCTION AT LARGE TRANSVERSE MOMENTA

A Dissertation Presented

by

Randall Jay Fisk

to

The Graduate School

in Partial Fulfillment of the Requirements

for the Degree of

Doctor of Philosophy

in

Physics

State University of New York

at

Stony Brook

August, 1978

STATE UNIVERSITY OF NEW YORK

AT STONY BROOK

Randall Fisk

We, the dissertation committee for the above candidate for the Ph.D. degree, hereby recommend acceptance of the dissertation.

Robert McCarthy, Advisor

Paul Grannis, Chairman

John Smith

Philip Johnson

The dissertation is accepted by the Graduate School.

SIGNED: _____
Herbert Weisinger, DEAN
The Graduate School

DATE: _____

August 1978

ABSTRACT

We have studied hadron pairs, roughly back to back in the center of momentum frame, produced by the interactions of 400, 300 or 200 GeV protons with a beryllium or tungsten target. The transverse momentum of each hadron was between 1 and 6 GeV/c. We were able to distinguish pions, kaons and protons over most of that range. We measured invariant single and two particle cross sections along with their nucleon number (A) and energy (s) dependence. When the transverse momentum of each hadron exceeded 2.7 GeV/c, our correlation measurements (by exhibiting x_e scaling) strongly suggested that constituent scattering is the dominant process for the production of hadrons in this regime. Correlations between species of hadrons seem to be consistent with the quark-quark scattering model.

ACKNOWLEDGEMENTS

Although my name alone appears on this thesis, credit is due to the many people of our Columbia - Fermilab - Stony Brook collaboration whose combined energies and talents made this experiment a success. Working with each of them was a pleasure and a valuable learning experience.

I would like to thank my thesis advisor, Bob McCarthy, for his helpful suggestions and guidance which spurred me on when problems brought me to a standstill.

At this culmination of my formal education, I look back at my parents' continuous support and their never ceasing faith in my ability. I cannot thank them enough for how much this has helped me.

Finally, I must express my love and gratitude for my wife, Mary, who gave me such understanding, help, and encouragement while I worked on this project. It was she who beautifully typed this thesis.

And there is always thanks in my heart for the Lord, my God, who always gives me more than I ask.

Table of Contents

LIST OF TABLES

LIST OF FIGURES

I. INTRODUCTION

Prior to 1973, observations of hadrons produced by the high energy collisions of nucleons were indicative of a "soft" scattering of diffuse nuclear material. In 1973, the CERN-Columbia-Rockefeller collaboration[1] revealed that the number of hadrons produced with large transverse momenta ($p_\perp \sim 6$ GeV/c) by high energy ($\sqrt{s} = 53$ GeV) PP collisions was $\sim 10^7$ times greater than the extrapolation of the steep exponential decline at low $p_\perp$ characteristic of the soft scattering. The favored theory explaining this abundance of high $p_\perp$ hadrons was the "hard" scattering of point-like constituents of the colliding protons. The primary candidates for these constituents were, of course, quarks. Measurements[2] substantiated the prediction of "jets" which, as shall be discussed shortly, comes from the quark-quark scattering picture. The energy (s) dependence characteristic of the scattering of point-like particles was <u>not</u> observed, however, in the production of single hadrons between $p_\perp = 1$ to 7 GeV/c.[3] Our experiment measured the production

of pairs of hadrons and found indications that constituent scattering is the primary process by which pairs of hadrons are produced when their transverse momenta both exceed ~3 GeV/c.

Our experiment was performed at Fermi National Accelerator Laboratory from June 1976 to February 1977. It was known at Fermilab as E494. We also performed an electron pair experiment (E288) concurrent with our dihadron effort in the hopes of confirming or rejecting a possible e^+e^- resonance at a mass near 6 GeV.[4] The reaction with which this thesis is concerned is

$$P + Be \rightarrow h^{\pm} + h^{\pm} + \text{anything}$$

where h is an unspecified type of hadron. The momenta of the primary protons were 400, 300 or 200 GeV/c. Occasionally we used a tungsten target. The secondary hadrons under study were roughly back to back and 90^{o} from the primary beam direction in the 400 GeV center of momentum (CM) frame. The momenta of our secondaries ranged from 20 to 100 GeV/c (typically ~35 GeV/c) and the transverse momenta from 1 to

6 GeV/c. The masses of the hadron pairs we studied were between 4 and 10 GeV. We were able to distinguish pions, kaons and protons from $p_\perp$ = 2 to 4 GeV/c in each arm and up to dihadron masses of 8 GeV. Of course we searched for massive dihadron resonances, exploring every combination of hadron species, and found none strong enough for us to detect. The resonance search is described in detail in Reference 5.

Since the purpose of this thesis is to present our experimental measurements and show how they support several ramifications of the quark-quark scattering picture, the quark-quark scattering picture will be discussed briefly here.[6] Figure 1 illustrates the collision of a beam proton and target nucleon. In this picture, quarks happen to collide, scattering at 90° in the CM frame. The force between the two scattered quarks, called the gluon field, is thought to increase as the distance between the two quarks becomes large. (This is postulated to explain the non-observation of free quarks yet allow their existence within hadrons.) The strengthening gluon field, then, pulls quark-antiquark pairs out of the vacuum between the two scattered quarks. All of the quarks eventually find antiquark partners to form mesons or join in groups of

three to form baryons. These are the hadrons we detect. Note some interesting predictions of this picture. First, several hadrons may be produced on each side of the interaction. These hadron groups are called jets. Second, jets are produced on opposite sides of the interaction in the quark-quark center of mass frame from two scattered quarks with equal and opposite $p_\perp$. Third, assuming a random selection of which beam quark collides with which target quark, and no correlation between the types of quarks pulled out of the vacuum on one side of the interaction and those on the opposite side, the species of the two detected hadrons are uncorrelated. Our measurements provide a quantitative check of a consequence of the second prediction and a somewhat more qualitative check of the third prediction.

The description of our experiment proceeds in an orderly fashion starting with the apparatus, the data, backgrounds, single hadron production measurements and finally hadron pair measurements.

II. THE APPARATUS

II. A. Beam and Targets

Protons were accelerated to energies of 200, 300 or 400 GeV, slowly extracted from the synchrotron and sent to our experiment at the Proton Central Laboratory at Fermilab. We controlled the final steering and focusing of the beam. The beam position was monitored by separated wire ionization chambers and the intensity of each pulse was monitored by both a secondary emission monitor (SEM) and an ionization chamber. We used beam intensities between 2×10^9 and 3×10^{10} protons per pulse. Typically a pulse lasted 1 second and was repeated every 10 seconds. The protons were bunched into "rf buckets" as a result of the rf accelerating voltage in the synchrotron being left on during extraction. Each bucket was less than a nanosecond long and was separated from neighboring buckets by 18.9 nsec. Our "resolving time", the time interval between two particles detected by our apparatus needed to rule out their simultaneity, was less than 18.9 nsec, so essentially it was one rf bucket. We placed a small freon filled Cerenkov counter (SB) in the beam line to tell us the population of each and every bucket. (SB is the acronym for "super bucket", an unusually heavily populated rf bucket, which,

as we shall see later, contributes substantially to dihadron background.)

The calibration of SEM to the number of beam protons was carried out by proton lab personnel who placed a copper foil in the beam line and passed a fixed amount of beam through it as measured by the SEM. High energy protons (>400 MeV) convert Cu atoms to ^{24}Na and ^{52}Mn with a known cross section (3.5 and 4.0 mb per Cu nucleus[7]), so the measurement of the amount of ^{24}Na and ^{52}Mn in the copper indicated how many protons actually passed through the foil. The calibration constant was found to be

$$\frac{\#\ \text{protons}}{\text{SEM}} = 1.01 \times 10^{8}$$

This measurement was performed several times showing the stability of this constant to be $\sim \pm 2\%$. [Another Cu $\rightarrow$ ^{24}Na or ^{52}Mn cross section measurement was recently made at Fermilab by S. Baker et al. The results (as yet unpublished) were 3.8 mb for ^{24}Na and 4.6 mb for ^{52}Mn production. If these values were used, our cross sections would increase by $\sim$10%. In order to maintain continuity with earlier Fermilab experiments, however, we will use 3.5 and 4.0 mb.]

We could move one of three targets into the beam: two beryllium targets which differed only in width (Be 7 and Be 3) and

one tungsten target (W). The widths of the Be 7 and W targets were of the order of the beam width (~0.04 cm), intercepting ~70% and ~95% of the beam respectively. The Be 3 target was wide enough to insure the entire beam was incident upon it. The target heights were much larger than the vertical spread of the beam (<0.1 cm). Properties of the targets are given in Table I. We will find it useful to calculate the ratio of interacting protons to incident protons using

$$\frac{\text{\# int. protons}}{\text{\# inc. protons}} = 1 - e^{-L/\lambda}$$

where L is the target length and λ is the absorption length. We will also need the effective target length, the average length of target encountered by unabsorbed beam, which is given by

$$L_{eff} = \lambda(1 - e^{-L/\lambda})$$

The number of protons interacting in the target was monitored by a scintillation telescope (N) located in the beam of neutral particles in one arm of our experiment. Figure 2, showing N/SEM vs. the distance from the beam to the target centers, confirms our knowledge of beam and target widths. Note that without a target N/SEM = 1.1, so that with a target more than 98.5% of N comes from the target. Because the

entire primary beam could be incident upon Be 3, the ratio N/SEM gave us Be 3' s N calibration: the number of N' s per proton incident upon the target. Since the ratios of N to incident protons for Be 7 and Be 3 were necessarily equal, the Be 3 calibration was used for Be 7. Figure 3 shows the stability of the N calibration constant as a function of time. We see no significant time dependence. N was placed in the neutral beam so that its calibration would be independent of analyzing magnet current. Figure 3 confirms this to the ±5% level. The dependence of N on beam intensity was also investigated (Fig. 4) and was found to be quite linear up to intensities much larger than we used. There was no wide tungsten target because, unlike Be 3, the absorption of secondaries near 90^{o} CM for such a target would not be negligible. The W calibration, then, had to be calculated from W target scans like that of Fig. 2. Integrating N/SEM with respect to the beam to target distance expressed in target widths should give a value equal to what N/SEM would be if the target were infinitely thick (but without secondary absorption). The integrals of the curves of Fig. 2 are 109, 105 and 80.5 for Be 3, Be 7 and W respectively. Note the values for Be 3 and Be 7 are very close to each other

and to the standard Be 3 calibrations. This and the fact the ratio of the peak value of N/SEM to the area is just under 1 (~ 95%), as one would expect from the target and beam widths, gives us confidence in the N calibration for W. Figure 3 shows the repeatability of the measurement. From this figure we obtain the final values of the N calibration constants and their errors for all our targets, which are listed in Table II.

Table II also gives values for two constants, C_{XS} and C_R, which will be used in cross section and correlation function calculations later. I define them as

$$C_{XS} \equiv \frac{N}{\#\text{ inc. protons}} \quad \frac{A}{\rho N_o L_{eff}}$$

$$C_R \equiv \frac{\#\text{ int. protons}}{N}$$

where A (the number of nucleons), ρ (the density), L_{eff} (the effective target length) and the ratio of interacting protons to incident protons are all found in Table I. N_o is Avagadro's number. Note that the product of C_{XS} and C_R reduces to

$$C_{XS}\ C_R = \frac{A}{\rho N_o \lambda}$$

$$= \sigma_{inel}$$

where λ is the absorption length and therefore σ_{inel} is the inelastic cross section.

II. B. Collimators, Magnets and Acceptances

The upstream portion of the apparatus is shown in Fig. 5. After their creation in the target, secondaries in each arm passed through a 5 m deep collimator made of steel and tungsten. Downstream of this collimator was a 5 cm deep tungsten collimator installed to define the aperture for the concurrent dielectron experiment. In our analysis computer program, hadrons were required to be well within the acceptance imposed by these collimators. The fiducial volume used in our final analysis is completely described by Table III. The angles θ_x and θ_y are relative to the primary beam direction. Positive x and θ_x point in a horizontal plane away from the primary beam line while positive y and θ_y point up in the up arm and down in the down arm. (The up and down arms will be defined shortly.) The distance from the target, z, is measured along a line described by $\theta_x = 0.0725$ radians, $\theta_y = 0.$ We measured x and y relative to this line. Our openings in θ_x and θ_y correspond to the acceptance in azimuthal angle ϕ and center of mass polar angle θ shown in Fig. 6. Note the wide acceptance in θ_{CM} ($90^o \pm 20^o$) compared to the narrow slit in ϕ ($\Delta\phi \sim 7^o$). Ranges in θ_{CM} for the three beam energies

are listed in Table IV and were calculated using $\tan \frac{\theta_{CM}}{2} = \gamma_{CM} \tan \theta_{LAB}$ [γ_{CM} = (1 - velocity of CM frame^2/speed of light^2)$^{-\frac{1}{2}}$], which is valid for β (the velocity of the secondary divided by the speed of light) near 1. These correspond to the ranges in rapidity, $y = \frac{1}{2} \ell n \frac{E + p_{\parallel}}{E - p_{\parallel}} \overset{\beta \to 1}{=} -\ell n \tan \frac{\theta}{2}$, where $p_{\parallel}$ is the parallel momentum and E is the energy of the secondary, also given in Table IV. Note Δy is only 0.67.

After the collimators, particles passed through the horizontal fields of the analyzing magnets, one in each arm. The pole faces were 3.05 m long, 25 cm high and tapered from 45 to 60 cm apart. Charged particles were bent vertically, thus decoupling the measurements of momentum and production angle. Looking downstream, the left arm of the apparatus only accepted particles bent up out of the neutral beam and was therefore called the up arm (UP). The right arm looked at charged particles bent downward and was called the down arm (DN). The two magnets were connected in series so that the currents through them were always equal. The polarities of the magnets, however, could be varied independently. Most of our data were taken at magnet currents of 1288 and 961 amps. The

corresponding integral fields were 34.8 and 25.8 kG-meters, imposing $p_\perp$ kicks of 1.043 and 0.774 GeV/c respectively. Both the current and the field at one point in each magnet were continuously monitored and found to be stable within $\pm 0.1\%$. Small variations ($\pm 1\%$) in field strength vs. x and y were taken into account in the analysis after being measured with a long and narrow flip coil.

The aperture downstream of the magnets is described in Table III and is illustrated in Fig. 7. This geometry dictates what the vertical acceptance ($\Delta\theta_y$) as a function of momentum must be, the result of which (for the up arm) is shown in Fig. 8. At low momenta, particles are bent out of the downstream aperture. At intermediate momenta, the vertical acceptance is determined by limits on θ_y. At high momenta the acceptance falls due to insufficient magnetic field to sweep high momentum particles out of the neutral beam.

To calculate the single arm acceptance as a function of $p_\perp$, we must know how hadrons are distributed in θ. This information comes from the approximation that at fixed $p_\perp$, single hadron production is independent of rapidity y when y is small. Since $dy \overset{\beta \to 1}{=} \frac{-d\theta}{\sin\theta}$, the number of hadrons produced

per unit range in θ at constant $p_\perp$ is proportional to $\frac{1}{\sin\theta}$. Based on this, a Monte Carlo program produced our acceptance vs. $p_\perp$ shown (for the up arm) in Fig. 9. Its error is estimated to be ± 0.003. Because we will express our results in terms of the single hadron invariant cross section,

$$E\frac{d^3\sigma}{dp^3} = \frac{1}{p_\perp}\frac{d^3\sigma}{d\phi\, dy\, dp_\perp}$$

we defined our acceptance as the integral over our fiducial volume: $\int d\phi\, dy$. This integral is Lorentz invariant and therefore can be evaluated in the CM or lab system. Also its value is independent of beam energy. (However the mean rapidity is energy dependent.) Since $\int d\phi\, dy \overset{\beta\to 1}{=} \int \frac{d\Omega}{\sin^2\theta}$ (where Ω is the solid angle), in the 400 GeV CM frame where $\theta \sim 90^\circ$ our acceptance is approximately equal to the CM solid angle.

To determine the acceptance for pairs, we must ask if the observation of a hadron on one side of the interaction affects our assumptions of flat distributions in y and ϕ over our acceptance in the opposite arm. The answer is approximately no over our small ranges in y and ϕ.[8] Hence the pair acceptance for $E_1 E_2 \frac{d^6\sigma}{dp_1^3\, dp_2^3}$, $\int\int d\phi_1\, dy_1\, d\phi_2\, dy_2$, is simply the product of our two single arm acceptances.

II. C. Scintillation Counters and Primary Trigger T

Figure 10 shows the apparatus used to detect the secondaries we have been discussing. The first alert to the possible presence of such a secondary came from the scintillation counters T0, T1 and S2. These were made of 1/4 inch scintillation material (Pilot Y), the geometry of which is shown in Fig. 11. From each counter element we derived an on-off signal and from these signals we created our primary trigger T. First we combined signals from the elements of T0 and T1 including only those $T0_i\ T1_j$ pairs which lined up with the exit of the analyzing magnet:

$$\begin{aligned} T0 * T1 = \; & T0_1 \cdot (T1_1 + T1_5) \\ & + T0_2 \cdot (T1_1 + T1_5 + T1_2 + T1_6) \\ & + T0_3 \cdot (T1_2 + T1_6 + T1_3 + T1_7) \\ & + T0_4 \cdot (T1_3 + T1_7 + T1_4 + T1_8) \\ & + T0_5 \cdot (T1_4 + T1_8) \end{aligned}$$

Finally we required that any S2 element fired. Hence

$$T = T0 * T1 \cdot S2$$

Our primary pair trigger was TUD, the coincidence of the up arm T (TU) and the down arm T (TD). Specific details of our triggering system will be discussed in Section IV. A.

Occasionally T was not on when a desirable secondary was actually present. To measure its inefficiency, we used an independent trigger based upon the requirement that both Cerenkov counters in one arm fired. Imposing very stringent track quality requirements (in order to be as sure as possible that a desirable secondary really was present), we measured the inefficiencies of TU and TD given in Table V. The inefficiencies were found to be dependent on the intensity of the beam and the mass ranges of Table V correspond to the different running conditions needed to best study the 4-5, 5-6 and 6-10 GeV regions of the mass spectra. In general, the higher the mass region, the higher the beam intensity. (See Table XV for specifics.)

Based upon information regarding the position of a secondary in our apparatus, the analysis computer program tried to reconstruct its track. After a possible track was found, the correct T1 element was required to have been on. The scintillation hodoscopes V1 and V2 were also required for track reconstruction. They were composed of 38 and 55 tall, narrow counters standing vertically side by side, thus giving fair resolution in θ_x. Starting with $V1_1$ on the small x side, their geometry is described as follows:

V1 (z = 2456 cm)

elements	1-16:	1.94 cm wide, 1/8 inch thick
	17-34:	3.57 cm wide, 1/4 inch thick
	35-38:	5.12 cm wide, 1/4 inch thick

V2 (z = 3562 cm)

elements	1-24:	2.19 cm wide, 1/4 inch thick
	25-48:	3.56 cm wide, 1/4 inch thick
	49-55:	5.11 cm wide, 1/4 inch thick

The inefficiencies of the T1 and V1-V2 requirements in track reconstruction were measured using T triggers and high quality tracks. The results are also in Table V.

The overall scintillation counter efficiencies, the products of the previously mentioned efficiencies, are given in Table V. The errors of these measurements are estimated to be ~15% of the inefficiencies, due to changes during the five-month running period. The efficiencies of the individual elements of V1 or V2 were roughly the same, with only one ($V2_{12}$ up) showing an inefficiency (~10%) much higher than the rest. Similarly, the trigger counter efficiencies were fairly constant across the aperture, the only exception being $T1_8$ up which contributed ~5% more to the T inefficiency in its region of the aperture than the rest.

The V1 and V2 hodoscopes were also used by our high $p_\perp$ trigger. For now, all we need know about the high $p_\perp$ trigger is that it used information in the form of whether or not a track existed in each of four regions in θ_x (θ_1, θ_2, θ_3, θ_4). The first step towards the accomplishment of this was the grouping (the logical OR of the signals) of the V1 elements into 10 groups of 4 and the V2 elements into 14 groups of 4. Each V2 group was then combined (logical AND) with every V1 group in line with it and the target. These 14 V2 * V1 groups were then grouped into categories consisting of 4, 4, 3 and 3 V2 * V1 groups. These 4 categories correspond to θ_1, θ_2, θ_3 and θ_4 respectively and have the following angular bounds.

θ_1 : θ_x = 48.5 to 58.5 mrad

θ_2 : 58.5 to 71.4 mrad

θ_3 : 71.4 to 83.4 mrad

θ_4 : 83.4 to 94.5 mrad

Another signal derived from the V1's and V2's was the multi-track indicator (M1). M1 was on if more than one V2 * V1 group per arm were on. Its effect will be discussed in Section IV. A.

II. D. Wire Chambers, Reconstruction and Resolution

Nine wire chambers in each arm were located as shown in Fig. 10. The directions and spacings of the signal wires are given in Table VI . These wires were gold plated tungsten 20 or 30 microns in diameter. Each chamber consisted of a plane of signal wires sandwiched between two planes of vertical high voltage wires which were 100 microns in diameter and spaced at 1 mm intervals. Outside these three planes were Aclar windows used to contain the 83% argon, 17% CO_2 gas. A trace (0.1%) of freon 13 B 1 was added to this mixture to inhibit wire breakage. Outside the windows were two planes of aluminum window screen which were grounded to prevent spurious radio-frequency pickup.

Knowing which wires of each chamber were activated, the path of a particle could be reconstructed. In our analysis program, this reconstruction began by requiring that of the three chambers at station 1 (1Q, 1P, 1Y), two contained activated wires. A pair of these activated wires from two different chambers corresponds to an x-y coordinate at station 1. Similarly, two out of 3Q, 3P and 3Y were required to have activated wires. By pairing coordinates from station 1 and station 3, we determined the possible trajectories of particles. Each possibility

was accepted or rejected by requiring that the correct T1, V1 and V2 elements be on and that the correct wires of 2Y or JY and of at least 7 of the 9 chambers be activated.

The efficiency of each chamber was measured with high quality tracks (which included the requirement that all other wire chambers were hit) and is presented in Table VII. From the previously described reconstruction formula, the overall wire chamber efficiencies were calculated and are also given in Table VII.

The resolution in momentum, $p_\perp$, mass and other variables was determined by the wire spacings and locations in z of the wire chambers and by the effects of multiple scattering. The mean square angular deviation, $d\langle\theta^2\rangle$, imparted by multiple scattering from a length of material dX is approximately[9]

$$d\langle\theta\rangle^2 = \left(\frac{0.015}{p}\right)^2 \frac{dX}{L_R}$$

where p is the momentum in GeV/c and L_R is the radiation length. The radiation lengths for all materials in the secondary beam are listed in Table VIII. Figure 12 shows our overall momentum resolution (expressed as a standard deviation σ_p) and the contribution of multiple scattering. The overall resolution in production angle is

$$\sigma_{\theta_x} = 0.18 \text{ mrad}$$

$$\sigma_{\theta_y} = 0.16 \text{ mrad}$$

The $p_\perp$ and mass resolutions are shown in Fig. 13. When the tungsten target was in use, the additional ~1 radiation length through which secondary particles passed added only 0.015 GeV/c in quadrature to $\sigma_{p_\perp}$. Because of the concurrent di-electron experiment, we were able to verify our resolution calculations by the observation of the J/ψ decay into electron pairs. At an analyzing magnet current of 961 amps, the acceptance in mass included the J/ψ region. The measured dielectron mass spectrum is shown in Fig. 14 along with a Gaussian distribution of standard deviation equal to our expected resolution. It can be seen that the width of the J/ψ peak is indeed consistent with our calculated resolution.

II. E. Cerenkov Counters and Particle Identification

We were able to distinguish pions, kaons and protons through the use of two Cerenkov counters in each arm (see Fig. 10). Each Cerenkov counter was a light-tight, gas-tight box enclosing the aperture. C1 was filled with helium and C2 with a neon-nitrogen mixture. Both gases were at just above atmospheric pressure in order to use thin windows and reduce cost. Each counter contained three mirrors which reflected the Cerenkov light onto three corresponding phototubes. The mirrors were side by side with the following widths (starting at the small x side:

C1 (mirrors at z = 2324 cm:
734 cm from the entrance window)
mirror 1: 35 cm wide
2: 48 cm
3: 48 cm

C2 (mirrors at z = 2915 cm:
422 cm from the entrance window)
mirror 1: 39 cm wide
2: 39 cm
3: 78 cm

The C1 phototubes were 2 inch RCA C3100M quantacons while those in C2 were 5 inch Amperex 58 DVP's with wavelength-

shifter coatings over their faces. Details of the design and construction of the Cerenkov counters are presented in the Appendix.

Cerenkov light is produced whenever a charged particle exceeds the local speed of light (c/n, where n is the index of refraction and c is the speed of light in vacuum). Hence the threshold momentum (p_{th}) above which light is produced from a charged particle of rest mass m_o is

$$p_{th} = \frac{m_o c}{\sqrt{n^2 - 1}}$$

The efficiency of a Cerenkov counter depends on the amount of light each particle produces. The pertinent quantity is the number of electrons knocked off the phototube face by the Cerenkov light. The average number of these photoelectrons (APE) is given by [10]

$$APE = N_o L \sin^2\theta_c$$

where N_o is a constant depending on the type and quality of the phototube, L is the path length of the particle emitting Cerenkov light and θ_c is the Cerenkov angle which is given by $\cos\theta_c = \frac{1}{\beta n}$ (where β is the particle's velocity divided by c). Equivalently,

$$APE = N_o L \left(1 - \frac{1}{n^2}\right) \left(1 - \frac{p_{th}^2}{p^2}\right)$$

For particles of a given velocity, the actual number of photoelectrons is described by a Poisson distribution. Hence the inefficiency $(1 - \epsilon)$, or fraction of times Cerenkov light produces no photoelectrons, is

$$1 - \epsilon = e^{-APE}$$

N_o was measured at a test beam where a very pure sample of particles guaranteed to produce maximum Cerenkov light (i. e. $p >> p_{th}$) could be obtained. This guarantee was made possible by an additional Cerenkov counter whose gas was under partial vacuum so that only very fast particles would be detected. The results were:

$$C1: \quad N_o = 185 \pm 5$$

$$C2: \quad N_o = 150 \pm 20$$

In our calculations, however, we used more conservative values for N_o: 150 for C1 and 100 for C2.

Even with gases of the lowest indices of refraction used in our experiment, the average numbers of photoelectrons were 8.2 for C1 and 11.2 for C2, which correspond to inefficiencies of 0.03% and 0.001% respectively. Inefficient light collection, faulty electronics and other problems could be additional sources of inefficiencies. Hence we measured the Cerenkov inefficiencies

directly as best we could. Since electrons traveled much faster than their Cerenkov thresholds in our experiment, we sought as pure a sample of electrons as possible. The e/π production ratio, normally 10^{-4} for PP collisions, was enhanced by a factor of 400 by allowing π^{o}'s to produce $e^{+}e^{-}$ pairs in a thick aluminum target. The best hadron rejection possible by the lead glass calorimeter increased e/π of our data sample by a factor of 1300. Since the remaining few percent of hadrons in our electron sample could not be eliminated, requirements were made so most of these hadrons would be above their threshold velocities. Specifically, the sample used to measure the efficiency of C1 had momenta exceeding 20 GeV/c so that most of the pions would be above threshold. The C2 sample was made up of events with C1 on, so that every particle of this data sample (except those included only because C1 accidentally was on) had a velocity greater than the threshold velocity of C2. The measured inefficiencies are presented in Table IX. Note that with the possible exception of C2 up (whose larger than average inefficiency arose from a measured 0.2% inefficiency of the small angle phototube), the measured inefficiencies are consistent with the contamination of our sample of electrons.

The most serious problem with the Cerenkov counters was that they were occasionally on when they should not have been. This was due to stray particles which were fast enough to produce Cerenkov light but did not come directly from the target and usually transversed only part of the apparatus. When a legitimate secondary was accompanied by one of these fast strays, unless the stray was incident upon a different mirror than the mirror traversed by the legitimate track, it was impossible to tell whether the stray or the legitimate particle produced whatever Cerenkov light was detected. It was possible to measure the extent of this effect by looking at mirrors not traversed by legitimate tracks and observing how often the phototubes were on. The results, of course, were intensity dependent, so measurements using the running conditions corresponding to each mass range are presented in Table IX . It was observed that most of the C1 and C2 accidental hits were uncorrelated.

The gases within the Cerenkov counters were chosen so that the momenta at which particle identification was possible covered the desired regions. The C1 gas never varied, but the C2 gas was changed according to the region of the mass spectrum under study. The gases and corresponding indices of refraction

are presented in Table X. The indices of refraction were measured directly with an interferometer. Details of this measurement and device are presented in the Appendix.

Threshold momenta for pions, kaons and protons are illustrated in Fig. 15. Comparisons of the thresholds calculated using our measured indices of refraction to the directly observed momentum thresholds are shown in Fig. 16. The top graph shows the measured C1 efficiency vs. momentum for pions identified by the requirement that C2 be on. (The apparent decrease in the efficiency of C1 when $p > 20$ GeV/c is actually due to kaons beginning to produce light in C2 and thus contaminate the pion sample.) Indeed pions began to produce light very near their expected momentum threshold. (The expected threshold appears a little too high. As will be discussed in the Appendix, lowered values were used in the analysis.) The bottom graph shows the measured efficiency of C2 vs. momentum for kaons and antiprotons, identified by requiring C1 be off. The kaon threshold is evident and in about the right place. (The non-zero C2 efficiency below kaon threshold is caused by accidental hits in C2 and pion contamination through accidental hits in C1. As one would expect, the efficiency at high momenta levels off to about 67%, the K^- to K^- plus $\overline{P}$ ratio.)

We were able to distinguish pions, kaons and protons at momenta where the Cerenkov responses were expected to be

π : C1 on, C2 on
K: C1 off, C2 on
P: C1 off, C2 off

(By "on", we mean the probability of on being greater than 95%.) This region in momentum we call the triple identification band (3-ID) and is illustrated in Fig. 15. Note that for our experiment the bounds of this region depended only on the C2 gas mixture. [As shown in Fig. 15, we restricted the 3-ID region so that even though the C2 gas mixture varied slightly ($\pm 10\%$ in n - 1) the 3-ID boundaries were defined to remain constant in time.] We also used the pion identification band (π-ID), the region in momentum where the Cerenkov responses were expected to be

π : C1 on, C2 on
K or P: C1 off, C2 on or off

The π-ID region is also illustrated in Fig. 15 and, as one would expect, depended only on the C1 gas. The acceptances in single arm $p_\perp$, defined in the same way as those of Fig. 9 but restricting momenta to these regions, are shown in Fig. 17. It should be noted that particle identification outside these regions is possible. For example, if a particle with

momentum slightly above proton threshold in C2 were to fire neither C1 nor C2, it could only be a proton. (See Fig. 15.) At this momentum, however, protons in general may or may not fire C2, so that not all protons can be identified in this way. This is an example of conditional particle identification. All particle identification outside the 3-ID band (except pion identification within the π-ID band), however, was ignored.

Definitions of C1 and C2 actually being on (from their phototube signals) were made and then modified to reduce the effects of accidental hits yet not significantly increase the inefficiencies of the Cerenkov counters. The following discussion may be clarified by Fig. 18 where events in the triple identification region are plotted on a C1 pulse height vs. C2 pulse height scatter plot. C1 was defined to be on when its signal exceeded 0.2 photoelectrons (PE). C2 was on when its signal was greater than 0.3 PE. When C2 was off (which should have implied C1 was also off), C1 on was redefined as > 1.0 PE. For positive particles and C1 off, C2 on was redefined as > 0.7 PE. (The increased inefficiency due to this redefinition merely sent more K^+ into the large P^+ data sample.)

Fortunately, the effects of Cerenkov accidentals were to cause rare species (protons and kaons) to contaminate larger species samples (kaons and protons). The species compositions of the secondaries in our apparatus were roughly

$$\pi^+ : K^+ : P^+ = 10 : 3\tfrac{1}{2} : 4$$

$$\pi^- : K^- : \overline{P} = 10 : 2 : 1$$

From these ratios, Table IX and approximate inefficiencies (for which the momentum dependence of APE was taken into account), we calculated the losses and contaminations of the π, K and P data samples given in Table XI. These values are accurate to about $\pm$ 25% of themselves.

II. F. Lead Glass and Water Calorimeters

The momentum of each secondary was measured a second time with our lead glass and water calorimeters. The lead glass array, present for electron identification in the concurrent di-electron experiment, is shown in Fig. 19. The water calorimeter, a novel device, was selected because of its low cost yet adequate energy resolution. It was basically a tank of ultra-pure water 244 cm deep, 305 cm wide and 549 cm long (the down arm calorimeter was somewhat smaller: 244 x 305 x 320 cm^3) with air gap mirrors on the sides and bottom. Wavelength shifter-doped acrylic panels at the downstream end sent light to RCA 8575 phototubes above. It is shown in detail in Fig. 20.[11]

Our calorimeters measured the energy of a hadron in the following way. When a hadron entered the calorimeters it soon collided with a nucleus producing many energetic hadrons (typically 6). These hadrons, in turn, collided with other nucleii producing even more energetic hadrons. This process is known as a hadronic shower. The typical length between collisions is the absorption length which is given for the components of the calorimeters in Table XII. Both calorimeters worked by detecting Cerenkov light produced by the shower hadrons

(including the initial hadron). The energy of the incoming hadron, distributed to shower hadrons upon collisions, was continuously lost to the surrounding media through ionization energy transfer. The total amount of energy lost in this fashion was a large, fairly constant fraction of the initial energy of the hadron and was proportional to the sum of the path lengths of the charged hadrons associated with the shower. Table XII lists these energy losses per particle-cm ($\left|\frac{dE}{dX}\right|_{min}$). Since the total amount of Cerenkov light detected was also proportional (with the exceptions discussed below) to the sum of the path lengths of the shower hadrons, the total Cerenkov radiation was proportional to the energy of the incoming hadron. There were problems with this type of hadron calorimeter, however, which made even the best possible energy resolution relatively poor. First, hadrons stopped giving off Cerenkov light while they still had large amounts of energy (see Table XIII). This problem was amplified by the fact that a hadron-nucleus collision produced many low energy hadrons. As seen in Table XIII, another problem was the different behavior of each species of shower hadron. Neutral pions were the worst offender in this regard, because they readily decayed into two photons which often created

electron-positron pairs which, in turn, initiated electromagnetic showers producing a great deal of Cerenkov light. A problem concerning the water calorimeter was that the Cerenkov light passed through 1 to 3 (light) absorption lengths of water before being collected, the amount of light absorbed depending on the location of the shower in the calorimeter. The problem of some shower hadrons making it through and out of the calorimeters was small. The amount of energy contained by the calorimeters was estimated to be 99% for the up arm and 91% for the down arm.[12]

The performance of the calorimeters is shown in Fig. 21. Here events are histogrammed according to their energy as measured by the calorimeters (E_{cal}) divided by their momentum as measured with the magnetic spectrometer (p). The scale was arbitrarily set so that $\langle E_{cal}/p \rangle \cong 1$. Excluding the low E_{cal}/p spike, FWHM = 0.80 $\langle E_{cal}/p \rangle$. The low E_{cal}/p spike is due in part to muons but mostly to particles which did not come directly from the target (but, for example, scattered off magnet pole faces) and thus fooled our magnetic spectrometer. This demonstrates a very important function of the calorimeter: it eliminated these "fakes" from the data

sample. We decided to only accept events with $E_{cal}/p > 0.35$. Figure 21 shows this cut eliminated most of the fakes yet only 1.0% of the good events in each arm. Exactly how many fakes remained with the good events after passing this cut will be discussed in the section on backgrounds.

The linearity of E_{cal} with the hadron's actual energy p is shown in Fig. 22. The histogram corresponding to high momenta is seen to be peaked at a slightly higher E_{cal}/p and has slightly better resolution than the low momenta histogram. This is the expected behavior because the larger the hadron's momentum, the larger the fraction of energy lost before the velocities of the shower hadrons were less than their Cerenkov thresholds.

It was observed that E_{cal} was dependent on the species of the incoming hadron. E_{cal}/p histograms for pions, kaons, protons and antiprotons are presented in Fig. 22. No differences between the E_{cal}/p curves of π^+ and π^- or of K^+ and K^- were observed. The species dependence of E_{cal} may be due to differences in the species compositions of the corresponding hadronic showers. Note that the difference between the pion and kaon curves is the large number of pions with high E_{cal}/p.

Perhaps more π^o's were produced early in the showers initiated by pions. The larger E_{cal} for antiprotons compared to protons may be due in part to the energy released in the $\overline{P}$'s eventual annihilation.

The lead glass and water calorimeter signals were digitized separately and mixed in the computer analysis program to attain the best energy resolution. This same mix was used to electronically combine the outputs of the two calorimeters. This signal, whose pulse height was proportional to E_{cal}, was the momentum input to the high $p_\perp$ trigger which will be discussed in the next section.

III. HIGH $p_\perp$ AND HIGH MASS TRIGGERS

Because we wished to study large $p_\perp$ hadrons and high mass hadron pairs, we needed a trigger to suppress the enormous number of low $p_\perp$ single arm events and low mass pair events. This we did by constructing signals with pulse heights proportional to $p_\perp$ or mass. Only if one of these signals exceeded a preset threshold voltage might the event be recorded on tape.

Our single arm $p_\perp$ trigger was based upon the equation $p_\perp = p \cdot \theta$. A signal proportional to momentum (p) came from the calorimeters, as described in the last section. The angular (θ) information for each arm was four bits, each of which was on if a track was detected in the corresponding angular region. This was described in detail in Section II. C. Before the angle bits were used by the trigger, each bit was vetoed by the presence of a larger angle bit so that at most one bit was on at a time. We multiplied p by θ by passing the calorimeter signal through one of four attenuators according to which angle bit was on. The attenuators reduced the pulse height by a factor of $< \theta_i > / < \theta_4 >$, where $< \theta_i >$ was the mean angle corresponding to the $i^{\underline{th}}$ angle bit, θ_4 being the largest angle. The result was

a signal approximately proportional to $p_\perp$, which turned on a bit (PT) when it exceeded a preset voltage. The trigger is diagramed in Fig. 24.

Our mass trigger was based upon the following series of approximations. (Θ is the angle between the two secondaries.)

$$m^2 = m_1^2 + m_2^2 + 2(E_1 E_2 - p_1 p_2 \cos\Theta)$$

$$\simeq 4 p_1 p_2 \sin^2\frac{\Theta}{2} \quad (\text{for } m_1, m_2 << m)$$

$$\simeq 4 p_{\perp 1} p_{\perp 2} \quad (\text{good within 0 to -5\% for this experiment})$$

$$= m'^2 - P'^2_\perp \quad \text{where } m' \equiv p_{\perp 1} + p_{\perp 2}$$

$$\simeq m'^2 \qquad\qquad P'_\perp \equiv p_{\perp 1} - p_{\perp 2}$$

Hence summing the two signals proportional to $p_{\perp up}$ and $p_{\perp dn}$ gave us a signal whose pulse height was approximately proportional to mass. As shown in Fig. 24, the mass signal set bits if it exceeded a high threshold voltage (MH) or a somewhat lower threshold voltage (MM).

The efficiency curves of the PT and MH triggers were measured directly using scintillation counter (T) triggered data, but the statistics were insufficient to accurately determine the

curves over their entire ranges. Knowing the shapes of the E_{cal}/p distributions, however, allowed us to simulate the PT and MH triggers in our Monte Carlo program, giving us high statistics efficiency curves. These curves are shown in Fig. 25 together with the directly measured efficiencies. One parameter, relating the pulse height of the $p_\perp$ (or m') signal in mV to an actual $p_\perp$ (or m') in GeV/c, was adjusted so that the simulated curves agreed with the measured efficiencies as well as possible. The Monte Carlo simulation indicated the efficiency curves scaled in the ratio of $p_\perp$ or m' (measured with our magnetic spectrometer) to threshold voltage. This, as one can see by comparing efficiencies using different thresholds, is verified by our direct measurements.

The threshold voltages were chosen according to the region of the mass spectra under study. Table XIV shows these voltages and the corresponding trigger efficiencies. Note the regions in $p_\perp$ and m' under study correspond to efficiencies of typically 70%.

The species dependent behavior of the calorimeters led to species dependent trigger efficiency curves. PT efficiency curves for the different types of hadrons are shown in Fig. 26.

This behavior was also evident from directly measured trigger efficiencies. The species dependence of the efficiency curves was, of course, taken into account in the analysis.

Our high $p_\perp$ and mass triggers were not, unfortunately, always trouble-free. The gain of the water calorimeter photo-tubes drifted during the course of the experiment, the effect of which was equivalent to the threshold voltages varying $\pm 7\%$. This we took into account in our data analysis. For a portion of our running, a power supply partially failed rendering our PT and MH triggers dead $\sim 30\%$ of the time. The dead time, however, was constant and was accurately measured, making this data useful.

The estimated errors associated with the PT and MH efficiency curves are represented by a shift in $p_\perp$ or m' of $\pm 4\%$. This for example, corresponds to an error in the PT curve of $\pm 5\%$ of 70% efficiency.

IV. THE DATA

IV. A. Rates and Data Acquisition

Detected particle and trigger rates, normalized to a one second pulse, are presented in Table XV. In actuality, the spill length varied from 0.8 to 1.3 seconds. At a typical intensity of 2×10^{10} incoming protons per pulse, the detected particle rate (singles rate) of each scintillation counter or wire chamber plane was on the order of 5 MHz. The JY and JV wire chambers, being so close to the analyzing magnet, had singles rates 3 or 4 times higher. The entire experiment was capable of handling two or three times more intensity than we used with no ill effects.

Several signals vetoed all counters in the experiment (including all triggers and our neutrals counter N), effectively turning the entire experiment off in their presence. One of these, the spike killer, turned off data taking when the intensity, averaged over an $\sim 10^{-5}$ second interval, exceeded a preset limit. Another signal killed the experiment whenever the intensity of an individual rf bucket was too large. This "super bucket" signal (SB) was described in Section II. A. After each trigger, slow trigger logic and the computer both took a certain amount of time

to process information before they were ready to handle another trigger. During this time a signal was on which stopped further data collection. The dead times associated with these signals are also listed in Table XV.

Because of the long time duration needed to collect signals from the lead glass and execute the complicated logic associated with the high $p_\perp$ and mass triggers, we used two levels of triggers: fast triggers and slow triggers. Only in the presence of a fast trigger was information processed by the relatively slow logic to determine the presence of the slow triggers. Only in the presence of a slow trigger was data collected by the computer and written onto data tape. The slow trigger logic took 300 nanoseconds to process information. The fast trigger logic operated every rf bucket. The fast triggers were:

TU prescaled $(TU^P/_S)$
TD prescaled $(TD^P/_S)$
TU · TD (TUD)

The TU and TD prescale factors were typically 1024. This means only after 1024 TU signals did the TU prescaler unit produce one signal. Because the computer took ~800 μsec to process a trigger before it was ready for another, the number

of slow triggers per pulse had to be relatively small. Typically the slow triggers were:

$PTU \cdot TU^{P}/_{S}$
$PTD \cdot TD^{P}/_{S}$
$PTU \cdot PTD \cdot TUD \quad (\equiv PTUD)$
$MH \cdot \overline{M1} \cdot TUD \quad (\equiv MH\overline{M1})$
$MH^{P}/_{S} \cdot TUD \quad (\equiv MH^{P}/_{S})$
$MM^{P}/_{S} \cdot TUD \quad (\equiv MM^{P}/_{S})$
electron pair trigger

The first two of these were our single arm triggers. Our main pair triggers were PTUD and $MH\overline{M1}$. $\overline{M1}$, as mentioned in Section II. C, vetoed events with possibly more than one track per arm. Its effects will be discussed in the next section. The $MH^{P}/_{S}$ and $MM^{P}/_{S}$ triggers were used to study the action of the $MH\overline{M1}$ trigger. The electron pair trigger was used in the concurrent dielectron experiment. At times we included other slow triggers, often involving FU and FD which were produced when the signals from the calorimeters (E_{cal}) exceeded a preset threshold voltage. Numerous types of study runs involved various other fast and slow triggers. Typical fast and slow trigger rates are given in Table XV. Note that only ~70 events were recorded on tape every pulse.

IV. B. Track Quality Cuts

The events written on data tapes underwent a series of track quality cuts in our computer analysis program. The fates of typical sets of 1000 slow triggers are presented in Table XVI. The first requirement was the ability to somehow reconstruct the track of each particle (requiring only 2 wires out of 1Q, 1P, 1Y, 2 out of 3Q, 3P, 3Y and the correct elements of T0, V1, V2). The track was then required to have originated near the target and to have passed cleanly through the collimators, magnet and apparatus. (See Table III describing the fiducial volume.) Any event with more than one track per arm was discarded, since retaining it would only add confusion to particle identification and E_{cal}/p determination. This cut eliminated only a small percent of the real particles as seen in Table XVIII. Next the stringent reconstruction described in Section II. D was required. Finally the E_{cal}/p cut described in Section II. F was applied. This affected the slow triggered data very slightly because the high $p_\perp$ and mass triggers already required a large E_{cal} signal.

The use of the E_{cal} signal in the slow triggers greatly increased the fraction of events with reconstructable, fiducial tracks. [The fact that PT and MH required a proper V1, V2

combination also made a small (~25%) improvement in reconstructability.] This great improvement in the reconstructability of the data sample is evident in the comparison of Tables XVI and XVII. Table XVII was made using study runs in which only TU, TD and TUD were triggers. The enrichment of high quality tracks in the sample of events written on tape was one of the most important features of our high $p_\perp$ and mass triggers.

$\overline{M1}$ was used because it increased the fraction of reconstructable, fiducial pair events by a factor of ~1.7 when studying the 6-10 GeV mass spectra. (For the 4-6 GeV spectra, $\overline{M1}$ increased pair event reconstructability by ~1.1.) The reason for this is that unreconstructable events usually passed trigger requirements only because the proper counters were turned on by a spray of stray particles rather than one particle coming cleanly from the target. Since these particle sprays were more likely to turn on more than one V1 * V2 combination than legitimate particles, $\overline{M1}$ was effective in eliminating non-reconstructable events. The particle sprays were more frequent when the primary protons were delivered in uneven bunches (for example, in "super buckets"), so when the beam quality was bad, $\overline{M1}$ was an even greater boon to reconstructability. Originally we hoped $\overline{M1}$

would eliminate most of the Cerenkov accidental hits and stray hadrons which perhaps deposited their energy in the calorimeters along with the legitimate secondary, producing an artificially large E_{cal} signal. It was found, however, that $\overline{M1}$ reduced Cerenkov accidentals by only ~10% and made no difference to the width or mean value of the E_{cal}/p distribution. As one might expect, $\overline{M1}$ reduced the number of pair events thrown out by the single track per arm requirement by a factor of ~5. $\overline{M1}$ also eliminated good events, the percentage of which was monitored by PTUD triggers. The $\overline{M1}$ efficiencies for hadron pairs are presented in Table XIX. These efficiencies were found to be independent of the $p_\perp$ of each secondary.

IV. C. Amounts of Data Collected

For each mass range under study, we adjusted the incident beam intensity, analyzing magnet current, high $p_\perp$ and mass trigger threshold voltages and the Ne-N_2 mixture in Cerenkov 2. The running conditions are summarized in Table XX. Most of the time the polarities of the analyzing magnets were set as to accept opposite sign pairs. (Roughly equal times were spent with up^+dn^- and up^-dn^+.) Some time was spent looking at +/+ or -/- pairs, although this was not popular with members of our group interested in searching for resonances in the dihadron or dielectron mass spectra. Normally we used 400 GeV protons on a beryllium target. We occasionally used a tungsten target to study A (nucleon number) dependence of hadron pair production and for a while used 200 and 300 GeV protons to study s dependence. The amounts of data corresponding to each running condition are given in Table XXI. The total luminosities can be converted to incoming protons by multiplying N by $\sim 2 \times 10^6$. A running day as defined in Table XXI corresponds to a reasonably full day of data taking with steady, high quality beam. Because of study runs, equipment problems and accelerator shutdowns, the data summarized in Table XXI was actually taken over an ~5 month period.

V. BACKGROUNDS

The first type of background I shall be discussing is single arm background. These background events passed all track quality cuts but still were not caused by real particles at the observed momenta. As discussed in previous sections, most of these events were caused by one of two phenomena: (1) sprays of stray particles turning on enough counters to pass all trigger requirements or (2) single particles not coming directly from the target, but scattering off objects such as magnet pole faces. Although the first type made up the bulk of undesirable events written on tape, almost all were eliminated by the stringent reconstruction requirements described in Section IV. D. Most of the illegitimate events of the second type (and the survivors of the first type) were eliminated by cuts on two independent quantities: the x position of the track at the target (see Table III) and E_{cal}/p. Even though the number of illegitimate events surviving these cuts was small, as the number of legitimate events decreased with increasing $p_\perp$, this background became more and more significant.

For two bins in $p_\perp$ (3-4 and 4-5 GeV/c) we attempted to directly measure this background. Figure 27 (using PTU

triggers from the 6-10 GeV running conditions) shows the distribution of events on an x_{target} vs. E_{cal}/p scatter plot. The legitimate events are distributed in a narrow Gaussian distribution about $x_{target} = 0$. All events have a somewhat high E_{cal}/p because the E_{cal} signal was used in the high $p_\perp$ trigger. One would expect the background events to be uniformly distributed in x_{target} and tend to have low values of E_{cal}/p. The events distributed about $x_{target} = 5$ cm should be ignored because they are the results of interactions in the thin, titanium window of the target box, ~70 cm upstream of the target, and are eliminated by the x_{target} cuts (shown as dashed lines in Fig. 27). Assuming the events in the left third of each plot are background events, and just as many of these background events populate the central third (the region within the x_{target} cuts), we estimated the background to real ratio to be on the order of 0.4% for $p_\perp$ = 3 to 4 GeV/c and 3% for $p_\perp$ = 4 to 5 GeV/c. A sneak preview of the high $p_\perp$ region of our single arm invariant cross section (which will be discussed in detail in the next section) confirms these order of magnitude background estimates. Assuming the background events were uniformly distributed across the aperture, we adjusted the level of our background to the highest value

consistent with the cross section measurement of Fig. 28. We see that although the background to real ratio is less than ~15% at $p_\perp$ = 5 GeV/c, it falls rapidly to ~1% at 4 GeV/c and is negligible below that. Because the background is small over the ranges in $p_\perp$ under study and is difficult to accurately determine, no attempt was made to subtract it from our measurements.

Background events of the second type to which our experiment was sensitive are accidental pairs. These are pairs of particles created during the same rf bucket but not by the same interaction. Hence any sample of pair events, nUD, is made up of real and accidental pairs, nUD_{real} and nUD_{acc}. We can calculate nUD_{acc} if we know the corresponding single arm quantities, nU and nD. In terms of probabilities per rf bucket, P_b,

$$P_b(nUD_{acc}) = P_b(nU)\ P_b(nD)$$

Of course summing over all buckets, $\Sigma P_b(nU) = nU$ and $\Sigma P_b(nUD_{acc}) = nUD_{acc}$. Using the proportionality of $P_b(nU)$ and $P_b(nD)$ to the intensity of the rf bucket, i_b,

$$P_b(nU) = i_b \frac{nU}{\Sigma i_b}$$

we can write

$$P_b(nUD_{acc}) = nU\ nD\ \frac{i_b^2}{(\Sigma i_b)^2}$$

Summing over all buckets

$$nUD_{acc} = nU\ nD\ \frac{\Sigma i_b^2}{(\Sigma i_b)^2}$$

$(\Sigma i_b)^2 / \Sigma i_b^2$ we call the effective number of rf buckets. (If i_b were constant, this would be equal to the actual number of rf buckets.) It is very useful to define a quantity, B_{int}, as the number of interacting protons per effective rf bucket. Hence

$$nUD_{acc} = nU\ nD\ \frac{B_{int}}{\#\ \text{int. protons}}$$

(Recall from Section II. A, the number of interacting protons is equal to $C_R N$.)

B_{int} was measured with T triggers, since it was found that $TUD_{acc} >> TUD_{real}$ (more on this later). Specifically

$$B_{int} = C_R N\ \frac{TUD}{TU\ TD}$$

where N, TUD, TU and TD were all measured with scalers.

B_{int} depended only on the intensity and quality of the incident beam. In order to keep B_{int} and hence the number of accidental pairs as low as possible, pulses with B_{int} much

higher than the average were removed from the data sample. Table XXII lists the B_{int} cuts and averages for the different running conditions. As previously mentioned, we used our bucket intensity monitor (SB) to eliminate individual rf buckets with very large intensities. Figure 29 shows a typical B_{int} distribution with and without the employment of SB.

The pair quantity used in the measurement of B_{int} really should have been TUD_{acc}. Hence B_{int} was multiplied by the correction factor $\frac{TUD_{acc}}{TUD}$ $(= 1 - \frac{TUD_{real}}{TUD})$. We obtained a lower limit of TUD_{real}/TUD by knowing how many TUD triggers passed all reconstruction and track quality requirements (see Table XVII) and then knowing what percentage of these pairs came from the same interaction. The latter piece of information required the measurement which will be discussed in Section VII. A. on the correlation function R. We will see that the ratio of real to total hadron pairs is $R/(R + B_{int})$, where to first order R is a function only of m', the sum of both hadrons' $p_\perp$. From the distribution in m' of the TUD triggered events, we found the ratios of real to total reconstructed, high quality TUD pairs to be 0.20, 0.20 and 0.15 for running conditions corresponding to the mass ranges 4-5, 5-6 and 6-10 GeV respectively. From this

and Table XVII we calculated the lower limits of TUD_{real}/TUD listed in Table XXII. To the extent the TUD triggers which failed the track quality or reconstruction requirements were uncorrelated (which is probably close to the truth since these pairs were of low m' and, as we shall see in Section VII. A, were therefore rarely correlated), the actual values of TUD_{real}/TUD are close to these lower limits.

We verified that the percentage of TUD_{real} in TUD was indeed very small through the dependence of TUD on intensity. The real component of TUD was proportional to the number of interactions, so it was proportional to N. TUD_{acc} per pulse, on the other hand, was proportional to the product of TU and TD [assuming $\Sigma i_b^2 / (\Sigma i_b)^2$ was constant pulse to pulse] and was therefore proportional to N^2. Writing

$$\frac{TUD}{N} = \left(\frac{TUD_{real}}{N}\right) + \left(\frac{TUD_{acc}}{N^2}\right) N$$

tells us a pulse by pulse scatter plot of TUD/N vs. N should produce a straight line with a y intercept of TUD_{real}/N. The assumption $\Sigma i_b^2 / (\Sigma i_b)^2$ was constant pulse by pulse is a bad one, however. Actually, $\Sigma i_b^2 / (\Sigma i_b)^2$ varied pulse to pulse and run to run, because it depended on how constant the intensity was

during each spill. Also, there was occasionally a correlation between spill uniformity and beam intensity. We made use, then, of a quantity called TUD4: the coincidence of a TU trigger with a TD trigger delayed by 4 rf buckets. Obviously there was no real component of TUD4. TUD4 can be expressed as

$$\text{TUD4} = \text{TU TD} \frac{\Sigma i_b i_{b+4}}{(\Sigma i_b)^2}$$

Hence

$$\frac{\text{TUD4}}{\text{TUD}_{acc}} = \frac{\Sigma i_b i_{b+4}}{\Sigma i_b^2}$$

This ratio, called sb (for super bucket ratio: the larger the bucket to bucket intensity variations, the smaller this quantity was) was found to be somewhat more stable than $\Sigma i_b^2 / (\Sigma i_b)^2$. It was typically 0.65 to 0.90. Hence we write

$$\frac{\text{TUD}}{N} = \left(\frac{\text{TUD}_{real}}{N}\right) + \frac{1}{sb}\left(\frac{\text{TUD4}}{N}\right)$$

so scatter plotting TUD/N vs. TUD4/N should produce a straight line with slope $\frac{1}{sb}$ and y intercept TUD_{real}/N. Figure 30 shows such a plot using the 4-5 GeV running conditions. (The x and y axes have been interchanged to improve accuracy.) Lines have been drawn through an intercept corresponding to

$$\left(\frac{TUD_{real}}{N}\right)_{min} = \left(\frac{TUD_{real}}{TUD}\right)_{min} < \frac{TUD}{N} >$$

$$\simeq 0.01 .$$

The distribution of events is consistent with TUD_{real}/TUD being anywhere between zero and ten times our lower limit. Hence we corrected B_{int} by $1 - (\frac{TUD_{real}}{TUD})_{min}$, realizing there is an uncertainty in B_{int} of a few times this correction. All together we estimated the systematic error associated with B_{int} to be +5%, -10%.

The first type of background I discussed, single arm background, also contaminated the sample of pair events. These background events, however, were mostly uncorrelated so were removed from the pairs by the accidental subtraction we made through the use of B_{int}.

VI. SINGLE HADRON CROSS SECTIONS AND PARTICLE RATIOS

The measurements of single hadron cross sections and particle ratios from $p_\perp$ = 1 to 7 GeV/c were carefully made several years before our experiment by the Chicago-Princeton collaboration.[13] We collected single arm data along with pairs in order to (1) subtract accidental pairs, (2) measure correlations, (3) check systematic errors by comparing results from the up and down arms and different running conditions and (4) present evidence to support or contradict the Chicago-Princeton measurements.

We will present the invariant cross section, $E\frac{d^3\sigma}{dp^3} = \frac{1}{2\pi}\frac{1}{p_\perp}\frac{d^2\sigma}{dy\,dp_\perp}$, which we measure at $y \cong 0$. In terms of measurable quantities,

$$E\frac{d^3\sigma}{dp^3} = \frac{C_{XS}}{N} \cdot \frac{(\text{events within } p_\perp \text{ and } p_\perp + \Delta p_\perp)}{p_\perp\,\Delta p_\perp \text{ acceptance } \epsilon_{PT}} \cdot \frac{(\text{single arm pre-scale factor})}{(1 - \text{decay probability})\text{ overall efficiency}}$$

where C_{XS} is the constant defined in Section II. A, N is the flux measured by our neutrals counter, the acceptance is that of Fig. 9 or Fig. 17, and ϵ_{PT} is the high $p_\perp$ trigger efficiency. The overall efficiency is the product of the efficiencies due to the

scintillation counters, wire chambers, E_{cal}/p cut, single track requirement and data compression programs. The decay probability for pions or kaons is calculated from

$$\text{decay probability} = 1 - e^{\frac{-L}{\beta\gamma c\tau}}$$

where L is the distance from the target to calorimeters, c is the speed of light, βc is the particle's velocity, $\gamma = (1 - \beta^2)^{-\frac{1}{2}}$ and τ is the mean lifetime of pions or kaons. The decay probabilities are in the range 10 to 17% for kaons and 1 to 3% for pions.

Our single particle cross sections (per Be nucleus) for hadrons (using no particle identification) are compared to Chicago-Princeton's in Fig. 31. The invariant cross sections have been multiplied by $p_\perp^8$ in order to make a detailed comparison possible. Our data points show both statistical errors (indicated by the horizontal caps) and combined statistical and estimated systematic errors (indicated by the full length of the vertical lines). They do not show an additional ±7% normalization error associated with C_{XS}. Our cross sections show remarkably good agreement with those of Chicago-Princeton. The data for Fig. 31 (and Fig. 32) were taken with various running conditions according to:

$p_\perp$ (GeV/c)	Running Conditions for Mass Range (GeV)
1.15 to 2.55	4-5
2.55 to 2.95	5-6
2.95 to 6.55	6-10

The consistency of our measurements using different running conditions appears to be within our estimated systematic errors. Data from the up and down arms have been combined. Cross sections from each arm alone show the same degree of agreement with Chicago-Princeton and with each other as the data of Fig. 31.

Our particle ratios, namely $K^{\pm}/\pi^{\pm}$ and $P^{\pm}/\pi^{\pm}$ as functions of $p_\perp$, were unfortunately not measured as directly as one might like. For example,

$$\frac{K^+}{\pi^+} = \frac{(K^+ \text{ within } p_\perp \text{ and } p_\perp + \Delta p_\perp)}{(\pi^+ \text{ within } p_\perp \text{ and } p_\perp + \Delta p_\perp)} \cdot \frac{\epsilon_{PT}(\pi^+)}{\epsilon_{PT}(K^+)}$$

$$\cdot \frac{(1 - \text{decay of } \pi^+)}{(1 - \text{decay of } K^+)} \cdot \text{misidentification corrections}$$

Recall the high $p_\perp$ trigger efficiency depended quite strongly on particle type (see Fig. 26). Misidentification corrections are given in Table XI. The combined corrections to the raw particle ratios were typically factors of 1.3 for $K^{\pm}/\pi^{\pm}$, 1.5 for

P^+/π^+ and 1.2 for $\overline{P}/\pi^-$. The pions, kaons and protons were restricted to the full identification region so that no acceptance corrections were needed. Our ratios and Chicago-Princeton's are shown in Fig. 32. Our K/π ratios are in fairly good agreement and our P/π ratios roughly agree with those of Chicago-Princeton. The P^+/π^+ and $\overline{P}/\pi^-$ ratios from the 5-6 GeV data sample ($p_\perp = 2.75$) seem high relative to Chicago-Princeton's as well as the two points at the highest $p_\perp$. At first it seems our excess of protons at high $p_\perp$ could be due to single arm background, but even if all background events failed to fire the Cerenkov counters (and hence were identified as protons), at a $p_\perp$ of 4 GeV/c less than 25% of our $\overline{P}$ sample and 5% of our P^+ sample would be background. It should be pointed out that we did not choose our running conditions for the best measurements of particle ratios. If, instead of running at high intensities and pre-scaling the single arm triggers by a factor of 1000, we had run at low intensities without pre-scaling the single arm triggers, then both our Cerenkov accidentals and single arm backgrounds would have been negligible.

VII. HADRON PAIR PHYSICS

VII. A. The Correlation Function R

The correlation function R is a convenient form in which to present our data because we can measure R directly and with few sources of systematic error. R by definition is

$$R = \frac{E_1 E_2 \frac{d^6\sigma}{dp_1^3 dp_2^3} \Big/ \sigma_{inel}}{E_1 \frac{d^3\sigma}{dp_1^3} \Big/ \sigma_{inel} \quad E_2 \frac{d^3\sigma}{dp_2^3} \Big/ \sigma_{inel}}$$

where our cross sections are evaluated at $y_1 = y_2 = 0$ and where our pair cross section is evaluated at $\phi_2 - \phi_1 = 180^o$. In words, R is the ratio of the probability of observing a hadron at $p_{\perp 1}$ and another hadron on the opposite side of the interaction at $p_{\perp 2}$ to the probability if the two hadrons were uncorrelated. In terms of measurable quantities,

$$R = C_R N \frac{n_{real}(p_{\perp 1}, p_{\perp 2})}{n(p_{\perp 1})\, n(p_{\perp 2})}$$

where C_R is defined in Section II. A, N is the flux measured by our neutrals monitor ($C_R N$, then, is the total number of interacting protons) and $n_{real}(p_{\perp 1}, p_{\perp 2})$ is the number of real

hadron pairs per $(GeV/c)^2$ at $p_{\perp 1}$ and $p_{\perp 2}$. $n(p_{\perp 1})$ is the number of hadrons per GeV/c at $p_{\perp 1}$ when looking at one side of the interaction only. Note that no acceptances or efficiencies (unless MH triggers were used) were needed to calculate R, because the pair acceptances and efficiencies are the products of the single arm acceptances and efficiencies. So that no high $p_{\perp}$ trigger efficiencies entered our equation for R, we always used PTUD triggers.

The number of pairs coming from different interactions $[n_{acc}(p_{\perp 1}, p_{\perp 2})]$ had to be subtracted from the observed $n(p_{\perp 1}, p_{\perp 2})$. Recall from Section V,

$$n_{acc}(p_{\perp 1}, p_{\perp 2}) = \frac{B_{int}}{C_R N} n(p_{\perp 1}) n(p_{\perp 2})$$

where B_{int} is the number of interacting protons per effective rf bucket. In terms of observed pairs, therefore,

$$R = C_R N \frac{n(p_{\perp 1}, p_{\perp 2})}{n(p_{\perp 1}) n(p_{\perp 2})} - B_{int}$$

Hence the removal of accidentals from R involved only the subtraction of a constant. A useful corollary of this is that the ratio of accidental to real pair events can be simply expressed as B_{int}/R.

The only sources of systematic error came from the measurement of B_{int} (σ_R = +10%, -5% of B_{int}) and from single arm accidentals, which affected R through the single particle cross sections in its denominator. Since our R measurements involved hadrons of $p_\perp \tilde{<} 5$ GeV/c, this background was small. (See Section V.) The systematic error associated with C_R (±11%) affected only the overall normalization of R and was therefore not included in our figures.

Looking at our measured values of R on a $p_{\perp 1}$, $p_{\perp 2}$ grid, one notices R is a strong function of $m' \equiv p_{\perp 1} + p_{\perp 2}$ but a weak function of $P_\perp' \equiv p_{\perp 1} - p_{\perp 2}$. This is illustrated in Figs. 33, 34 and Table XXIII. All 400 GeV beryllium +/- data were used, with a lower limit in m' chosen for each running condition (m' > 3.9, 4.9 or 5.9 GeV/c for the 4-5, 5-6 or 6-10 GeV mass range) to limit the percentage of accidental pairs. It should be noted that our R measurements from different running conditions (and hence different B_{int}'s) agreed, substantiating our procedure of subtracting accidentals. The flatness in R as a function of $P_\perp'$ allowed us to improve statistical accuracy for Fig. 33 by averaging our R values within $-1.1 < P_\perp' < 1.1$ GeV/c. Each curve of Fig. 34 was the average of several curves of constant

m' after each of these curves was raised or lowered by a constant factor so that their values near $P_\perp' = 0$ were the same. This was necessary to assure that the shape of each curve of Fig. 34 was not due to a varying mean m'.

Our correlation results are difficult to interpret in this form. The flatness of our $R(P_\perp')$ curves shows that the two hadrons by themselves do not display strict transverse momentum conservation. The tremendous increase in R with m' ($R \propto e^{1.50\, m'}$ near $m' = 7$ GeV/c) will be understood when we discuss x_e scaling.

VII. B. The A Dependence of Hadron Pairs

The nucleon number (A) dependence of single hadron production at large $p_\perp$ was carefully measured by the Chicago-Princeton collaboration several years ago.[14] They found single hadron cross sections to vary as A^α, where α as a function of $p_\perp$ is as shown in Fig. 35 . To get a feeling for the meaning of α, let us consider several simple models of proton-nucleus interactions and their predicted values of α. For an "opaque" model of the nucleus, where incident protons would most likely interact soon after contact with its surface, cross sections would vary as $A^{2/3}$. If, however, an incident proton was equally likely to interact with a nucleon at any point within the nucleus, a cross section would be proportional to the number of nucleons, so α would be one. The observation by Chicago-Princeton that α is greater than one implies the nucleus must act collectively in producing single hadrons. Possible explanations of this collective behavior include multiple scattering,[15] the collective motion of nucleons or partons,[16] and the alteration by the nucleus of the gluon field between scattered quarks.

Our measurement of α is based on the equation

$$\left(\frac{A_W}{A_{Be}}\right)^{\alpha} = \frac{(C_{XS} \cdot \text{events/N})_W}{(C_{XS} \cdot \text{events/N})_{Be}}$$

The values for A and for the ratio of the cross section constants can be found in Tables I and II. Our measured α values for single hadrons are presented in Fig. 35. To study the A dependence of pair cross sections we assumed pair production also varies as A^{α}. Of course using only two target materials, the power law dependence for pairs could not be checked. Instead of looking at the pair α on a $p_{\perp 1}$, $p_{\perp 2}$ grid, we once again rotate axes and look at α as a function of $m'(= p_{\perp 1} + p_{\perp 2})$ and $P_{\perp}'$ $(= p_{\perp 1} - p_{\perp 2})$. Our results are presented in Fig. 36. First we see, after integrating over all $P_{\perp}'$, $\alpha(m')$ is consistent with 1. Next we see, especially for large values of m' (where large values of $P_{\perp}'$ are accessible), $\alpha(P_{\perp}')$ increases with $\left|P_{\perp}'\right|$ to values significantly greater than 1.

Why the production of single hadrons at high $p_{\perp}$ should be enhanced by a large nucleus but not the production of pairs, unless $\left|p_{\perp 1} - p_{\perp 2}\right| \tilde{>} 2$ GeV/c, is very mysterious. Our observations are perhaps consistent with collective motion

models, where a kick is given to the $p_\perp$ of one hadron at the expense of the $p_\perp$ of the away side hadron. On the other hand, the larger nuclear enhancement of asymmetric hadron pairs compared to symmetric pairs may be because the low $p_\perp$ hadron of an asymmetric pair has a low fraction (z) of the scattered quark $p_\perp$ and, for some reason, the production of such hadrons is more sensitive to large nucleii.

For single hadrons, α ($p_\perp$) was observed by Chicago-Princeton to be species dependent. For pairs we observed α was also species dependent. α, for all m' and $|P_\perp'| < 2.1$ GeV/c, is given as a function of particle combination in Table XIV. The possible significance of these results will be discussed in Section VII. D.

Further details of our A dependence measurements can be found in Reference 17.

VII. C. x_e Scaling

The quark-quark scattering picture makes definite predictions for hadron-hadron correlations. In a simple-minded way, let us see how these predictions come about.[18] First let us ignore transverse motion of the quarks within the beam proton or target nucleon. Let us say the scattered quarks are produced with equal and opposite transverse momentum $P_\perp$ and with cross section $\frac{d\sigma}{dP_\perp} = \phi(P_\perp, \sqrt{s})$. Jet experiments tell us $\phi(P_\perp)$ can be approximated by $AP_\perp^{-n}$, where for our beam energies $n \sim 12$.[19] In the quark-quark scattering picture, the mesons or baryons we detect are made up of the scattered quarks and/or quarks pulled out of the vacuum by the gluon field between the scattered quarks. If the probability of producing such a hadron with transverse momentum between $p_\perp$ and $p_\perp + dp_\perp$ from a scattered quark of transverse momentum $P_\perp$ is $D(z)\,d(z)$, where $z = \frac{p_\perp}{P_\perp}$, then the cross section of the hadron is given by

$$\frac{d\sigma}{dp_\perp} = \int_{p_\perp}^{\infty} \phi(P_\perp)\ D(z)\ \frac{dP_\perp}{P_\perp}$$

$$= \int_0^1 \phi\left(\frac{p_\perp}{z}\right)\ D(z)\ \frac{dz}{z}$$

$$\cong A\, p_\perp^{-n} \int_0^1 D(z)\ z^{n-1}\, dz$$

At this point two interesting features of single hadron production in the quark-quark picture are evident. First, the $p_\perp$ dependence of the cross section of the detected hadron is the same as that of the scattered quark. The comparison of jet cross sections to single hadron cross sections substantiates this prediction.[19] Second, the z^{n-1} inside the integral over z means only the values of D at z near 1 are important. For the same reason, the average z should be near 1. Using results from jet experiments, the detected hadron carries on the average ~85% of the transverse momentum of the scattered quark. (We must not be misled. Given a hadron was <u>detected</u>, it carries ~85% of the quark $P_\perp$. Given a quark was scattered, however, the average $p_\perp$ of the leading hadron is a much smaller percentage of the quark $P_\perp$. This is known as trigger bias.) Next we write the cross section for back to back hadron pairs.

$$\frac{d^2\sigma}{dp_{\perp 1}\, dp_{\perp 2}} = \int_{p_{\perp 1}}^{\infty} \phi(P_\perp)\, D_1(z_1)\, D_2(z_2)\, \frac{dP_\perp}{P_\perp^2} \quad \text{where } p_{\perp 2} \leq p_{\perp 1}$$

$$= \int_0^1 \phi\left(\frac{p_{\perp 1}}{z_1}\right) D_1(z_1)\, D_2\left(\frac{p_{\perp 2}}{p_{\perp 1}}\, z_1\right) \frac{dz_1}{p_{\perp 1}}$$

$$\cong A\, p_{\perp 1}^{-n-1} \int_0^1 D_1(z_1)\, D_2\left(\frac{p_{\perp 2}}{p_{\perp 1}}\, z_1\right) z_1^n\, dz_1$$

We define $x_e \equiv \frac{p_{\perp 2}}{p_{\perp 1}}$ and use the conditional probability function $\frac{dN}{dx_e}$ defined as

$$\frac{dN}{dx_e} \equiv \frac{\frac{d^2\sigma}{dp_{\perp 1}\, dx_e}}{\frac{d\sigma}{dp_{\perp 1}}}$$

In words, $\frac{dN}{dx_e}\,\Delta x_e$ is the probability that given a hadron with $p_\perp = p_{\perp 1}$ is observed, a hadron on the opposite side of the interaction with $p_\perp$ between $x_e p_{\perp 1}$ and $(x_e + \Delta x_e)\, p_{\perp 1}$ is also observed. Substituting our expressions for the single and pair hadron cross sections,

$$\frac{dN}{dx_e} = \frac{\int_o^1 D_1(z_1)\, D_2(x_e z_1)\, z_1^n\, dz_1}{\int_o^1 D_1(z_1)\, z_1^{n-1}\, dz_1}$$

The fact that this $\frac{dN}{dx_e}$ is independent of $p_{\perp 1}$ is called x_e scaling. Feynman, Field and Fox, taking into account effects like the transverse momentum of quarks within the beam and target, and taking into account our experimental aperture, also predict approximate x_e scaling (for regions in $p_\perp$ much larger than the mean $p_\perp$ of the beam and target quarks). Reference 20 shows the predictions of Feynman-Field-Fox made for us just before the analysis of our data. Next we shall put our correlation data in the form of $\frac{dN}{dx_e}$ and test for x_e scaling.

The correlation function R is related to $\frac{dN}{dx_e}$ in a very simple way. From the definition of $\frac{dN}{dx_e}$ we find

$$\frac{dN}{dx_e} = \frac{0.065}{\sigma_{inel}} R E_2 \frac{d^3\sigma}{dp_2^3} p_{\perp 1} p_{\perp 2}$$

0.065 comes from the way we chose to express $\frac{dN}{dx_e}$. We wanted to emphasize that, given a trigger hadron, our acceptance on the opposite side of the interaction was small. Hence we quote $\frac{dN}{dx_e}$ as the probability of the away arm hadron falling into a constant acceptance (close to our maximum acceptance) of 0.065, with ranges in y and ϕ close to those of our actual aperture. (See Section II. B.) Hence we can quickly obtain a $\frac{dN}{dx_e}$ curve through the multiplication of our R(m') with our single hadron cross section. Since our R(m') is approximately R at $P_\perp' = 0$, this $\frac{dN}{dx_e}$ is at $x_e = 1$ and is a function of $p_{\perp trig} = p_{\perp away} = m'/2$. The result is shown in Fig. 37. Roughly, we do see x_e scaling, which is quite striking compared to the enormous rise and fall of R and the away arm cross section with $p_\perp$.

In terms of directly measurable quantities,

$$\frac{dN}{dx_e} = \frac{\text{real pair events within } x_e \text{ and } x_e + \Delta x_e}{(\text{trigger arm events})\,(\text{trigger arm pre-scale factor})\,\Delta x_e}$$

$$\cdot \frac{1}{\left[\frac{\text{acceptance}}{0.065}\,\epsilon_{PT}\,(1 - \text{decay prob})\,\text{overall eff}\right]_{\text{away arm}}}$$

where the quantities used in this equation are those defined in Section VI. In order to explore $\frac{dN}{dx_e}$ where the efficiency of the PT trigger was low, however, we found that measuring R and $E_2 \frac{d^3\sigma}{dp_2^3}$ independently (i.e. perhaps using different running conditions) and then calculating $\frac{dN}{dx_e}$ reduced possible systematic errors. Our results are presented in Figs. 38 and 39. These figures are based upon R values using PTUD triggers and using the observation that $R_{h^+h^-}$ is symmetric about $P_\perp' = 0$ (see Fig. 34) to combine data accordingly. To improve statistical precision we plotted $\int \frac{dN}{dx_e}\,dx_e$ in Fig. 38, which should also be independent of $p_{\perp trig}$ if x_e scaling is obeyed. Indeed, we observe x_e scaling near and above $p_{\perp trig} = 2.7$ GeV/c. This observed independence of $\frac{dN}{dx_e}$ with $p_{\perp trig}$ motivated us to combine data within $3 < p_{\perp trig} < 4$ GeV/c to better show the x_e dependence of $\frac{dN}{dx_e}$ in Fig. 39. From our final equation for $\frac{dN}{dx_e}$ from our simple-minded quark-quark scattering picture, the z_1^n inside the integrals over z_1 means only the integrands

near $z_1 = 1$ are important, so that the x_e dependence of $\frac{dN}{dx_e}$ should be roughly that of $D_2(x_e)$. The data presented in Fig. 39 fit very well to a line proportional to $e^{-5.7 x_e}$.

We must remember the data we are using were taken using a beryllium target. Let us estimate the effect of A dependence on our x_e scaling results. From the definition of $\frac{dN}{dx_e}$ we find we must correct the pair cross section in the numerator and trigger arm cross section in the denominator for A dependence. Looking only at $\frac{dN}{dx_e}$ at $x_e = 1$, we can assume the pair cross section is proportional to $A^{1.0 \pm 0.05}$ (see Fig. 36). Hence we multiply our $\frac{dN}{dx_e}$ values by $A^{\alpha - 1}$, where α is for single hadrons (as measured by Chicago-Princeton). (See Fig. 35.) The results are given in Fig. 40. x_e scaling is still very evident.

Let us gain a feeling for the effect of the transverse motion of the beam and target quarks on our simple-minded prediction of exact x_e scaling. Mainly because of this transverse motion, the distribution of the net $P_\perp$ of the two scattered quarks is smeared around $P_{\perp net} = 0$. This does not significantly affect the shape of the pair cross section as a function of m', but does affect the single hadron cross section, because a

number of hadrons are boosted to a higher $p_\perp$ (typically ~ 1 GeV/c higher[21]) where the population before their arrival was relatively sparse. The steeper the exponential slope of the single hadron cross section ($\frac{d\sigma}{dp_\perp}$), the larger this effect is. From $p_\perp$ = 2 to 5 GeV/c, this slope decreases very gently. $\frac{dN}{dx_e}$ ($x_e \cong 1$, $p_{\perp trig}$) is affected only through the trigger arm cross section in its denominator. This net $P_\perp$ smearing, therefore, changes our exact x_e scaling prediction into a $\frac{dN}{dx_e}$ ($x_e \cong 1$, $p_{\perp trig}$) with a gentle rise on the order of that observed when $p_{\perp trig} > 2.7$ GeV/c in Fig. 40.

The agreement between our data and predicted x_e scaling shows consistency if not proof that constituent scattering is the dominant mechanism for the production of hadrons with $p_\perp \gtrsim 2.7$ GeV/c. The observed fall of $\frac{dN}{dx_e}$ in Fig. 40 when $p_{\perp trig} < 2.5$ GeV/c is a deviation from x_e scaling, perhaps indicating the dominance of another mechanism producing hadrons at these $p_\perp$. This non-x_e scaling at low $p_\perp$ is consistent with previous dihadron measurements.[8]

VII. D. The Species Dependence of R

If quark-quark scattering were the only process by which hadrons are produced at large $p_\perp$, one would expect no correlation between the type of hadron produced on one side of the interaction and the type produced on the opposite side. This is because any quark from the beam proton can collide with any quark from the target nucleon after which the two quarks dress themselves with other quarks independently to form the observed hadrons. [We are neglecting the small effect due to the requirement that whenever the two hadrons contain valence quarks of the original scatterers, one must have come from a beam proton and the other from a target proton or neutron. For example, if the two hadrons always were to contain valence quarks of the scatterers, this effect would lead to a ratio of π^+ (away arm) yield given a π^- trigger to that given a π^+ trigger of about 1.05.]

If species correlations are indeed absent, then $\frac{dN}{dx_e}$ should be independent of the species of the trigger hadron. From the relationship between R and $\frac{dN}{dx_e}$, we see R should be independent of the species of either hadron. Therefore we will compare R for all species combinations and look for their equality. The lack of statistical precision prevented a straightforward

comparison of R(m') between all combinations of species. Therefore we divided R for each species by R for h^+h^- at each m' (in order to divide out the common exponential dependence of R) and then averaged over m'. Note that $R/R_{h^+h^-}$ can be thought of as a pair particle ratio divided by the product of single particle ratios. No attempt was made to correct for particle misidentification. The loss of particles from a π, K or P sample is an inefficiency which, as we recall, does not affect R. Contamination of different particle types into the species sample under consideration moves the measured R in the direction of the R of the contaminants in an amount proportional to the degree of contamination. (See Table XI.) Hence the only effect of particle misidentification is to bring the R ratios slightly closer to one another.

Our $R/R_{h^+h^-}$ are presented in Fig. 41 (and Table XXV). We used PTUD triggers and restricted all momenta to the triple identification region. The ranges in m' were chosen to correspond to the x_e scaling region (m' = 5.9 to 7.9 GeV/c) and the region where a process other than constituent scattering may be present (m' = 3.9 to 5.9 GeV/c). As one can see, our R ratios are not all the same.

The phenomenon mentioned in the last section, net $P_\perp$ smearing, is responsible for surprisingly large deviations in $R/R_{h^+h^-}$ from unity. Since the exponential slopes of the single hadron cross sections differ between particle types, the effects of net $P_\perp$ smearing on R, which contains two single arm cross sections in its denominator, are species dependent. We can look at this in a more simple-minded way. Single hadrons observed at a certain $p_\perp$ are most likely low $p_\perp$ hadrons in the quark-quark center of mass frame (where $P_{\perp net} = 0$) which have been given a boost of 1 GeV/c or so by the net $P_\perp$ smearing.[21] The single hadron particle ratios at $p_\perp = 4$ GeV/c, therefore, actually may correspond to a $p_\perp$ of 3 GeV/c in the quark-quark center of mass frame. It is the quark-quark center of mass $p_\perp$ which is the variable of interest in studying the basic constituent interaction. Therefore, if each hadron of a <u>pair</u> were to have a $p_\perp$ of 3 GeV/c, which, on the average, should also be the $p_\perp$ in the quark-quark center of mass frame (because of symmetry), the probability of each being a π, K or P should depend on the <u>single</u> hadron particle ratios measured at a single arm $p_\perp$ of about <u>4</u> GeV/c. Hence our naive expectations of $R/R_{h^+h^-}$ being 1 should, in the quark-quark scattering model, be corrected by

the ratios of particle ratios at $p_\perp$ + 1 GeV/c to those evaluated at $p_\perp$. Our new predictions are presented in Fig. 41. The data indeed follow the trend of our crude predictions. More accurate predictions require an estimate of the actual distribution in net $P_\perp$ which produces the effect we have been discussing.

Two species combinations of interest are K^-K^+ and $\overline{P}P$ because, if quantum number exchanging processes are at work, the $R/R_{h^+h^-}$ for these two combinations should be higher than the rest. In the low m' plot of Fig. 41 we do indeed see such an effect, which is diminished in the high m' plot as it should be if quark-quark scattering is the dominant process at large m'. Before we jump to conclusions, however, we must remember our R ratios were measured using beryllium, and A dependence corrections are quite species dependent. To correct for A dependence we multiply our measured R's by $A^{\alpha_1+\alpha_2-\alpha_{pair}}$, where α_1 and α_2 are single particle α's (see Ref. 14) and α_{pair} is listed in Table XXIV. Our A-dependence corrected R ratios are presented in Fig. 41. We see the R ratios for K^-K^+ and $\overline{P}P$ are no longer larger than the rest. This still may be an interesting observation, however, perhaps indicating the enhancement of a low $p_\perp$ quantum number exchanging process by large nuclei.

VII. E. $E_1 E_2 \, d^6\sigma / dp_1^3 \, dp_2^3$

Perhaps the most direct way to present our hadron pair data is the invariant six-fold differential cross section, $E_1 E_2 \frac{d^6\sigma}{dp_1^3 \, dp_2^3}$. We quote this cross section per beryllium nucleus and evaluated at $y_1 = y_2 = 0$ and $\phi_1 - \phi_2 = 180^o$. In terms of directly measurable quantities,

$$E_1 E_2 \frac{d^6\sigma}{dp_1^3 dp_2^3} = \frac{C_{XS}}{N} \cdot \frac{\text{real pair events within} \begin{Bmatrix} p_{\perp 1} \text{ and } p_{\perp 1} + \Delta p_{\perp 1} \\ p_{\perp 2} \text{ and } p_{\perp 2} + \Delta p_{\perp 2} \end{Bmatrix}}{p_{\perp 1} \, p_{\perp 2} \, \Delta p_{\perp 1} \, \Delta p_{\perp 2} \, \text{acceptance}_1 \, \text{acceptance}_2}$$

$$\cdot \frac{1}{\epsilon_{MH} \, \epsilon_{\overline{M1}} (1 - \text{decay prob})_1 \, (1 - \text{decay prob})_2}$$

$$\cdot \frac{1}{\text{overall efficiency}_1 \, \text{overall efficiency}_2}$$

Basically the acceptances and efficiencies used here are the products of those used for our single hadron cross sections. Because statistical and systematic accuracy was improved through the use of $MH\overline{M1}$ triggers rather than PTUD, we needed ϵ_{MH}, the high mass trigger efficiency, and $\epsilon_{\overline{M1}}$, the efficiency of $\overline{M1}$ (see Table XIX). In order to determine if $\overline{M1}$ altered the ratio of real to accidental pairs, we measured R with PTUD

triggers both with and without the employment of $\overline{M1}$. Since no difference was observed, we concluded that $\overline{M1}$ had no significant effect on our accidentals subtraction. Our six-fold cross sections as a function of m' for symmetric h^+h^- and $\pi^+\pi^-$ pairs ($|P_\perp'| < 1.1$ GeV/c) are shown in Fig. 42.

The six-fold cross section is related to the correlation function R in a very simple way.

$$E_1E_2\frac{d^6\sigma}{dp_1^3\,dp_2^3} = \frac{1}{\sigma_{inel}} R \; E_1\frac{d^3\sigma}{dp_1^3} \; E_2\frac{d^3\sigma}{dp_2^3}$$

We can also relate this to $\frac{dN}{dx_e}$.

$$E_1E_2\frac{d^6\sigma}{dp_1^3\,dp_2^3} = \frac{\frac{dN}{dx_e} \; E_1 \; \frac{d^3\sigma}{dp_1^3}}{0.065 \; p_{\perp 1} \; p_{\perp 2}}$$

Hence for symmetric pairs where $x_e \cong 1$, x_e scaling implies $E_1E_2\frac{d^6\sigma}{dp_1^3\,dp_2^3}$ as a function of $p_{\perp 1} = p_{\perp 2} = m'/2$ should have the $p_{\perp 1}$ dependence of the single hadron invariant cross section divided by $p_{\perp 1}^2$.

From the relationship between $E_1E_2\frac{d^6\sigma}{dp_1^3\,dp_2^3}$ and R, we see that if the single hadron invariant cross section were linear exponential ($\propto e^{ap_\perp}$), the $P_\perp'$ dependence of the

six-fold cross section would be the same as the $P_\perp'$ dependence of R (see Fig. 34). Because the exponential slope of $E\frac{d^3\sigma}{dp^3}$ increases (becomes less negative) with increasing $p_\perp$, the $P_\perp'$ dependence of $E_1E_2\frac{d^6\sigma}{dp_1^3\,dp_2^3}$ should be even milder than that of R. Our measurements are shown in Fig. 43. Indeed the cross section is very flat as a function of $P_\perp'$. Similar measurements for the various species combinations were difficult due to the small number of events collected, as shown in Fig. 44. The "tilts" of these curves (for example, the $m' = 6.6$ curves for π^+K^- and $P^+\pi^-$) are consistent with $R(P_\perp')$ for all species being symmetric about $P_\perp' = 0$.

According to our A dependence findings, (see Fig. 36), our cross sections for symmetric pairs vs. m' should not change in shape when we correct for A dependence, but should simply be divided by $A^{1.0\pm0.05}$. The six-fold cross section vs. $P_\perp'$ will change in shape, however. Using a simple fit to our pair α, $\alpha = 0.98 + \frac{P_\perp'^2}{40}$, we show the A-dependence correction factor on Fig. 43 by which the beryllium data of that figure should be multiplied in order to convert to cross section per nucleon.

VII. F. s Dependence

By comparing measurements using 400, 300 and 200 GeV incoming protons, we were able to determine the s dependence of the cross sections and correlation functions. It should be noted, however, that at 300 and 200 GeV, our center of mass rapidity ranges were no longer centered around 0. (See Table IV.) In fact, in the 200 GeV center of mass frame, back to back hadron pairs were not accepted into our apparatus. Fortunately (due to a broad spectrum of quark longitudinal momenta within the beam protons), the production of hadron pairs is rather insensitive to the rapidity of the pair.[8] Our acceptance vs. pair rapidity (which was close to the average rapidity of the two hadrons), generated by Monte-Carlo, is shown in Fig. 45.

The correlation function R for the three beam energies is shown in Fig. 46. Note the slight decrease in R (at constant m') with increasing beam energy. Figure 47 shows the test of x_e scaling at 200 and 300 GeV. The 300 GeV data exhibit x_e scaling, but, due to the paucity of events, no conclusion can be drawn from the 200 GeV data. Note the slight increase in $\frac{dN}{dx_e}$ (at $x_e \cong 1$) with increasing beam energy. Hence from the definitions of R and $\frac{dN}{dx_e}$, at constant $p_\perp$, the s dependence of

the pair cross section is somewhere between that of the single hadron cross section and the square of the single hadron cross section.

In its simplest form, the quark-quark scattering picture predicts the s dependence of the single hadron invariant cross section to be[6]

$$E\frac{d^3\sigma}{dp^3} = f(x_\perp, \theta_{CM})\, p_\perp^{-4}$$

where the scaling variable $x_\perp \equiv \frac{2p_\perp}{\sqrt{s}}$. (That an invariant cross section describing point-like elastic scattering must be of this form is evident from simple dimensional analysis.) For symmetric pairs we generalize the definition of $x_\perp$ to $x_\perp \equiv \frac{m'}{\sqrt{s}}$, so that $x_\perp$ is the fraction of available CM energy associated with the transverse motion of the two hadrons. The power of $p_\perp$ for the symmetric $E_1E_2\frac{d^6\sigma}{dp_1^3\, dp_2^3}$ is predicted by the simple quark-quark scattering picture to be -6, as one can see by dimensional analysis.

We followed the procedure of the Chicago-Princeton collaboration[3] in fitting our cross sections to the form

$$E\frac{d^3\sigma}{dp^3} = A\,(1 - x_\perp)^b\, p_\perp^{\,k}$$

Our results are presented in Table XXVI . Our π^+ cross sections for the three beam energies are shown together with the $x_\perp > 0.17$ fit in Fig. 48 . Since the cross sections are plotted as functions of $x_\perp$, the $p_\perp$ dependence can be measured from the vertical displacements between the 200, 300 and 400 GeV curves. Note that these displacements are not perfectly constant as a function of $x_\perp$, which is why the fits over the two different $x_\perp$ ranges in Table XXVI produced slightly different values for k. Since the A dependence corrections changed the shape of our single hadron cross sections only slightly, the fit parameters b and k were relatively insensitive to our conversion to cross section per nucleon. $E_1E_2 \frac{d^6\sigma}{dp_1^3 dp_2^3}$ for $\pi^+\pi^-$ and the $x_\perp > 0.17$ fit are shown in Fig. 49 . Assuming its A-dependence for all energies corresponds to $\alpha_{pair} \cong 1$ (the measurements described in Section VII. B were made only at 400 GeV), the b and k fit parameters are independent of A dependence corrections. From Table XXVI we conclude that the fit parameter k for the symmetric pair invariant cross sections is typically 1 (+0.5, -1.0) unit more negative than k for the single hadron invariant cross sections.

The deviation of the $p_\perp$ dependence of the single hadron invariant cross section from $p_\perp^{-4}$ is thought to be due in part (up to two powers of $p_\perp$) to net $P_\perp$ smearing.[22] Since the symmetric pair cross section is immune to such effects, R. D. Field suggested we measure this by comparing the energy dependence of the cross section for symmetric pairs to that for single hadrons. Indeed the fit parameter k for symmetric pairs is closer to -6 than k for single hadrons is to -4 by 0.5 to 2.0 units.

VIII. CONCLUSION

Our many results are summarized as follows. Our single hadron cross sections are in very good agreement with those of Chicago-Princeton. Our particle ratios also agree with theirs. The A dependence for symmetric hadron pairs corresponds to $\alpha \cong 1$, in sharp contrast with the rise in the single hadron α as a function of $p_\perp$ to values greater than 1. The pair α, however, does rise significantly higher than 1 when $|P_\perp'|$ becomes large. Our correlation function R and the pair invariant six-fold differential cross section are both very mild functions of $P_\perp'$ ($= p_{\perp 1} - p_{\perp 2}$). The exponential rise of R with m' ($= p_{\perp 1} + p_{\perp 2}$) is directly related to the fact we observe x_e scaling when $p_{\perp trig} \gtrsim 2.7$ GeV/c. For m' > 6 GeV/c, R for each species combination appears to be the same given we compare pair cross sections and single hadron cross sections at the same $p_{\perp 1}$, $p_{\perp 2}$ in the quark-quark center of mass system (where $P_{\perp net} = 0$). For m' = 4 to 6 GeV/c, there seems to be an enhancement of K^+K^- and $P^+\overline{P}$ pairs above that expected assuming no species correlations. After making A dependence corrections, however, these enhancements disappear. The s dependence of the single hadron

invariant cross section is described by $p_\perp^{-8}$ at constant $x_\perp$, in agreement with previous measurements. For the pair invariant cross section it is roughly $p_\perp^{-9}$.

The fact we observe x_e scaling is an important, quantitative piece of evidence in support of the constituent scattering model. Our species correlation measurements are in agreement with the quark-quark scattering picture. Thus it appears we have probed the nucleon and have uncovered its substructure: point-like constituents which are most likely quarks.

APPENDIX: Details of the Cerenkov Counters

C1 was approximately 140 cm wide, 80 cm high and 760 cm long. It was made in three 254 cm long sections. The walls were made of two sheets of aluminum separated by ~4 cm of plastic honeycomb, making the Cerenkov counters quite sturdy but relatively light. The mirrors were aluminum-coated glass with a film (~500 Å) of MgF_2 over the reflecting surface. This prevented oxidation of the aluminum which would have decreased the reflectivity of ultraviolet light. During the experiment, the C1's were continuously flushed with helium which kept the pressure within the Cerenkov counters at a constant 3 cm of water above atmosphere. The phototubes had to be out of contact with the C1 gas, since helium will slowly penetrate glass, ruining phototubes in a matter of months. This was accomplished with quartz windows, which filtered out no more ultraviolet light than did the faces of the RCA C3100M phototubes. Even though almost all the Cerenkov light was focused upon the 2-inch diameter phototube faces, Winston cones were used to assure complete light collection. The downstream section of C1 is drawn in Fig. 50.

C2 was 160 cm wide, 80 cm high and 450 cm long and was made in two sections. Its construction was similar to that of

C1 except in it were 5-inch Amperex 58 DVP's (with no Winston cones) in direct contact with the gas. Since the majority of Cerenkov light is ultraviolet, most of which is unable to pass through the face of 58 DVP phototubes, we coated the faces of the tubes with an organic wavelength shifter, p-terphenyl (pT), which absorbed UV light and reradiated visible light. The type and thickness of the wavelength shifter was arrived at after experimentation at a test beam. The thickness of the pT coat was varied from 50 to 500 $\mu G/cm^2$ with no apparent change in light collectability. Another wavelength shifter, tetraphenyl-butadiene (TPB), was also tested and found to work about as well as pT. After a month, however, the TPB became cloudy and ineffective. pT supposedly also will age, especially when exposed to air, although we had no such problems during the course of our experiment. The coats of pT we decided upon were 200 $\mu G/cm^2$ thick. We evaporated the pT onto the tube faces under a vacuum of about 5×10^{-5} torr. The N_o of the tubes increased from the standard 60 ± 2 to 150 ± 20 with wavelength shifter: a factor of 2½ more Cerenkov light collected.

Since the C2 gas was a variable mixture of neon and nitrogen, the index of refraction was measured three times a day.

This was done with the interferometer of Fig. 51. A laser beam was split into two parallel beams, one of which traveled through air, the other which traveled through a cell which was evacuated or filled with Cerenkov gas. When the beams were recombined, they either constructively or destructively interfered depending on differences in their optical path lengths. The differences in optical path lengths across the cross section of the beams produced light and dark bands in the recombined beam. The lens enlarged this interference pattern before it illuminated the viewing screen. (It was crucial to place the lens after the beams were recombined, otherwise temperature gradients in the gas cell would drastically distort the interference pattern during a measurement.) When gas was slowly let into the evacuated cell, the optical path length in the cell increased, making the light and dark bands move across the screen. The number of bands which crossed the screen was counted electronically with the aid of two phototransistors (two in order to detect forward and backward movement). When the cell was completely filled, the number of bands that crossed the screen center was related to the index of refraction (n) of the gas in the cell by

$$\#\ \text{bands} = \frac{L}{\lambda}\ (n - 1)$$

where L is the length of our gas cell (1.026 m) and λ is the wavelength of the laser light (6.328×10^{-7} m). Typical numbers of bands were 56 for helium, 210 for 67% Ne, 33% N_2 and 430 for N_2. A correction had to be made to take into account different temperatures in the Cerenkov counters and the gas cell. Another correction was made because n is dependent on the frequency of the light. (n was measured with red laser light. Cerenkov light is predominantly in the UV region.) Although this dependence is well known for the gases we used,[23] we were not sure just what regions of the ultraviolet spectrum we were sensitive to. After direct observation of Cerenkov thresholds (Fig. 16), we arrived at a frequency correction factor of 1.08 for both C1 and C2 by which we multiplied our measured n - 1. (For the expected thresholds of Fig. 16, we used first guess frequency corrections for C1 and C2 of 1.04 and 1.10 respectively.) Uncertainties in the measurements of n - 1 are estimated to be ± 4%, which corresponds to uncertainties in the threshold momenta of only ± 2%.

REFERENCES

[1] F. W. Busser et al., Phys. Lett. 46B, 471 (1973).

[2] The literature substantiating the prediction of jets is numerous. See the report of P. Darriulat at the Tbilisi Conference (1976).

[3] D. Antreasyan et al., Phys. Rev. Lett. 38, 112 (1977).

[4] Our dielectron experiment is described in great detail in the theses of D. C. Hom and H. D. Snyder, Columbia University (1978).

[5] R. D. Kephart et al., Phys. Rev. Lett. 39, 1440 (1977).

[6] Theoretical papers on quark-quark scattering include R. D. Field and R. P. Feynman, Phys. Rev. D 15, 2590 (1977); R. P. Feynman, R. D. Field, and G. C. Fox, Nucl. Phys. B128, 1 (1977).

[7] Brookhaven measurements by J. Hudis et al., Phys. Rev. 129, 434 (1963) and J. B. Cumming et al., Phys. Rev. C 14, 1554 (1976).

[8] M. Della Negra et al., Nucl. Phys. B127, 1 (1977).

[9] Particle Data Group, Rev. Mod. Phys. 45 (1963).

[10] J. D. Jackson, Classical Electrodynamics, Chapter 14.

[11] For further details on the water calorimeter, see B. C. Brown et al., IEEE Trans. Nucl. Sci. 25, 347 (1968).

[12] B. C. Brown, Fermilab Preprint TM-268 (1975).

[13] J. W. Cronin et al., Phys. Rev. D 11, 3105 (1975) and private communication with M. J. Shochet.

[14] L. Kluberg et al., Phys. Rev. Lett. 38, 670 (1977).

[15] M. L. Good, Y. Kazama, and C. N. Yang, Phys. Rev. D 15, 1920 (1977).

[16] G. Berlad, A. Dar, and G. Eilam, Phys. Rev. D 13, 161 (1976); G. Farrar, Phys. Lett. 56B, 185 (1975).

[17] R. L. McCarthy et al., Phys. Rev. Lett. 40, 984 (1978).

[18] M. Jacob, CERN Academic Training Programme, January, 1978.

[19] C. Bromberg et al., Phys. Rev. Lett. 38, 1447 (1977).

[20] R. J. Fisk et al., Phys. Rev. Lett. 40, 984 (1978).

[21] That the shift in $p_\perp$ is of the order 1 GeV/c is based upon D. M. Kaplan et al., Phys. Rev. Lett. 40, 435 (1978).

[22] R. D. Field, private communication.

[23] A. Dalgarus and A. E. Kingston, Proc. Roy. Soc. 259, 424 (1960).

[24] A paper is now being written by H. Jöstlein et al. about our experimental results and their possible significance.

TABLE I

TARGET PROPERTIES

Target	Width (cm)	Length (cm)	A	Density (gm/cm^3)	Absorption Length (cm)	$\frac{\#\ int.\ protons}{\#\ inc.\ protons}$	L_{eff} (cm)
Be 7	0.0222	10.271	9.012	1.848	37.1 ± 10%	0.242 ± 8.7%	8.971 ± 1.3%
Be 3	0.203	"	"	"	"	"	"
W	0.0417	1.275	183.85	19.3	9.85 ± 10%	0.121 ± 9.4%	1.196 ± 0.6%

TABLE II

N CALIBRATION CONSTANTS

	N/SEM	C_{XS} $\left(\frac{cm^2}{nuclei}\right)$	C_R	σ_{inel} $\left(\frac{cm^2}{nuclei}\right)$
Be @ 400 GeV	100.5 ± 5%	8.98×10^{-31} ± 7%	243,000 ± 11%	2.18×10^{-25} ± 10%
Be @ 300 GeV	96.0 ± 6%	8.58×10^{-31} ± 8%	254,000 ± 12%	2.18×10^{-25} ± 10%
Be @ 200 GeV	89.7 ± 5%	8.02×10^{-31} ± 7%	272,000 ± 11%	2.18×10^{-25} ± 10%
W @ 400 GeV	77.6 ± 5%	1.016×10^{-29} ± 7%	158,000 ± 12%	1.605×10^{-24} ± 10%
$\frac{W}{Be}$ @ 400 GeV	0.772 ± 7%	11.31 ± 7.5%	0.649 ± 14%	7.36 ± 14%

TABLE III

FIDUCIAL VOLUME

	z	Up Arm	z	Down Arm
Target	0	x = -2.3, 2.3	0	x = -2.3, 2.3
Production Angles		θ_x = 0.0485, 0.0945 θ_y = -0.0040, 0.0035		θ_x = 0.0485, 0.0945 θ_y = -0.0035, 0.0040
Collimators	152.8	x = -5.08, 5.08 y = -0.635, 0.635	152.8	x = -5.08, 5.08 y = -0.635, 0.635
Tungsten Collimator	676	y = -3.05, 2.24	676	y = -2.64, 2.64
Magnet Center	1123		1127	
Magnet Exit	1324	x = -35.6, 35.6 y = -2.03, 9.89	1328	x = -35.6, 35.6 y = -2.03, 9.89
Chamber 1Y	2416	y = 10.64, 49.7	2413	y = 10.83, 49.9
Lead Glass	3655	x = -83.3, 84.3 y = 24.1, 91.8 (x < 6.9) = 24.1, 101.5 (x > 6.9)	3659	x = -78.7, 88.9 y = 23.9, 91.7 (x < 1.3) = 23.9, 101.3 (x > 1.3)

Lengths in cm, Angles in radians

TABLE IV

CM RAPIDITY RANGES

	400 GeV	300 GeV	200 GeV
$\sqrt{s}$	27.430	23.764	19.418
γ_{CM}	14.617	12.664	10.348
$\theta_{LAB} \leftrightarrow 90^{o}_{CM}$	0.0683 rad	0.0788 rad	0.0963 rad
θ_{CM}	70.7^{o} to 108.4^{o}	63.2^{o} to 100.4^{o}	53.3^{o} to 88.9^{o}
y_{CM}	-0.326 to 0.343	-0.183 to 0.487	0.019 to 0.689

TABLE V

SCINTILLATION COUNTER INEFFICIENCIES (%)

Running Conditions for Mass Range:		4-5 GeV	5-6 GeV	6-10 GeV
T Trigger	UP	3.5	4.4	7.3
	DN	2.8	3.8	6.0
T1 Requirement	UP	0.1	0.1	0.3
	DN	0.6	0.7	1.4
V1 Requirement	UP	0.8	0.9	1.3
	DN	0.6	0.8	0.8
V2 Requirement	UP	0.7	0.7	0.6
	DN	0.3	0.4	0.4
TOTAL	UP	5.0	6.0	9.3
	DN	4.2	5.6	8.4

TABLE VI

WIRE CHAMBER GEOMETRY

	Z (cm)	Wire Spacing (cm)	Angle from Horizontal	# Wires
JY	1427	0.212	0	79
JV	1427	0.212	60^{o}	304
1Q	2388	0.203	-7.125^{o}	272
1P	2402	0.203	7.125^{o}	272
1Y	2416	0.203	0	192
2Y	2975	0.300	0	192
3Q	3503	0.298	-7.125^{o}	352
3P	3517	0.298	7.125^{o}	352
3Y	3531	0.300	0	280

TABLE VII

WIRE CHAMBER INEFFICIENCIES (%)

		Running Conditions for Mass Range		
		4-5 GeV	5-6 GeV	6-10 GeV
JY	UP	2.6	3.4	4.6
	DN	2.0	3.0	5.5
JV	UP	0.8	1.1	1.6
	DN	4.2	5.7	6.3
1Q	UP	1.1	1.4	2.2
	DN	1.0	1.4	2.3
1P	UP	4.2	4.7	4.3
	DN	2.0	2.2	2.9
1Y	UP	1.4	1.7	3.2
	DN	1.7	2.3	3.7
2Y	UP	2.2	2.6	3.5
	DN	3.3	4.0	5.7
3Q	UP	1.6	1.9	2.1
	DN	1.4	1.7	2.0
3P	UP	1.3	1.9	2.1
	DN	2.8	3.7	3.7
3Y	UP	2.0	2.0	2.4
	DN	1.3	1.7	2.5
TOTAL	UP	0.3	0.4	0.7
	DN	0.3	0.5	1.0

TABLE VIII

MATERIAL IN SECONDARY BEAM

		Material	Length (cm)	Radiation Length (cm)	% Radiation Length	Z (cm)
1	Target	Be	0.12 to 0.23	35.3	0.3 to 0.6	0
		W	0.22 to 0.43	0.35	63.0 to 123.0	
2		He	585	477000.0	0.1	
3	Target Box Window	Kapton	0.013	28.7	-	585
4		Air	91	31000.0	0.3	
5	Shielding Pile Window	Mylar	0.025	28.7	0.1	676
6		Vacuum				
7	Magnet Exit Window	Mylar	0.025	28.7	0.1	1324
8		Air	103	31000.0	0.3	
9	JY, JV				-	1427
10		Air	164	31000.0	0.5	
11	C1 Entrance Window	Mylar	0.028	28.7	0.1	1591
12		He	766	477000.0	0.2	
13	C1 Mirror	Glass	0.15	10.6	1.4	2324
14	C1 Exit Window	Mylar	0.035	28.7	0.1	2357
15		Air	45	31000.0	0.1	
16	1Q, 1P, 1Y	Aℓ Screen	0.0068	8.9	0.1	2402
17	V1	Pilot Y	0.32 or 0.64	42.9	0.7 or 1.5	2456
18	T0	Pilot Y	0.64	42.9	1.5	2467
19		Air	92	31000.0	0.3	
20	C2 Entrance Window	Mylar	0.035	28.7	0.1	2494
21		C2 Gas	452	34300.0	1.3	
22	C2 Mirror	Glass	0.25	10.6	2.4	2915
23	C2 Exit Window	Mylar	0.035	28.7	0.1	2946
24		Air	29	31000.0	0.1	
25	2Y	Aℓ Screen	0.0023	8.9	-	2975
26	T1	Pilot Y	0.64	42.9	1.5	3034
27		Air	542	31000.0	1.7	
28	3Q, 3P, 3Y					3517

TABLE IX

CERENKOV INEFFICIENCIES (%)

(Measured with Electrons)

	Inefficiency (%)	Inefficiency Due to Impurities in Electron Sample (%)
C1 up	0.16	~ 0.15
C1 dn	0.10	
C2 up	0.08	~ 0.02
C2 dn	0.02	

% OF TIMES CERENKOVS FIRED

WHEN THEY SHOULD NOT HAVE

Running Conditions for Mass Range:		4-5 GeV	5-6 GeV	6-10 GeV
C1 up	> 0.2 P. E.	1.8	5.1	11.5
	> 1.0	0.8	2.1	4.9
C1 dn	> 0.2	2.2	5.6	8.0
	> 1.0	1.1	2.5	3.9
C2 up	> 0.3	5.5	12.1	14.8
	> 0.7	3.0	7.0	9.6
C2 dn	> 0.3	3.7	7.4	11.8
	> 0.7	2.3	5.0	7.9

TABLE X

CERENKOV GASES

C1:

	Gas	n - 1	Pion Identification Momentum Band
	He	3.72×10^{-5}	8-56 GeV/c

C2:

Mass Range	Gas	n - 1	Triple Identification Momentum Band
4-5 GeV	N_2	2.86×10^{-4}	22-39 GeV/c
5-6 GeV	42% Ne, 58% N_2	1.93×10^{-4}	30-50 GeV/c
Asymmetric 5-6 GeV	UP: N_2 DN: 67% Ne, 33% N_2	UP: 2.86×10^{-4} DN: 1.40×10^{-4}	UP: 22-39 GeV/c DN: 35-55 GeV/c
6-10 GeV	67% Ne, 33% N_2	1.40×10^{-4}	35-55 GeV/c

TABLE XI

π, K, P SAMPLES: LOSSES AND CONTAMINATIONS (%)

				Running Conditions for Mass Range		
				4-5 GeV	5-6 GeV	6-10 GeV
π:	losses:	C1 or C2 inefficiencies		0.4	0.2	0.2
	cont:	K's with C1 accidentals	K^+	0.7	1.9	3.4
			K^-	0.4	1.1	2.0
K:	losses:	C1 accidentals or C2 inefficiencies		2.2	5.4	9.8
	cont:	π's with C1 inefficiencies	π^+	1.0	0.5	0.4
			π^-	1.8	0.9	0.7
		P's with C2 accidentals	P^+	3.1	6.9	10.1
			$\overline{P}$	2.3	4.9	6.7
P:	losses:	C1 or C2 accidentals	P^+	3.7	8.2	12.8
			$\overline{P}$	5.6	11.9	17.1
	cont:	K's with C2 inefficiencies	K^+	0.2	0.1	0.1
			K^-	0.3	0.1	0.1

TABLE XII

PROPERTIES OF CALORIMETER COMPONENTS

Material	Length (cm)	Abs. Length (cm)	# Abs. Length	Rad. Length (cm)	$\left\lvert \frac{dE}{dX} \right\rvert_{min}$ (MeV/cm)
Pb	1.27	18.5	0.1	0.56	12.8
Lead Glass	60.0	40.0	1.5	2.36	9.0
Steel	6.3	17.1	0.4	1.77	11.6
H_2O up arm	549.0	78.8	7.0	36.4	2.03
H_2O down arm	320.0		4.1		

TABLE XIII

CERENKOV THRESHOLDS FOR THE CALORIMETERS

Particle	Lead Glass		H_2O	
	n	E_{th}	n	E_{th}
π	1.673	0.17 GeV	1.33	0.21 GeV
K		0.62		0.75
P		1.17		1.42

TABLE XIV

PT AND MASS TRIGGER SETTINGS

	Mass Range (GeV)	Threshold Voltage (mV)	$p_\perp$ (or m') for which h^+ (or h^+h^-) Trigger Efficiency is 25%	50%	70%	85%
PT Trigger	4-5	52	1.4	1.8	2.2	2.7
	5-6	72	1.9	2.5	3.1	3.7
	Asymmetric 5-6	UP: 52 DN: 92				
	6-10	92	2.4	3.2	3.9	4.7
MH Trigger	4-5	32	2.5	3.1	3.6	4.2
	5-6	47	3.7	4.5	5.3	6.1
	6-10	62	4.8	5.9	6.9	8.0

($p_\perp$'s in GeV/c, Masses in GeV)

TABLE XV

RATES (Per a 1 Second Pulse)

	Mass Range (GeV)		
	4-5	5-6 (asymmetric)	6-10
INTENSITY (protons per pulse)	4×10^9	7×10^9	2×10^{10}
SINGLES RATES (per counter or wire chamber plane)	$\sim 1 \times 10^6$	$\sim 2 \times 10^6$	$\sim 5 \times 10^6$
LIVE TIMES:			
Spike Killer	0.95	0.95	0.95
SB Veto	1.00	1.00	0.95
Slow Logic Busy	1.00	0.99	0.95
Computer Busy	0.83	0.84	0.93
FAST TRIGGERS:			
TU	1.5×10^5	4.0×10^5	1.1×10^6
TD	1.6×10^5	4.2×10^5	1.3×10^6
TUD	1300	7400	56000
SLOW TRIGGERS:			
PTU	(÷ 1024) 17	(÷ 2048) 18	(÷ 1024) 10
PTD	(÷ 1024) 18	(÷512) 11	(÷ 1024) 10
PTUD	16	12	7
MHM1	41	18	24
MH	(÷ 8) 10	(÷ 8) 10	(÷ 8) 6
MM	(÷ 32) 7	(÷ 32) 12	(÷ 256) 4
Electron Pairs	1/2	3	5
TOTAL	96	72	58

TABLE XVI

NUMBER OF EVENTS PASSING TRACK QUALITY CUTS

Mass Range (GeV)			Slow Triggers	Simple Track Reconst.	Fiducial Cuts	Single Track Per Arm	Stringent Track Reconst.	E_{cal}/p Cut
4-5	PTU	(from 12.7K $TU^P/_S$)	1000	939	722	716	700	700
	PTD	(from 14.8K $TD^P/_S$)	1000	914	739	739	728	728
	MHM1	(from 21.4K TUD)	1000	640	378	377	368	362
5-6 (asym.)	PTU	(from 10.3K $TU^P/_S$)	1000	930	731	729	713	713
	PTD	(from 85.4K $TD^P/_S$)	1000	889	723	710	700	700
	MHM1	(from 115K TUD)	1000	704	452	450	436	432
6-10	PTU	(from 93K $TU^P/_S$)	1000	776	562	550	530	530
	PTD	(from 159K $TD^P/_S$)	1000	812	602	596	571	571
	MHM1	(from 2500K TUD)	1000	454	252	248	237	235

TABLE XVII

NUMBER OF T TRIGGERED EVENTS PASSING TRACK QUALITY CUTS

Mass Range (GeV)		Triggers	Simple Track Reconstruction	Fiducial Cuts	Single Track Per Arm	Stringent Track Reconstruction	E_{cal}/p Cut
	TU	1000	371	239	237	229	225
4-5	TD	1000	277	162	161	157	148
	TUD	1000	117	58	56	56	54
	TU	1000	321	201	199	191	186
5-6	TD	1000	255	154	153	147	134
	TUD	1000	104	40	40	37	35
	TU	1000	104	53	52	46	43
6-10	TD	1000	130	66	64	60	57
	TUD	1000	13	3	3	3	3

TABLE XVIII

PERCENTAGE OF TRACKS WITH MORE THAN ONE TRACK PER ARM

	Mass Range (GeV)		
	4-5	5-6	6-10
Up Arm	0.3	0.6	2.2
Down Arm	0.2	0.8	1.4

TABLE XIX

$\overline{M1}$ EFFICIENCIES FOR HADRON PAIRS

Mass Range	Percentage of PTUD High Quality Pairs with $\overline{M1}$
4-5 GeV	87%
5-6 GeV	82%
6-10 GeV	79%

TABLE XX

RUNNING CONDITIONS

Mass Range (GeV)	Intensity (protons/pulse)	Magnet Current (amps)	50% Efficiency Points of PT in $p_\perp$ (GeV/c) MH in m'	Full Particle ID Momentum Band (GeV/c)
4-5	4×10^9	961	1.8 3.1	22-39
5-6	7×10^9	1288	2.5 4.5	30-50
5-6 asymmetric	7×10^9	961	up: 1.8 down: 3.2 4.5	up: 22-39 down: 35-55
6-10	2×10^{10}	961 or 1288	3.2 5.9	35-55

TABLE XXI

DATA SETS

Data Set (Mass Range in GeV)			N ($\times 10^6$)	Running Days @ 5000 Pulses/Day
400 GeV Protons on Beryllium:				
4-5:		+/-	7.3	1.2
		+/+	0.9	0.2
		-/-	0.9	0.2
5-6:		+/-	20.5	1.7
		+/+	3.4	0.3
		-/-	5.8	0.5
	asymmetric:	+/-	14.1	1.1
		+/+	5.1	0.5
		-/-	8.6	0.7
6-10:	961 amps:	+/-	324.0	10.2
	1288 amps:	+/-	405.0	8.7
		+/+	35.0	1.4
		-/-	92.0	3.1
400 GeV Protons on Tungsten:				
4-5:		+/-	1.0	0.2
5-6:		+/-	3.5	0.2
	asymmetric:	+/-	1.7	0.2
6-10:		+/-	35.0	1.4
300 GeV Protons on Beryllium:				
5-6:		+/-	53.2	2.0
		+/+	11.0	0.4
		-/-	32.5	1.2
	asymmetric:	+/-	105.5	5.5
		+/+	13.7	0.7
		-/-	36.7	1.7
200 GeV Protons on Beryllium (taken concurrently with 300 GeV runs):				
5-6:		+/-	41.5	1.6
		+/+	10.7	0.4
		-/-	23.3	0.9

TABLE XXII

B_{int} CUTS AND AVERAGES

Mass Range	B_{int} Cut	$\langle B_{int} \rangle$	$\frac{TUD_{real}}{TUD}$
4-5 GeV	25	16	0.011
5-6 GeV	50	30	0.007
6-10 GeV	110	70	0.0005

TABLE XXIII

$R(m')$ $\left|p_{\perp 1} - p_{\perp 2}\right| < 1.1$

m'	B_{int}	$R_{h^+h^-}$	Error	$R_{\pi^+\pi^-}$	Error
4.0	15	9.1	0.4	10.4	0.7
4.2	15	11.8	0.5	12.1	0.9
4.4	15	14.5	0.7	16.1	1.2
4.6	15	18.6	1.0	22.6	1.7
4.8	15	21.6	1.4	27.1	2.4
5.0	26	31.9	1.5	37.2	2.5
5.2	27	43.5	2.2	51.8	3.7
5.4	28	53.7	3.1	60.8	5.3
5.6	28	66.0	4.4	83.1	8.1
5.8	29	92.2	6.7	112.4	12.7
6.0	66	120.0	4.1	145.6	7.9
6.2	66	153.2	5.8	203.1	12.3
6.4	67	215.7	8.5	249.9	18.6
6.6	68	290.8	12.6	382	31
6.8	68	412.5	19.1	537	52
7.0	69	591	30	987	99
7.2	69	687	42	823	131
7.4	69	1034	67	1450	250
7.6	69	1252	97	1680	390
7.8	69	1843	154	3060	780
8.0	69	2840	250	4150	1330
8.2	70	3770	390		
8.4	70	4290	560		
8.6	70	4830	780		
8.8	70	8100	1340		
9.0	71	9850	1950		
9.2	71	11300	2800		
9.4	71	15500	4300		
9.6	72	17100	6100		
9.8	71	26700	10100		
10.0	71	40200	16400		

Errors shown are statistical only.

TABLE XXIV

SPECIES DEPENDENCE OF α

	π^-	K^-	$\overline{P}$
π^+	0.99 ± 0.03	1.05 ± 0.09	1.29 ± 0.14
K^+	0.98 ± 0.09	1.33 ± 0.17	-
P	1.11 ± 0.07	1.58 ± 0.21	1.37 ± 0.13

TABLE XXV

$R / R_{h^+h^-}$

Species	m' = 3.9-5.9 GeV/c		m' = 5.9-7.9 GeV/c	
	Be Data	A-Corrected	Be Data	A-Corrected
$\pi^+\pi^+$	1.03 ± 0.11		1.08 ± 0.16	
$\pi^+\pi^-$	1.15 ± 0.04	1.08 ± 0.10	1.28 ± 0.04	1.21 ± 0.11
$\pi^-\pi^-$	1.07 ± 0.11		0.97 ± 0.12	
$K^+\pi^+$	0.95 ± 0.13		0.91 ± 0.18	
$K^+\pi^-$	0.94 ± 0.07	0.96 ± 0.20	0.97 ± 0.07	0.99 ± 0.21
K^+K^+	0.79 ± 0.29		1.66 ± 0.53	
$K^-\pi^+$	0.83 ± 0.08	0.71 ± 0.16	0.67 ± 0.08	0.59 ± 0.13
$K^-\pi^-$	0.74 ± 0.14		0.88 ± 0.17	
K^-K^+	1.20 ± 0.16	0.59 ± 0.23	1.05 ± 0.16	0.53 ± 0.22
K^-K^-	1.00 ± 0.45		0.76 ± 0.52	
$P^+\pi^+$	0.64 ± 0.10		0.60 ± 0.14	
$P^+\pi^-$	0.87 ± 0.06	0.80 ± 0.13	0.72 ± 0.06	0.71 ± 0.12
P^+K^+	0.90 ± 0.18		0.54 ± 0.22	
P^+K^-	0.74 ± 0.12	0.25 ± 0.12	0.64 ± 0.13	0.24 ± 0.12
P^+P^+	0.47 ± 0.18		0.23 ± 0.23	
$\overline{P}\pi^+$	0.84 ± 0.11	0.47 ± 0.15	0.33 ± 0.10	0.20 ± 0.09
$\overline{P}\pi^-$	0.52 ± 0.17		0.49 ± 0.22	
$\overline{P}K^+$	0.75 ± 0.18		0.43 ± 0.18	
$\overline{P}K^-$	0.61 ± 0.37		0.07 ± 0.34	
$\overline{P}P^+$	1.15 ± 0.17	0.69 ± 0.22	0.39 ± 0.17	0.27 ± 0.14
$\overline{P}\overline{P}$	0.49 ± 0.67		0.00 ± 0.69	

TABLE XXVI

FITS TO SINGLE HADRON AND SYMMETRIC PAIR INVARIANT CROSS SECTIONS

$$E\frac{d^3\sigma}{dp^3} \text{ or } E_1E_2\frac{d^6\sigma}{dp_1^3\,dp_2^3} = A(1-x_\perp)^b\,p_\perp^k \quad \text{where } x_\perp = \frac{2p_\perp}{\sqrt{s}}\ ;\ p_\perp = \frac{m'}{2} \text{ for symmetric pairs}$$

	$x_\perp > 0.17$			$x_\perp > 0.24$		
Cross Section	A	b	k	A	b	k
Single π^+ (Be)	$(3.3\pm0.3)\times10^{-26}$	7.4 ± 0.5	-8.0 ± 0.1	$(5.5\pm1.5)\times10^{-26}$	6.1 ± 0.8	-8.9 ± 0.2
(AC)	$(4.4\pm0.4)\times10^{-27}$	7.4 ± 0.5	-8.4 ± 0.1	$(7.2\pm1.9)\times10^{-27}$	6.1 ± 0.8	-9.2 ± 0.2
π^- (Be)	$(2.9\pm0.2)\times10^{-26}$	9.1 ± 0.1	-7.5 ± 0.1	$(4.7\pm1.4)\times10^{-26}$	8.1 ± 0.8	-8.2 ± 0.2
(AC)	$(3.9\pm0.3)\times10^{-27}$	9.1 ± 0.1	-7.9 ± 0.1	$(6.5\pm1.7)\times10^{-26}$	8.1 ± 0.8	-8.6 ± 0.3
h^+ (Be)	$(13.0\pm0.7)\times10^{-26}$	8.3 ± 0.1	-8.5 ± 0.1	$(39.1\pm4.5)\times10^{-26}$	7.3 ± 0.2	-9.5 ± 0.1
h^- (Be)	$(6.9\pm0.4)\times10^{-26}$	11.2 ± 0.1	-7.6 ± 0.1	$(16.3\pm1.7)\times10^{-26}$	10.7 ± 0.2	-8.4 ± 0.1
Symmetric $\pi^+\pi^-$	$(1.6\pm0.3)\times10^{-28}$	12.8 ± 0.6	-8.7 ± 0.2	$(1.7\pm0.7)\times10^{-28}$	14.0 ± 0.8	-8.4 ± 0.2
h^+h^-	$(6.7\pm0.4)\times10^{-28}$	13.0 ± 0.4	-9.3 ± 0.1	$(8.4\pm1.9)\times10^{-28}$	13.7 ± 0.6	-9.2 ± 0.2
300 & 400 GeV Data Only						
Single π^+ (Be)	$(4.2\pm0.2)\times10^{-26}$	7.8 ± 0.9	-8.2 ± 0.2			
π^- (Be)	$(3.4\pm0.4)\times10^{-26}$	8.3 ± 0.3	-7.9 ± 0.2			
Symmetric $\pi^+\pi^-$	$(1.7\pm0.4)\times10^{-28}$	10.8 ± 1.2	-9.2 ± 0.4			

Be = Beryllium data. AC = A dependence corrected.
All errors are statistical. Systematic error on k = ±0.5.

THE QUARK-QUARK SCATTERING PICTURE

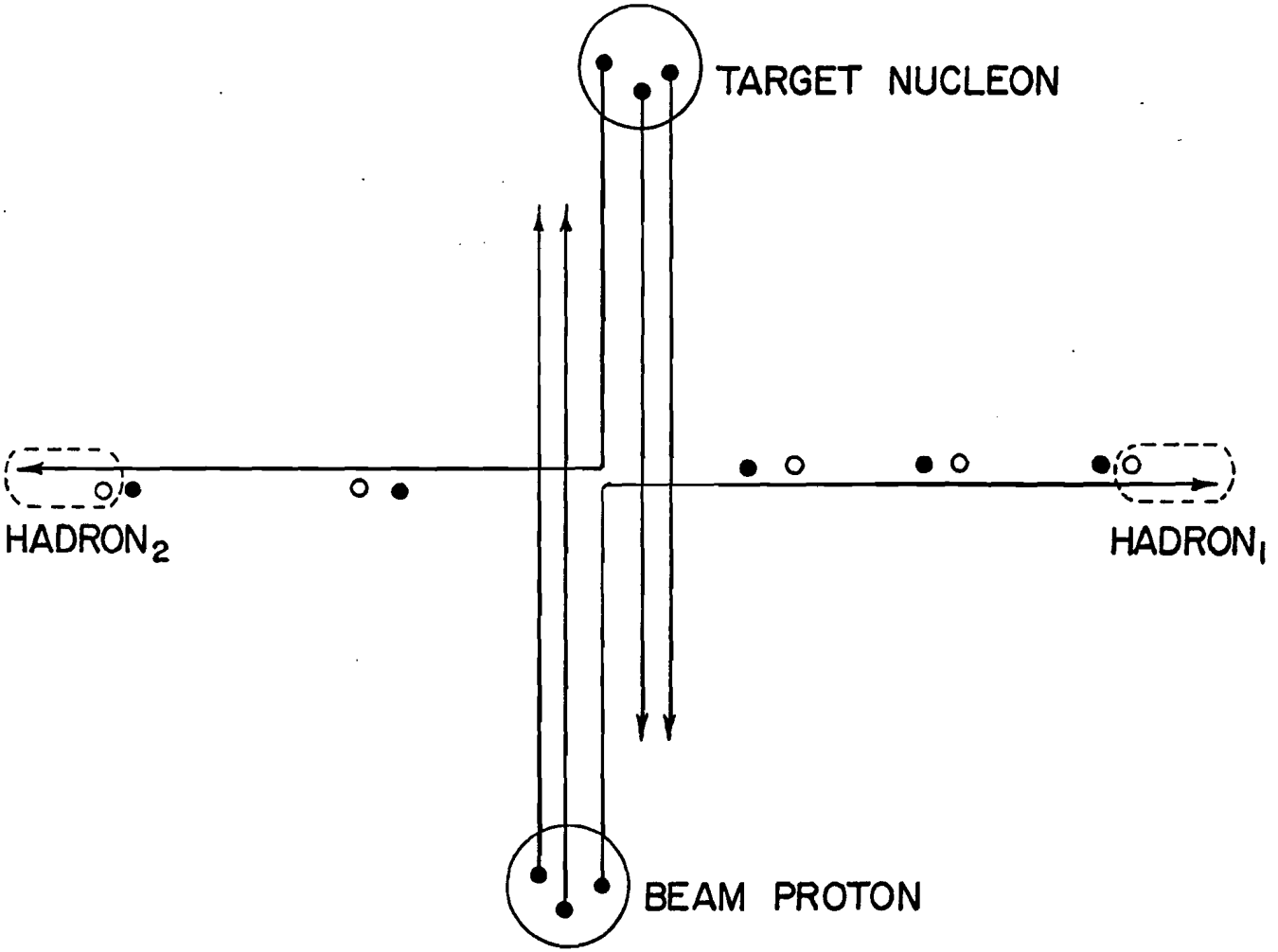

FIGURE 1

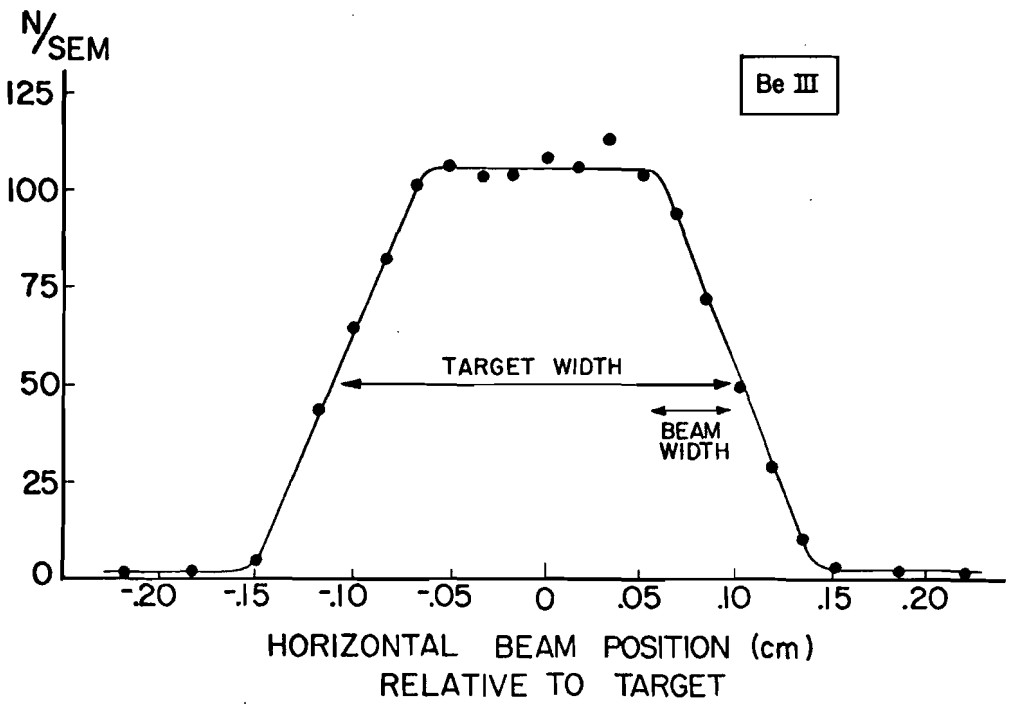
N/SEM
125
100
75
50
25
0
Be III
TARGET WIDTH
BEAM WIDTH
-.20
-.15
-.10
-.05
0
.05
.10
.15
.20
HORIZONTAL BEAM POSITION (cm)
RELATIVE TO TARGET

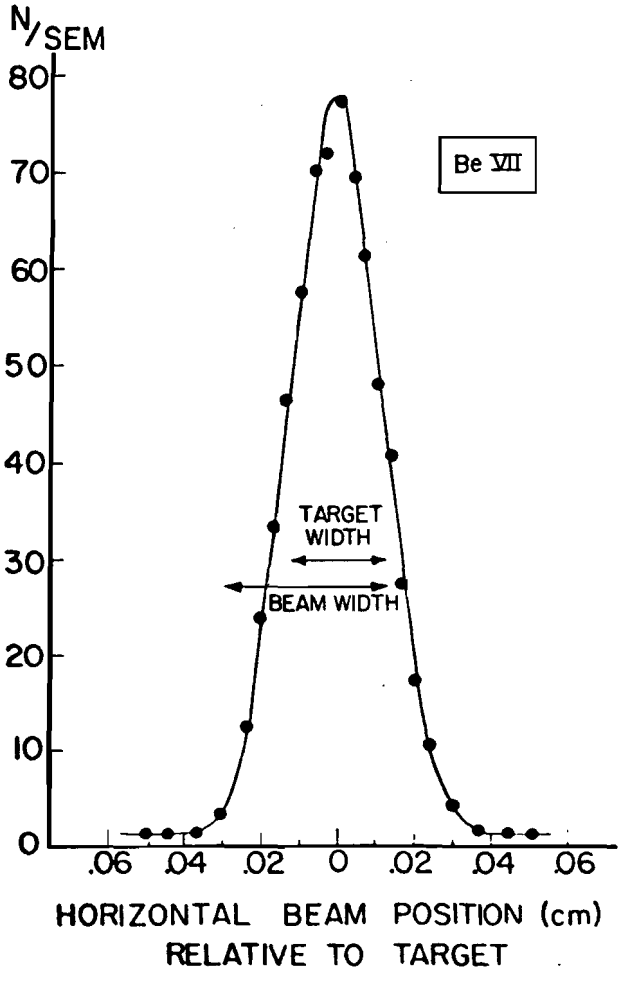
N/SEM
80
70
60
50
40
30
20
10
0
Be VII
TARGET WIDTH
BEAM WIDTH
.06
.04
.02
0
.02
.04
.06
HORIZONTAL BEAM POSITION (cm)
RELATIVE TO TARGET

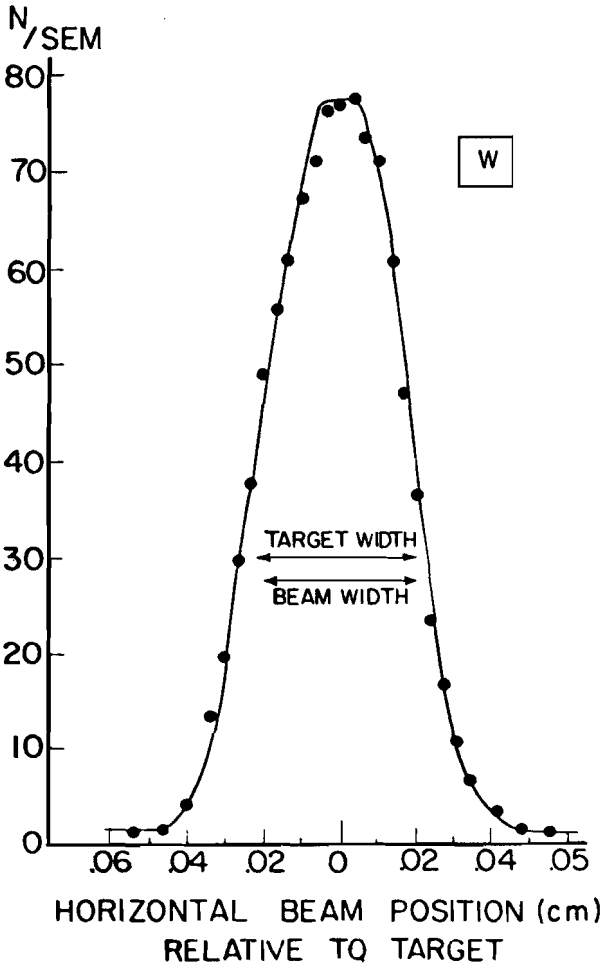
N/SEM
80
70
60
50
40
30
20
10
0
W
TARGET WIDTH
BEAM WIDTH
.06
.04
.02
0
.02
.04
.05
HORIZONTAL BEAM POSITION (cm)
RELATIVE TO TARGET

FIGURE 2

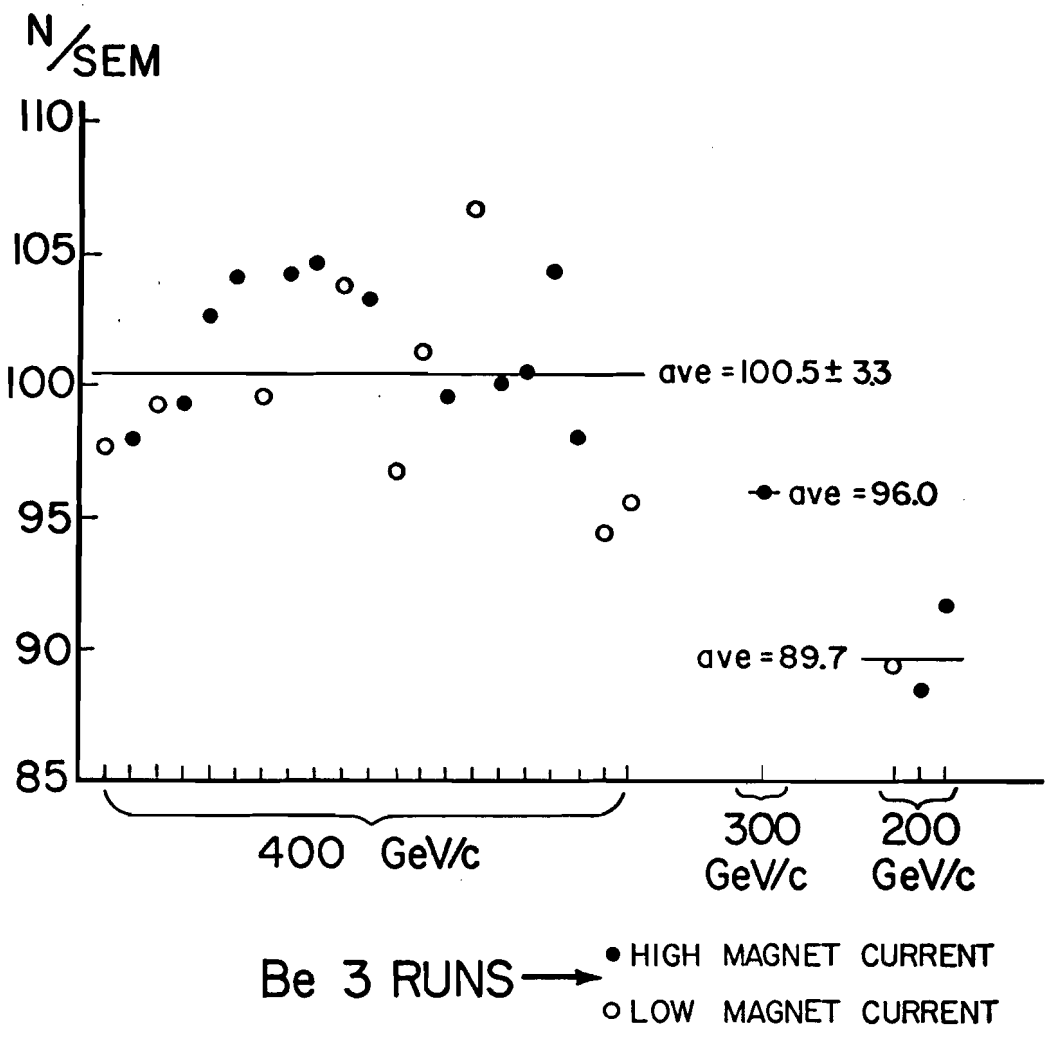
N/SEM
110
105
100
95
90
85
ave = 100.5 ± 3.3
ave = 96.0
ave = 89.7
400 GeV/c
300 GeV/c
200 GeV/c
Be 3 RUNS
HIGH MAGNET CURRENT
LOW MAGNET CURRENT

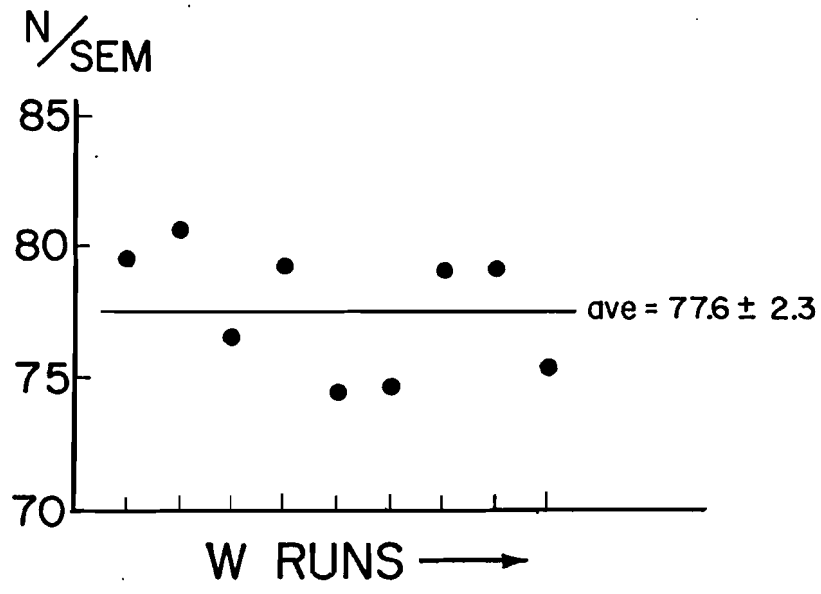
N/SEM
85
80
75
70
ave = 77.6 ± 2.3
W RUNS

FIGURE 3

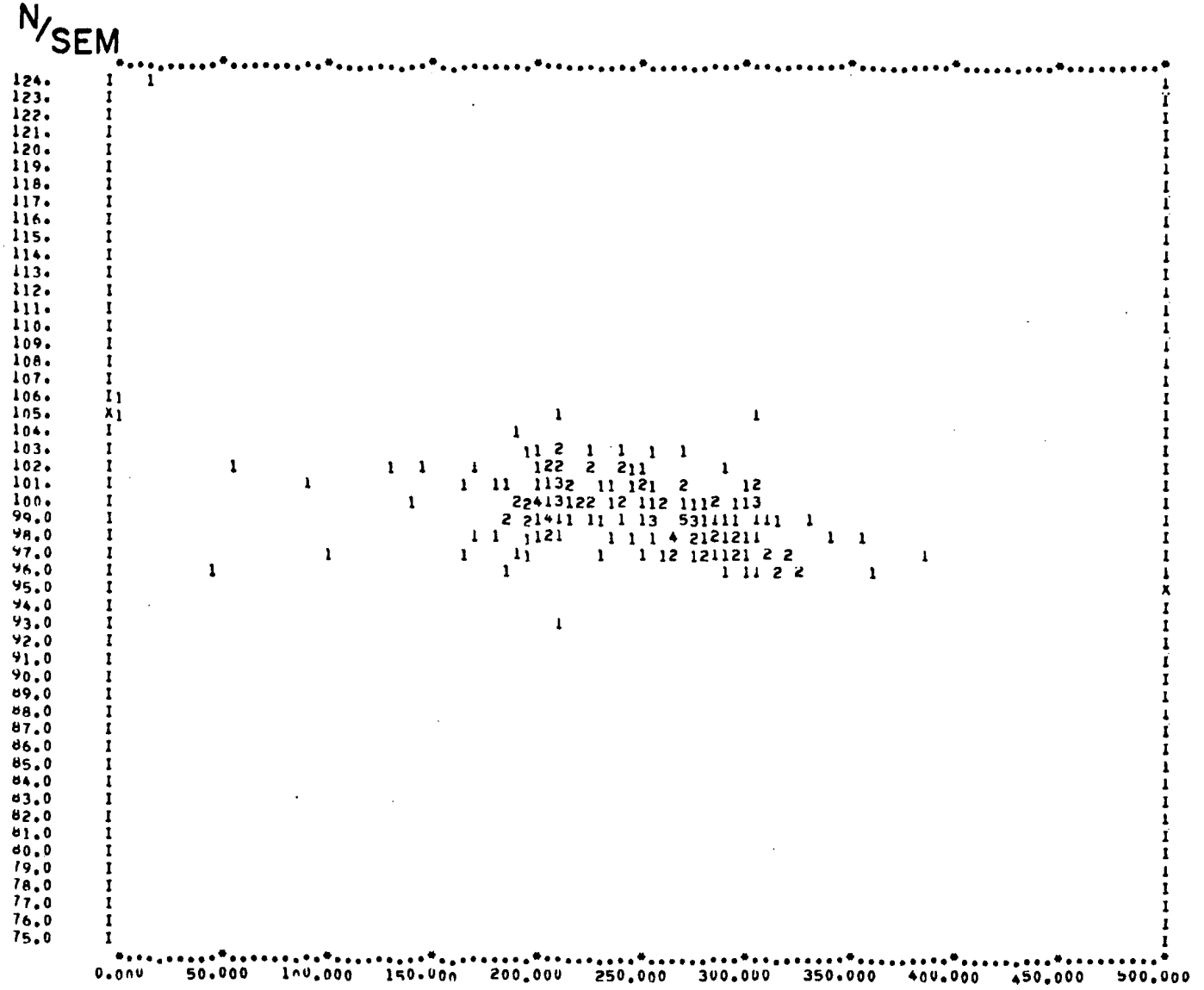
N/SEM
124.
123.
122.
121.
120.
119.
118.
117.
116.
115.
114.
113.
112.
111.
110.
109.
108.
107.
106.
105.
104.
103.
102.
101.
100.
99.0
98.0
97.0
96.0
95.0
94.0
93.0
92.0
91.0
90.0
89.0
88.0
87.0
86.0
85.0
84.0
83.0
82.0
81.0
80.0
79.0
78.0
77.0
76.0
75.0
0.000
50.000
100.000
150.000
200.000
250.000
300.000
350.000
400.000
450.000
500.000
SEM

FIGURE 4

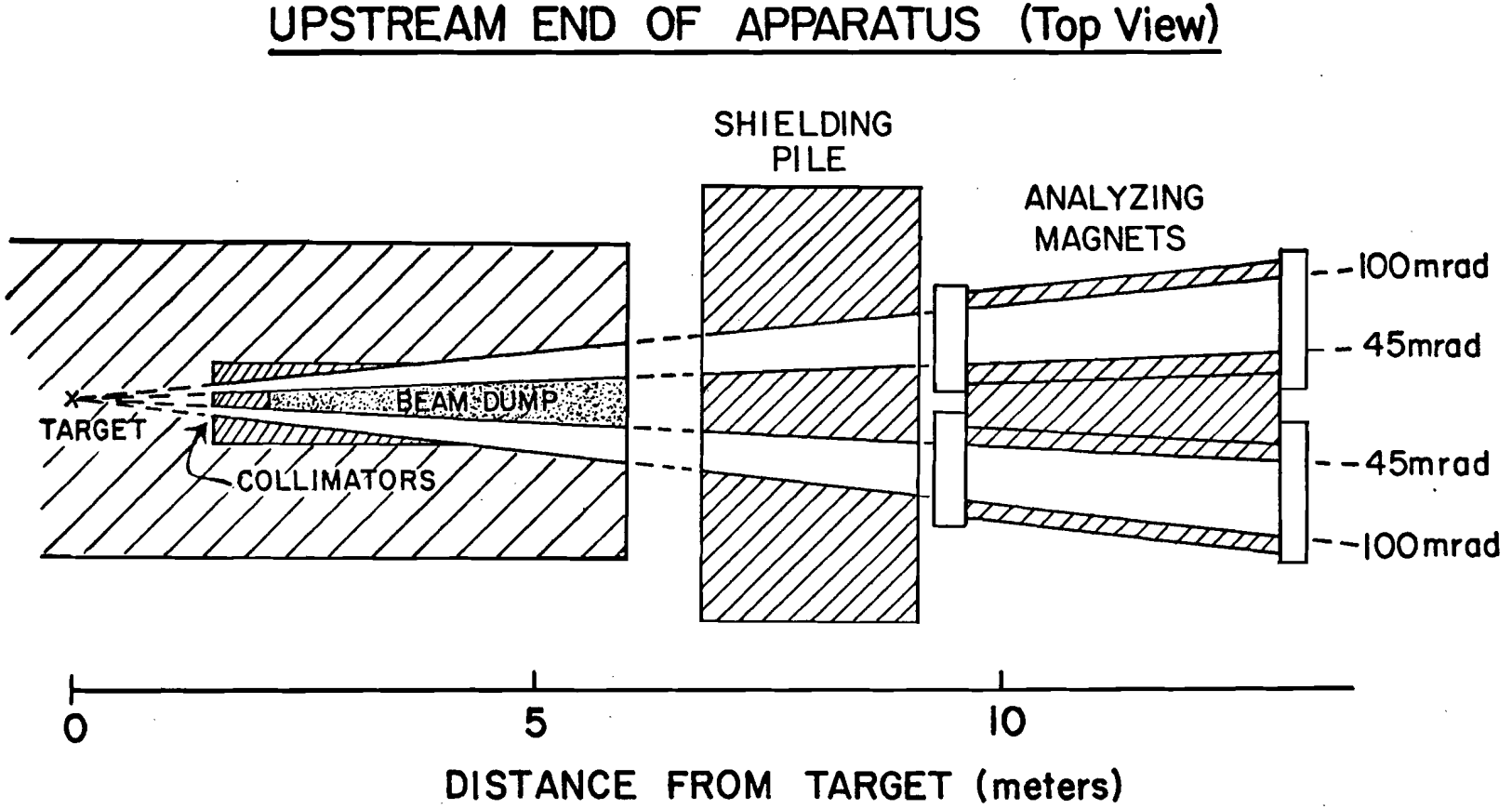
UPSTREAM END OF APPARATUS (Top View)
SHIELDING PILE
ANALYZING MAGNETS
100mrad
45mrad
45mrad
100mrad
BEAM DUMP
TARGET
COLLIMATORS
0
5
10
DISTANCE FROM TARGET (meters)

FIGURE 5

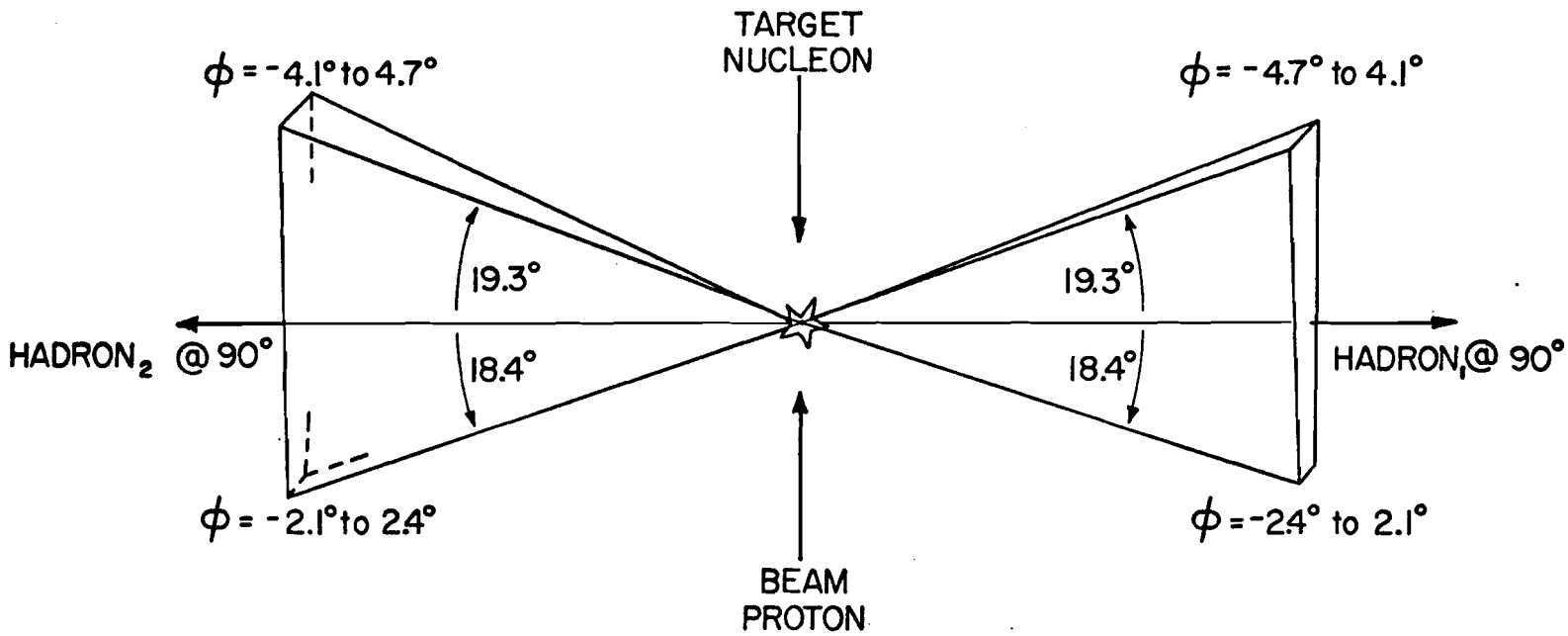
CENTER OF MASS ACCEPTANCE @ 400 GeV (top view)
TARGET NUCLEON
ϕ = -4.1° to 4.7°
ϕ = -4.7° to 4.1°
19.3°
19.3°
HADRON$_2$ @ 90°
18.4°
18.4°
HADRON$_1$ @ 90°
ϕ = -2.1° to 2.4°
ϕ = -2.4° to 2.1°
BEAM PROTON

FIGURE 6

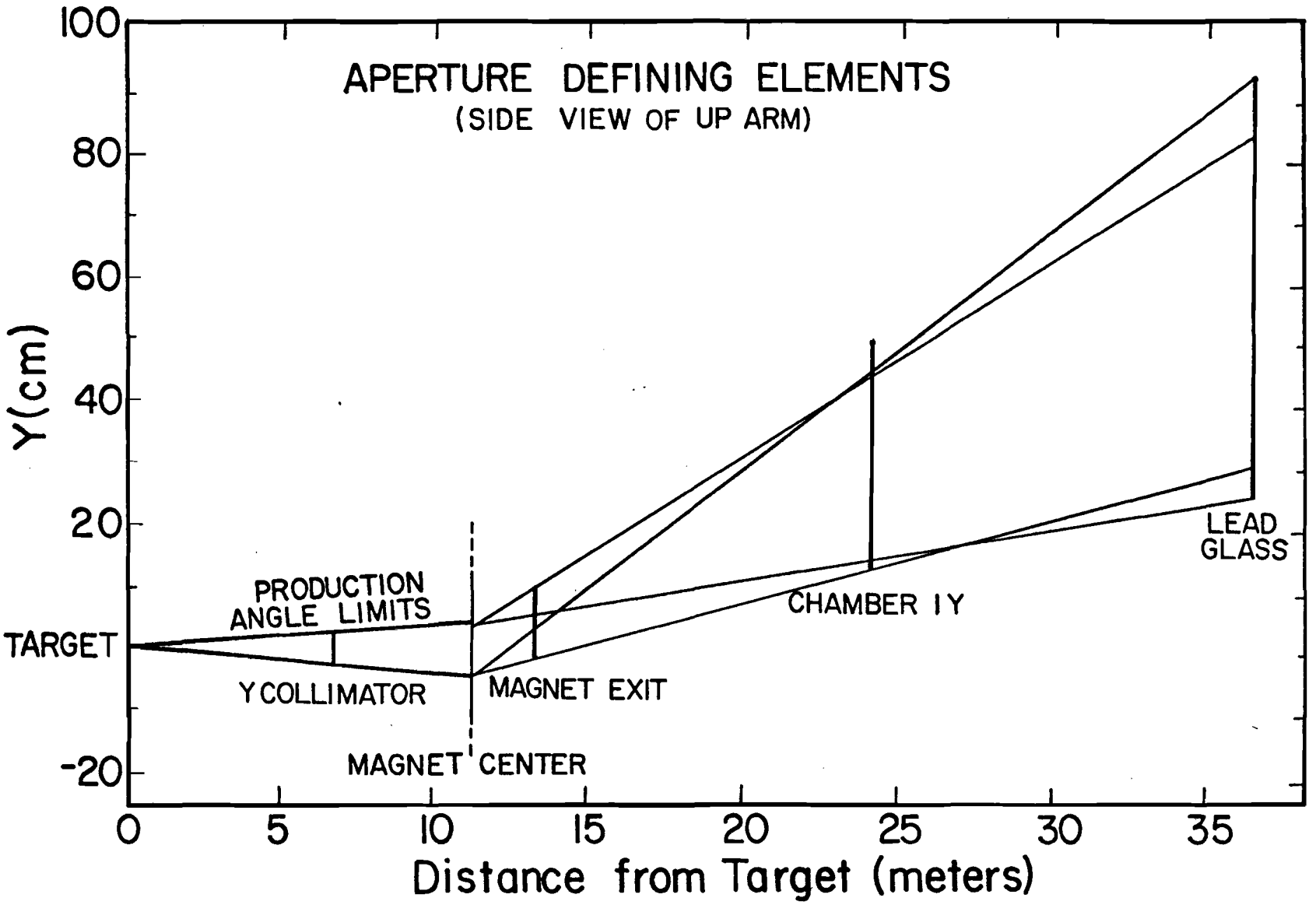
APERTURE DEFINING ELEMENTS
(SIDE VIEW OF UP ARM)
Y(cm)
100
80
60
40
20
TARGET
-20
PRODUCTION
ANGLE LIMITS
Y COLLIMATOR
MAGNET EXIT
MAGNET CENTER
CHAMBER I Y
LEAD
GLASS
0
5
10
15
20
25
30
35
Distance from Target (meters)

FIGURE 7

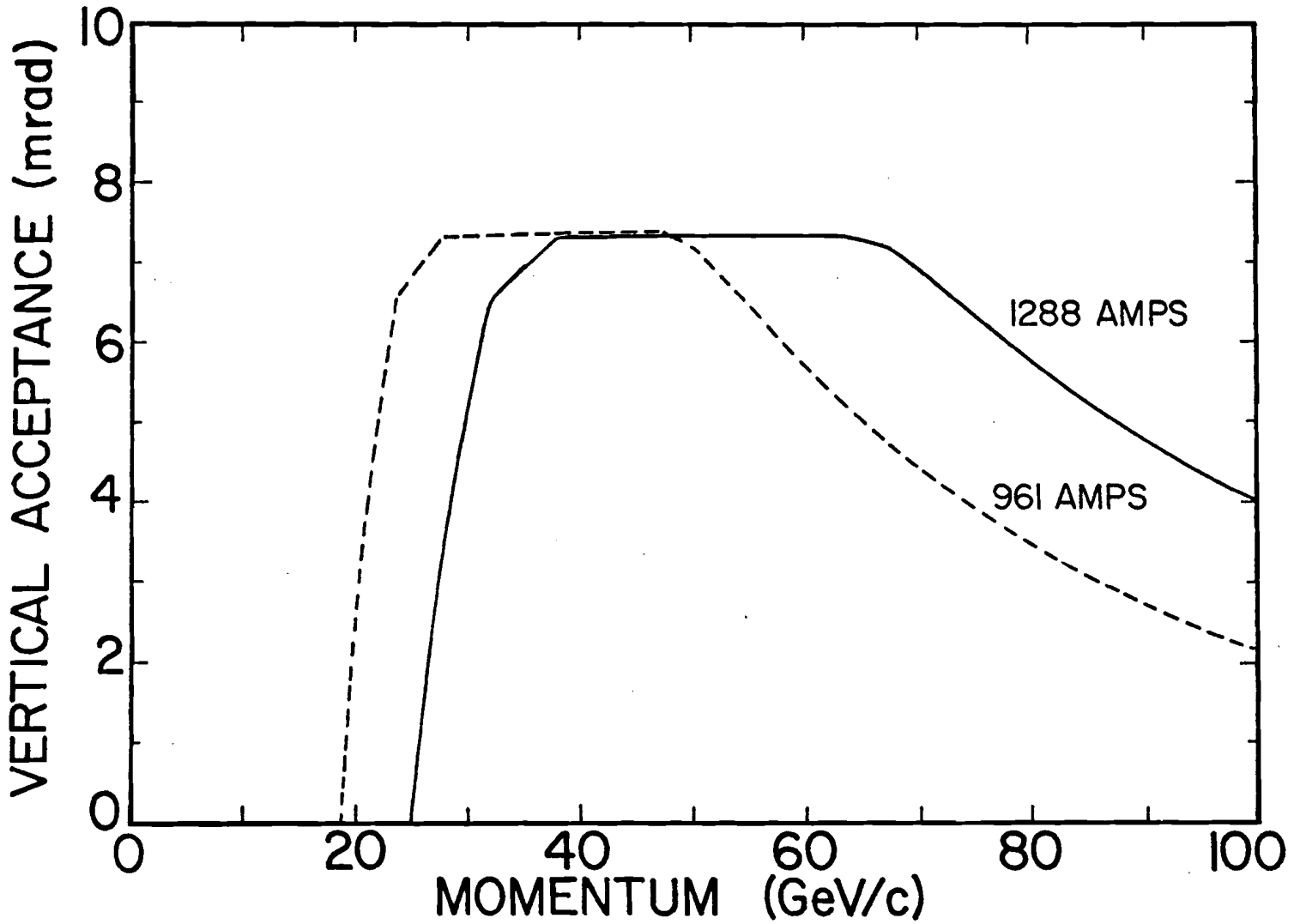
VERTICAL ACCEPTANCE (mrad)
0
2
4
6
8
10
0
20
40
60
80
100
MOMENTUM (GeV/c)
1288 AMPS
961 AMPS

FIGURE 8

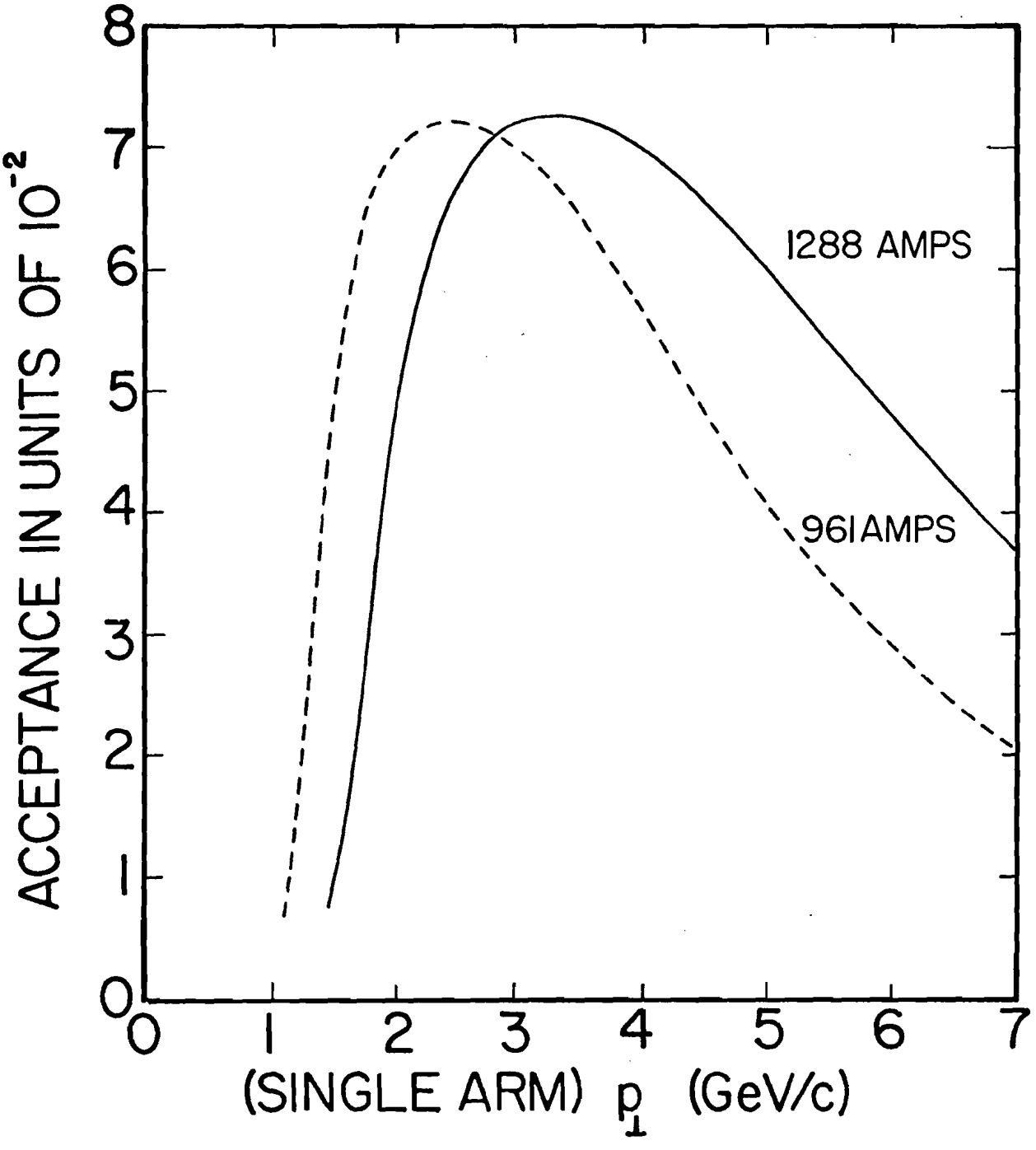
ACCEPTANCE IN UNITS OF 10^{-2}
0
1
2
3
4
5
6
7
8
1288 AMPS
961 AMPS
0
1
2
3
4
5
6
7
(SINGLE ARM) $p_\perp$ (GeV/c)

FIGURE 9

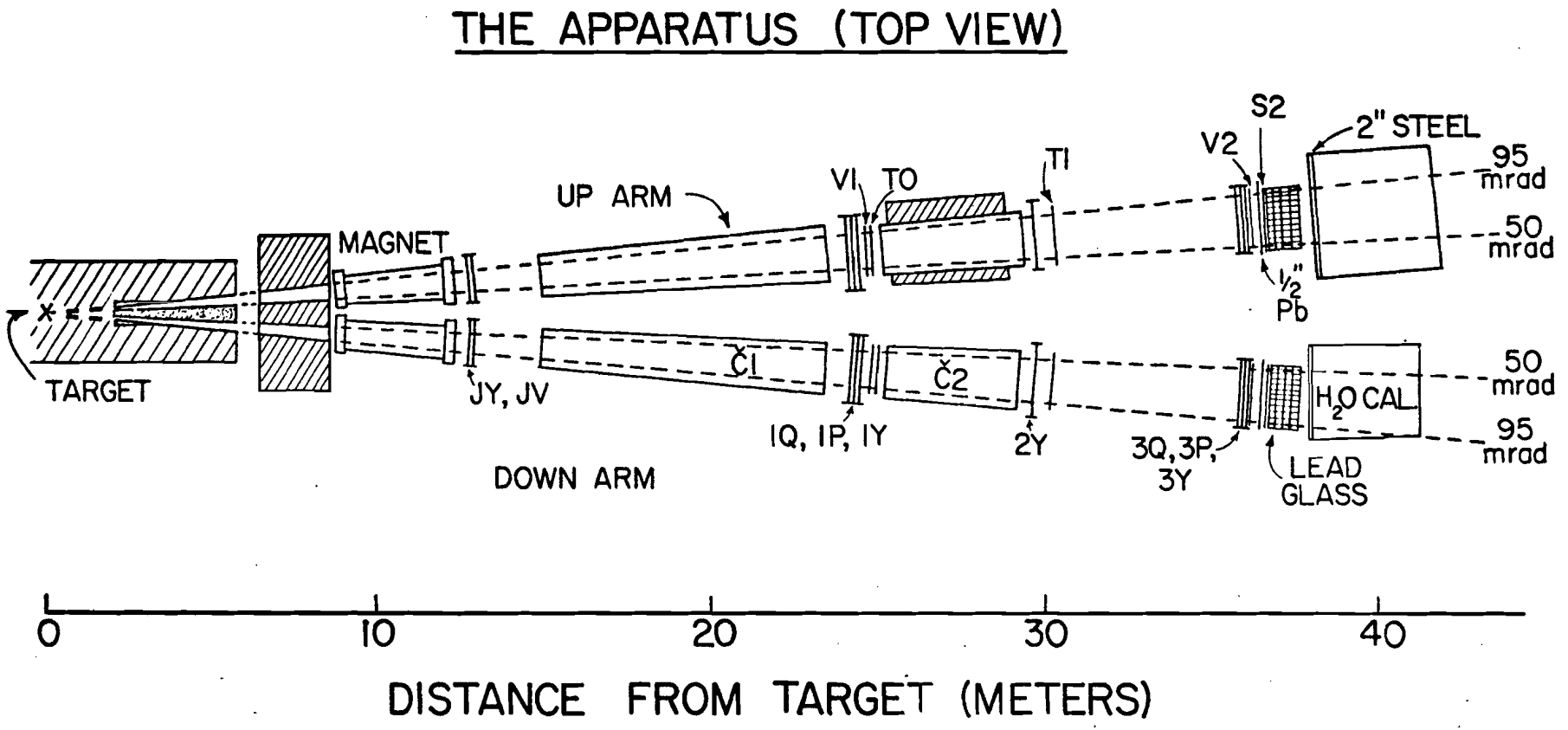
THE APPARATUS (TOP VIEW)
S2
2" STEEL
V2
95 mrad
50 mrad
UP ARM
VI
TO
TI
MAGNET
½" Pb
TARGET
JY, JV
C1
C2
50 mrad
H2O CAL
95 mrad
IQ, IP, IY
2Y
3Q, 3P, 3Y
LEAD GLASS
DOWN ARM
0
10
20
30
40
DISTANCE FROM TARGET (METERS)

FIGURE 10

TRIGGER COUNTER GEOMETRY

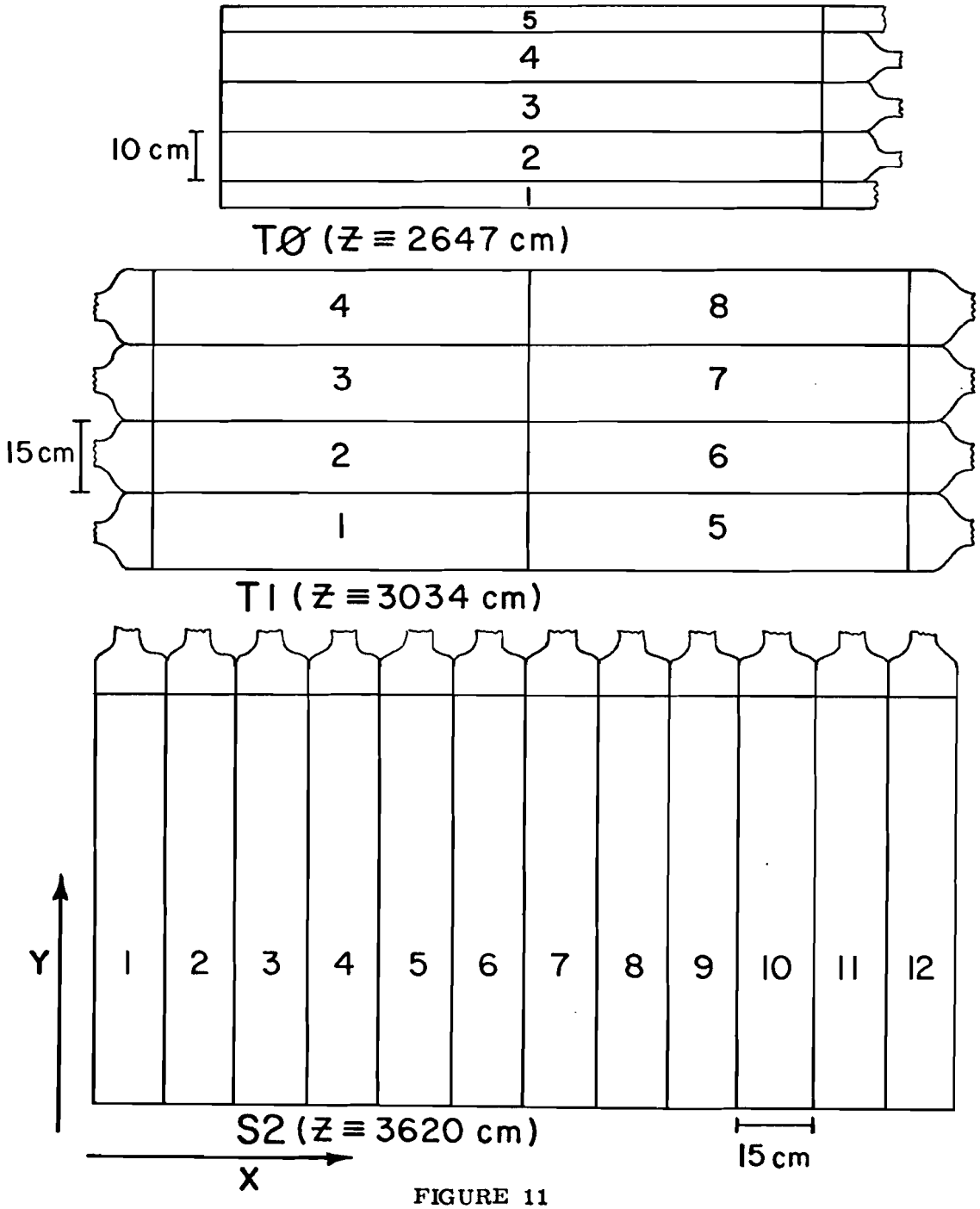

FIGURE 11

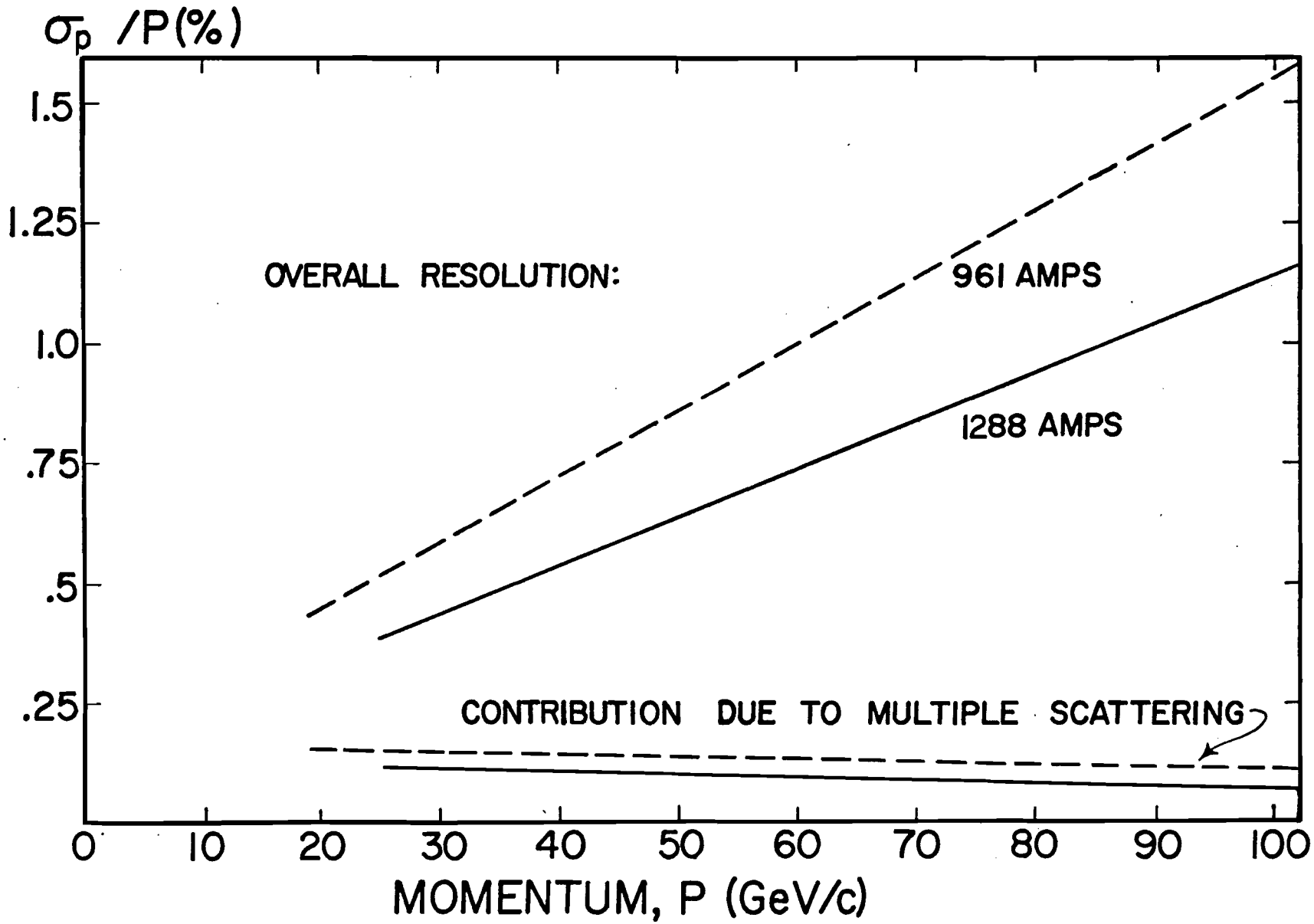
σp /P(%)
1.5
1.25
1.0
.75
.5
.25
OVERALL RESOLUTION:
961 AMPS
1288 AMPS
CONTRIBUTION DUE TO MULTIPLE SCATTERING
0
10
20
30
40
50
60
70
80
90
100
MOMENTUM, P (GeV/c)

FIGURE 12

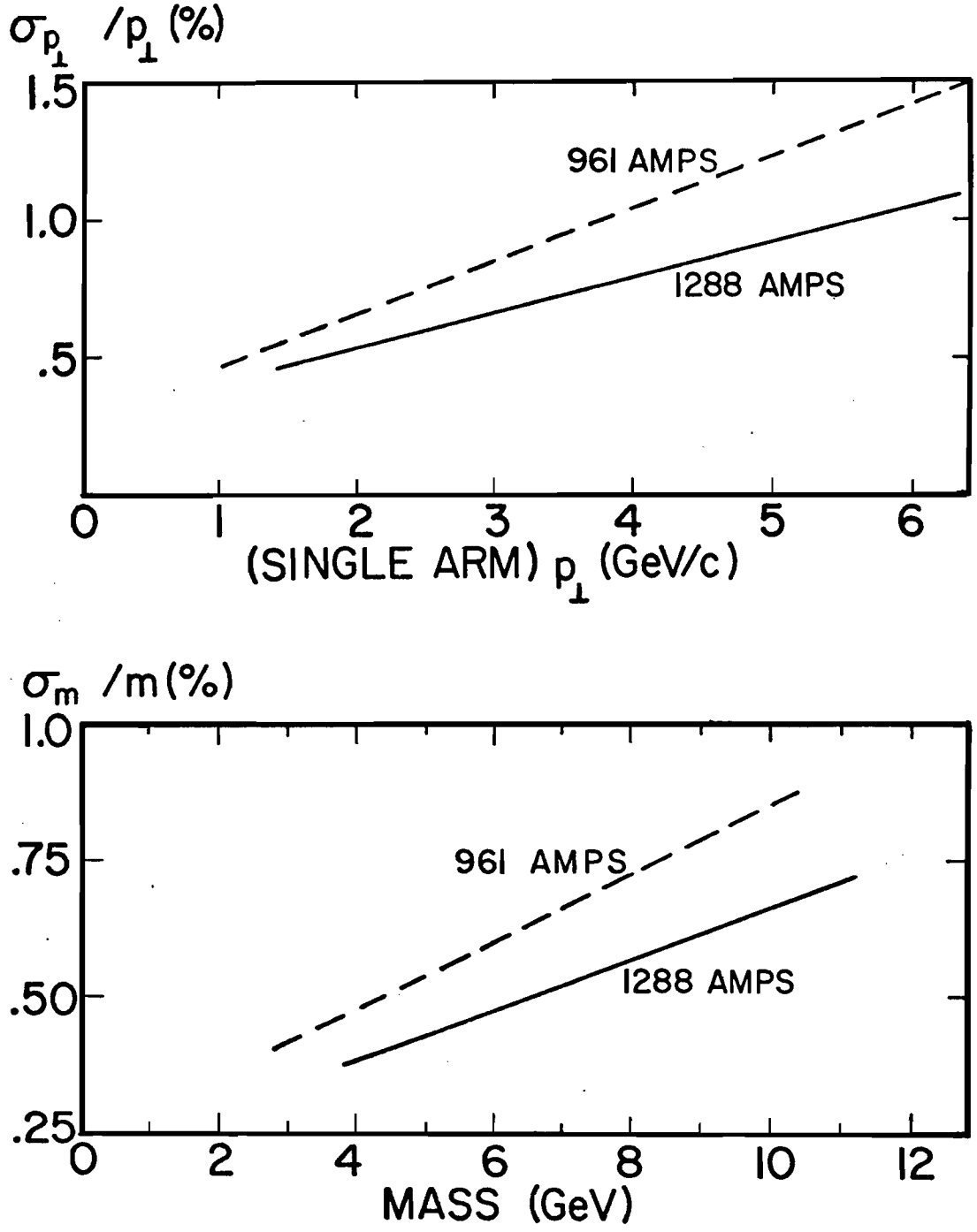
$\sigma_{p_\perp}/p_\perp$ (%)
1.5
1.0
.5
961 AMPS
1288 AMPS
0
1
2
3
4
5
6
(SINGLE ARM) $p_\perp$ (GeV/c)
σ_m/m (%)
1.0
.75
.50
.25
961 AMPS
1288 AMPS
0
2
4
6
8
10
12
MASS (GeV)

FIGURE 13

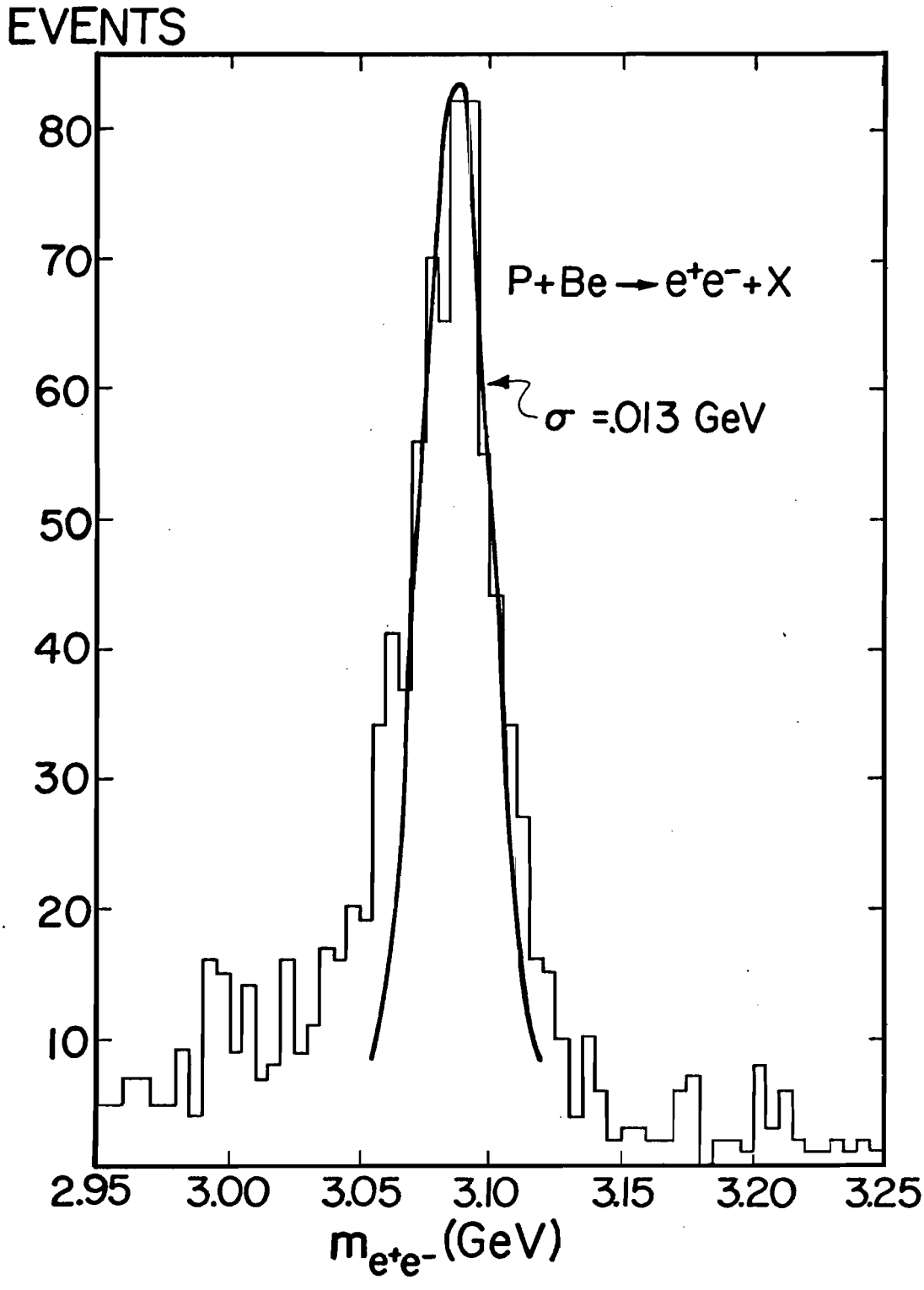
EVENTS
80
70
60
50
40
30
20
10
P+Be → e⁺e⁻+X
σ =.013 GeV
2.95
3.00
3.05
3.10
3.15
3.20
3.25
m e⁺e⁻ (GeV)

FIGURE 14

PARTICLE ID REGIONS FOR 67% Ne, 33% N_2

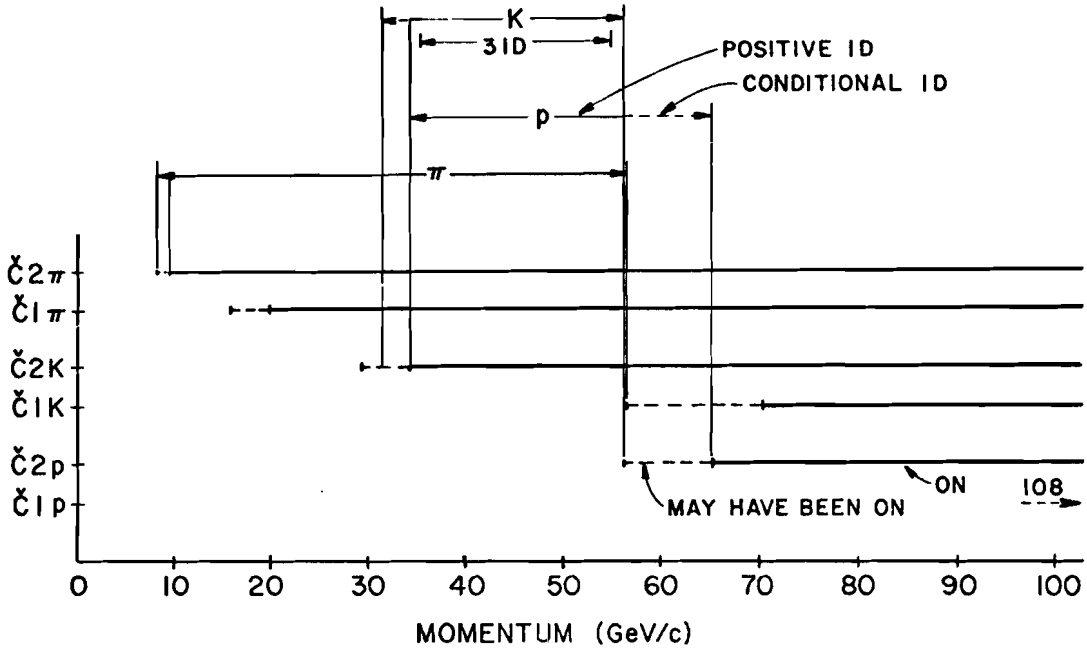

PARTICLE ID REGIONS FOR N_2

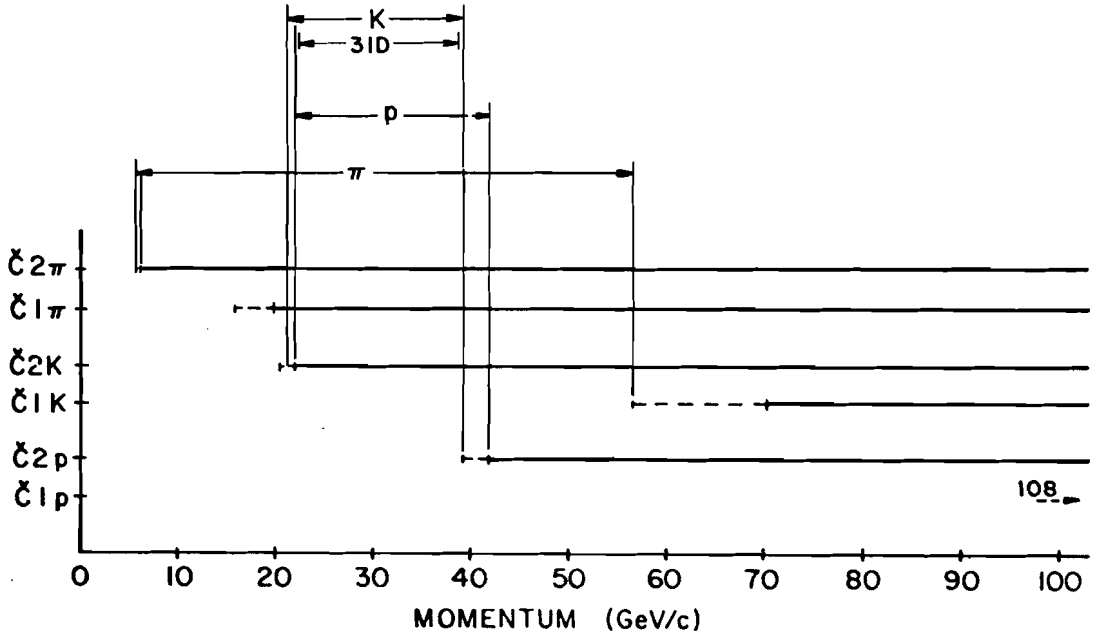

FIGURE 15

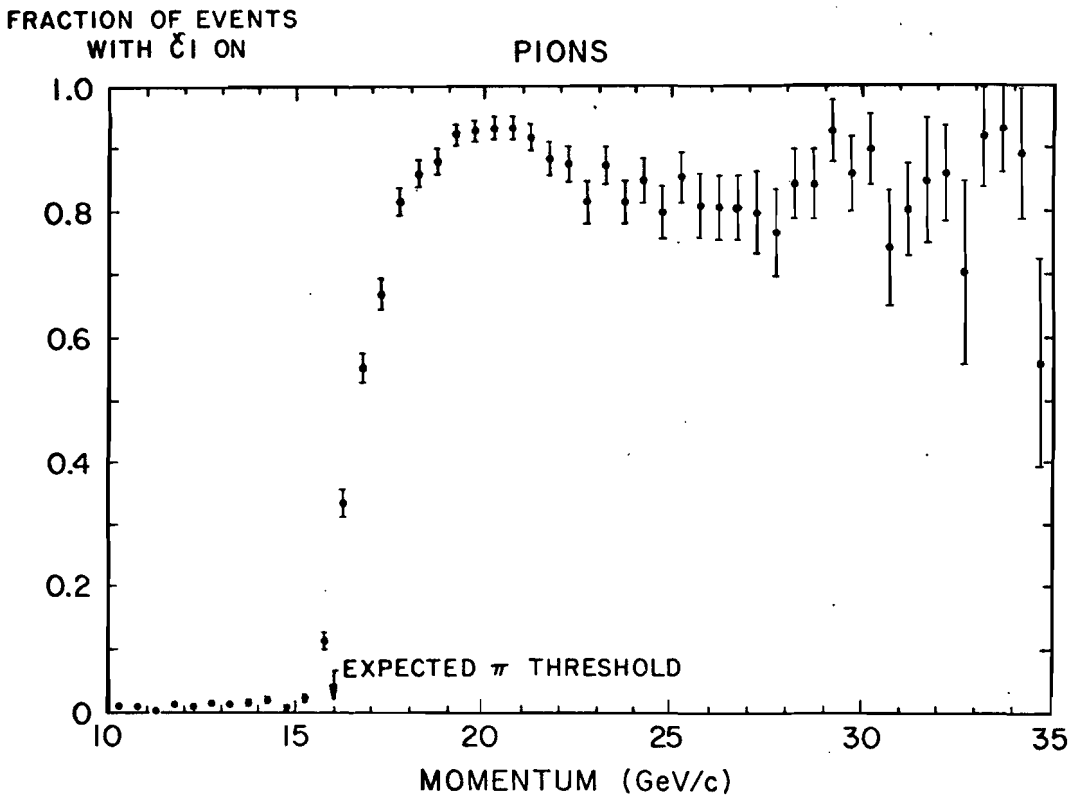
FRACTION OF EVENTS
WITH Č1 ON
PIONS
1.0
0.8
0.6
0.4
0.2
0
EXPECTED π THRESHOLD
10
15
20
25
30
35
MOMENTUM (GeV/c)

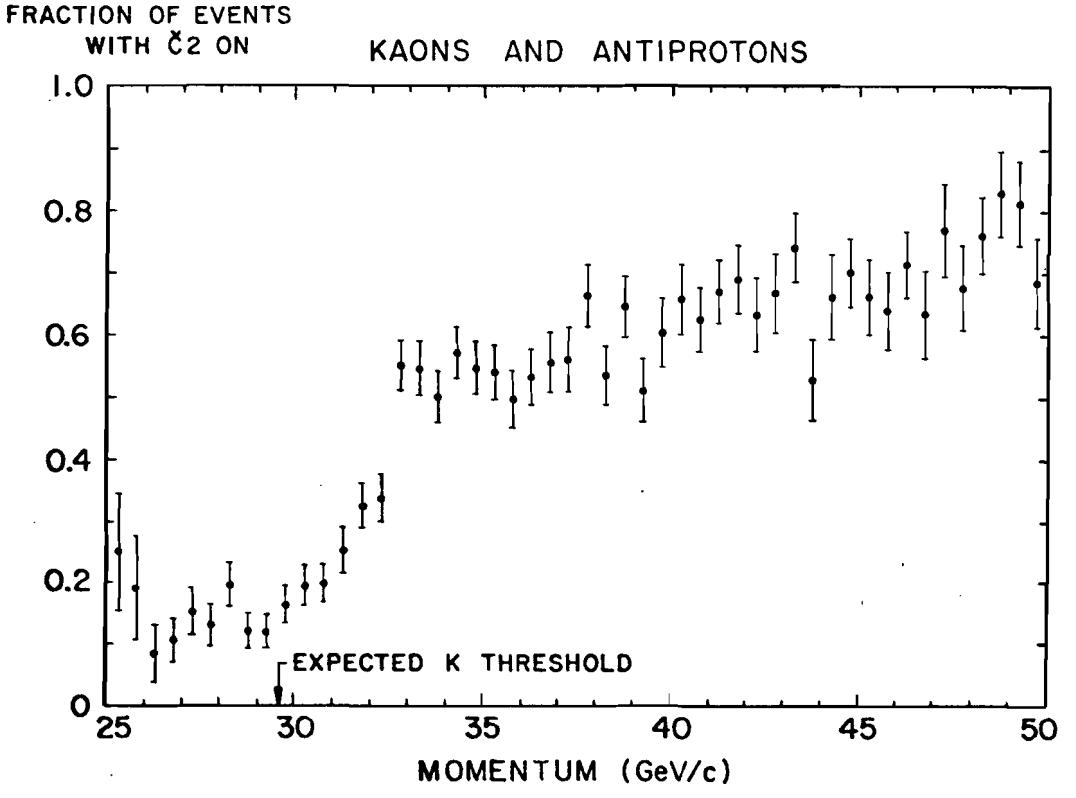
FRACTION OF EVENTS
WITH Č2 ON
KAONS AND ANTIPROTONS
1.0
0.8
0.6
0.4
0.2
0
EXPECTED K THRESHOLD
25
30
35
40
45
50
MOMENTUM (GeV/c)

FIGURE 16

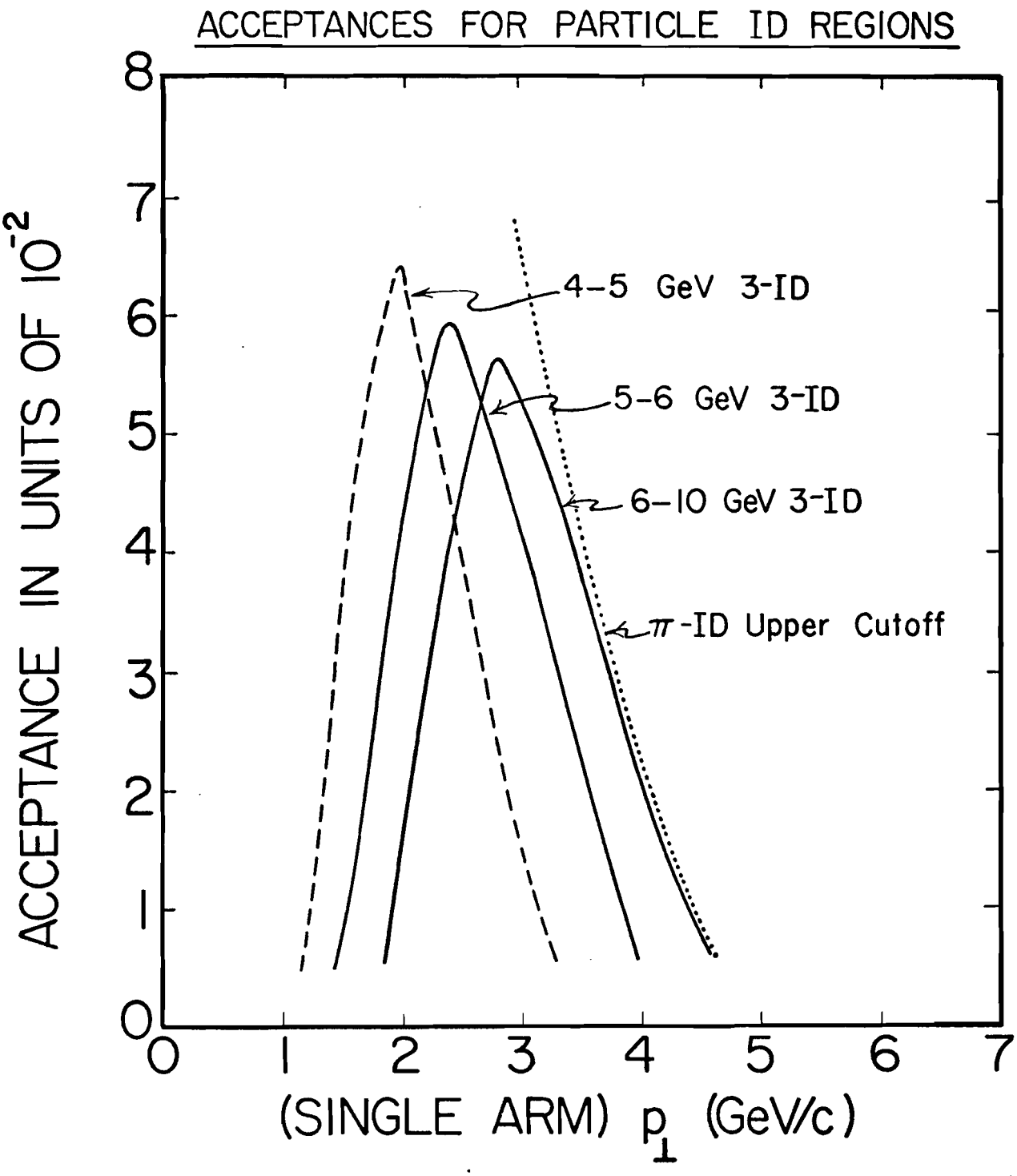
ACCEPTANCES FOR PARTICLE ID REGIONS
ACCEPTANCE IN UNITS OF 10^{-2}
(SINGLE ARM) $p_\perp$ (GeV/c)
4-5 GeV 3-ID
5-6 GeV 3-ID
6-10 GeV 3-ID
π-ID Upper Cutoff
0
1
2
3
4
5
6
7
8

FIGURE 17

Č 2 LIGHT (photoelectrons)

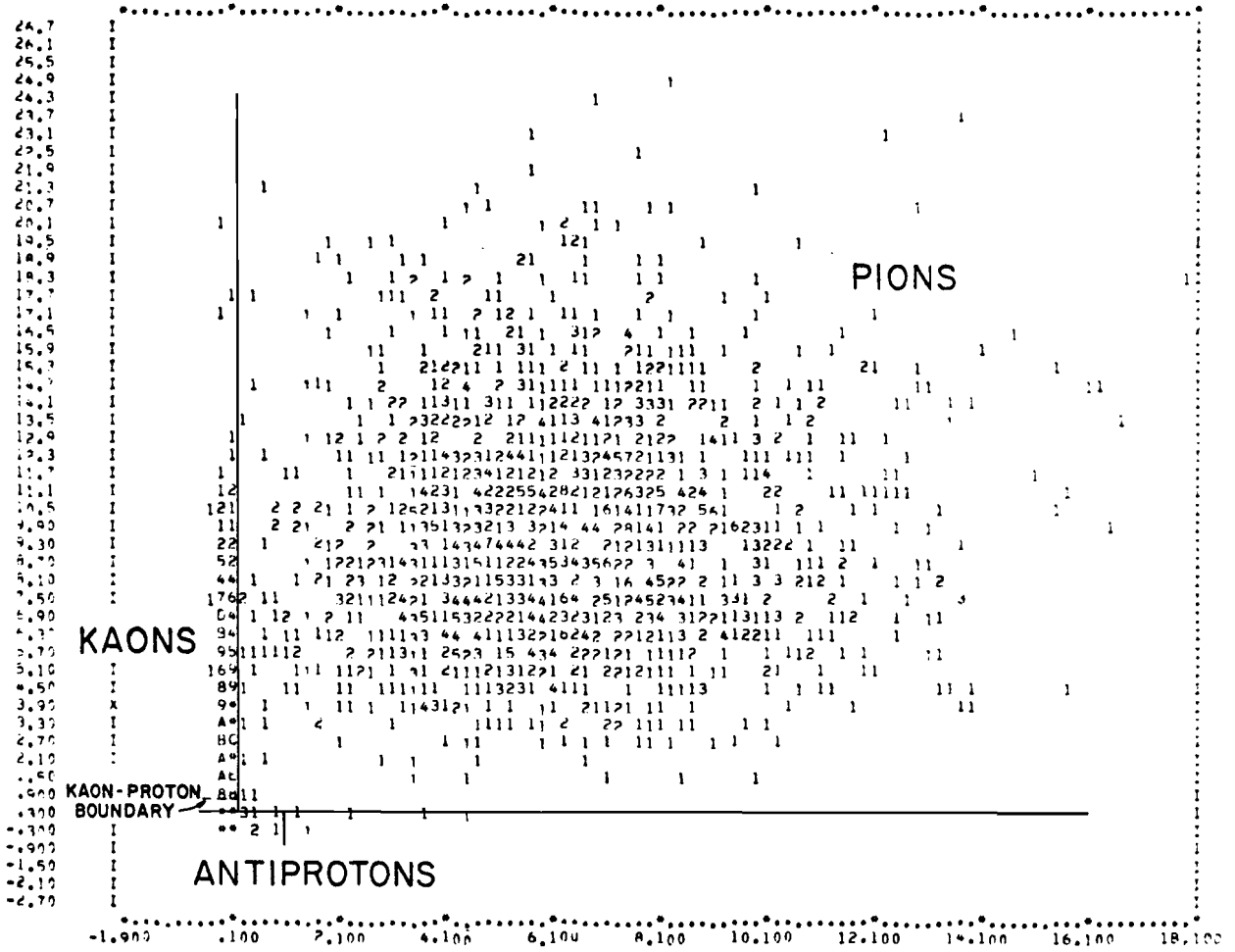

Č 1 LIGHT (photoelectrons)

FIGURE 18

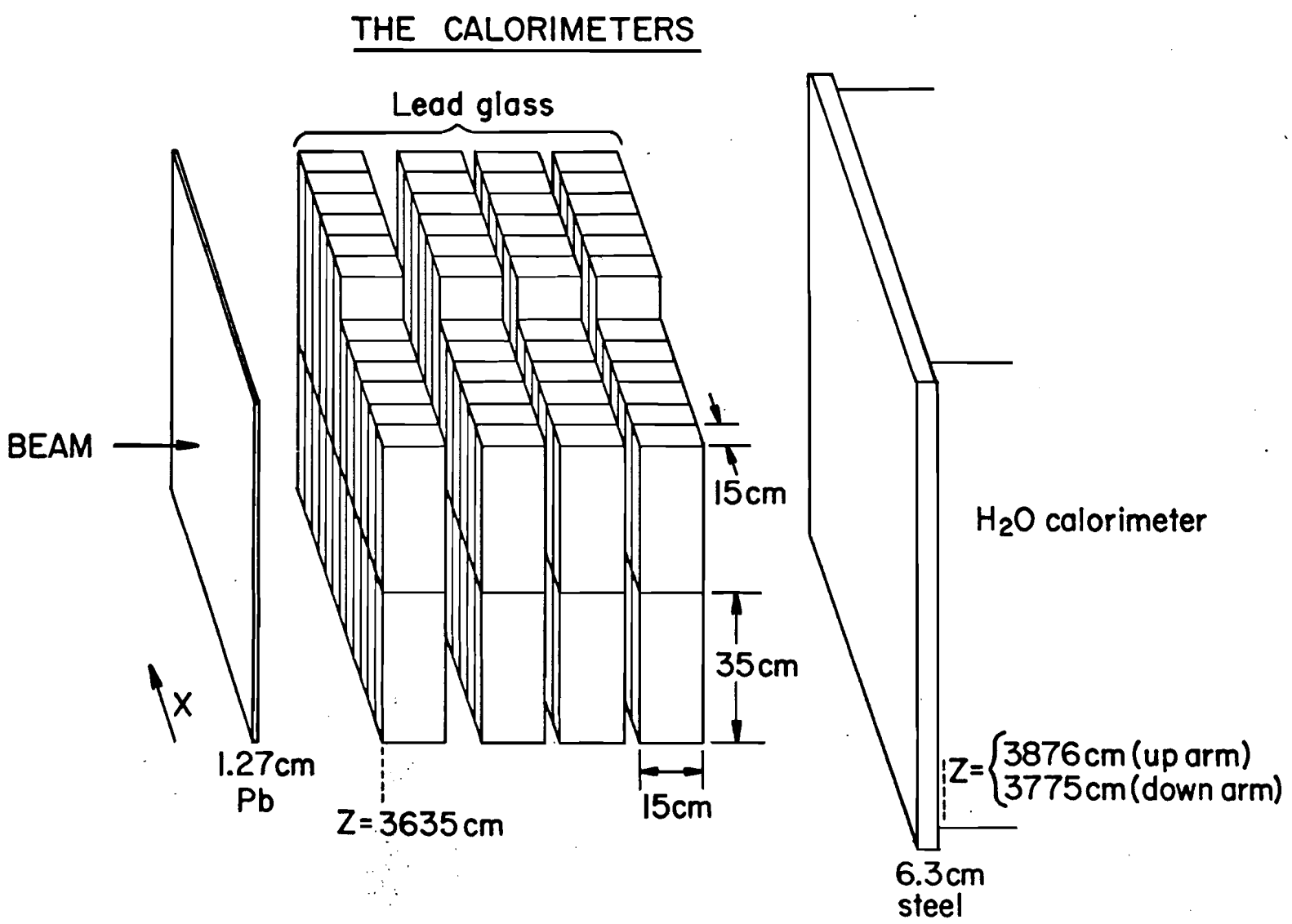
THE CALORIMETERS
Lead glass
BEAM
X
1.27cm
Pb
Z=3635cm
15cm
35cm
15cm
H2O calorimeter
Z={3876cm (up arm)
3775cm (down arm)
6.3cm
steel

FIGURE 19

THE WATER CALORIMETER

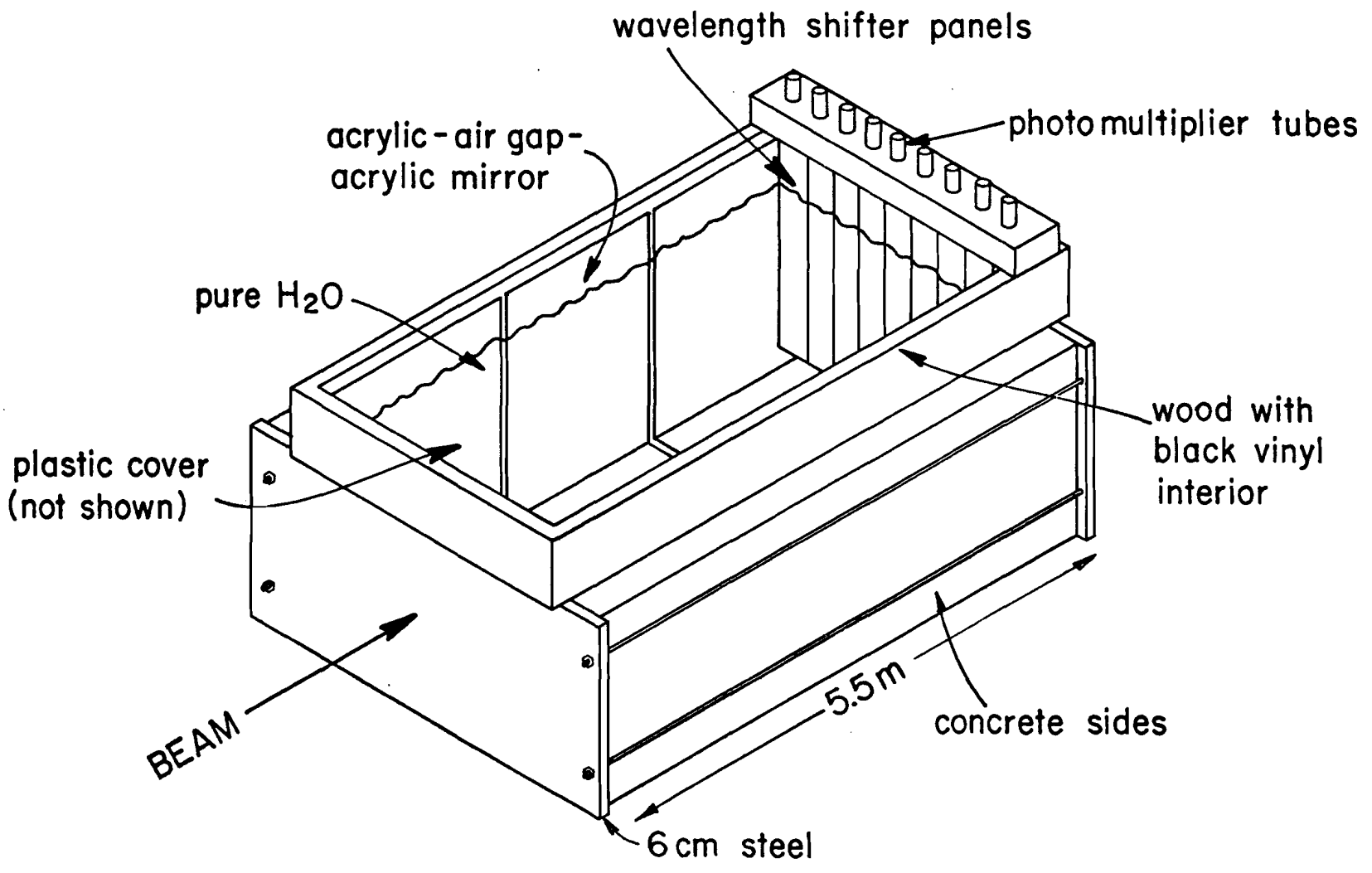

FIGURE 20

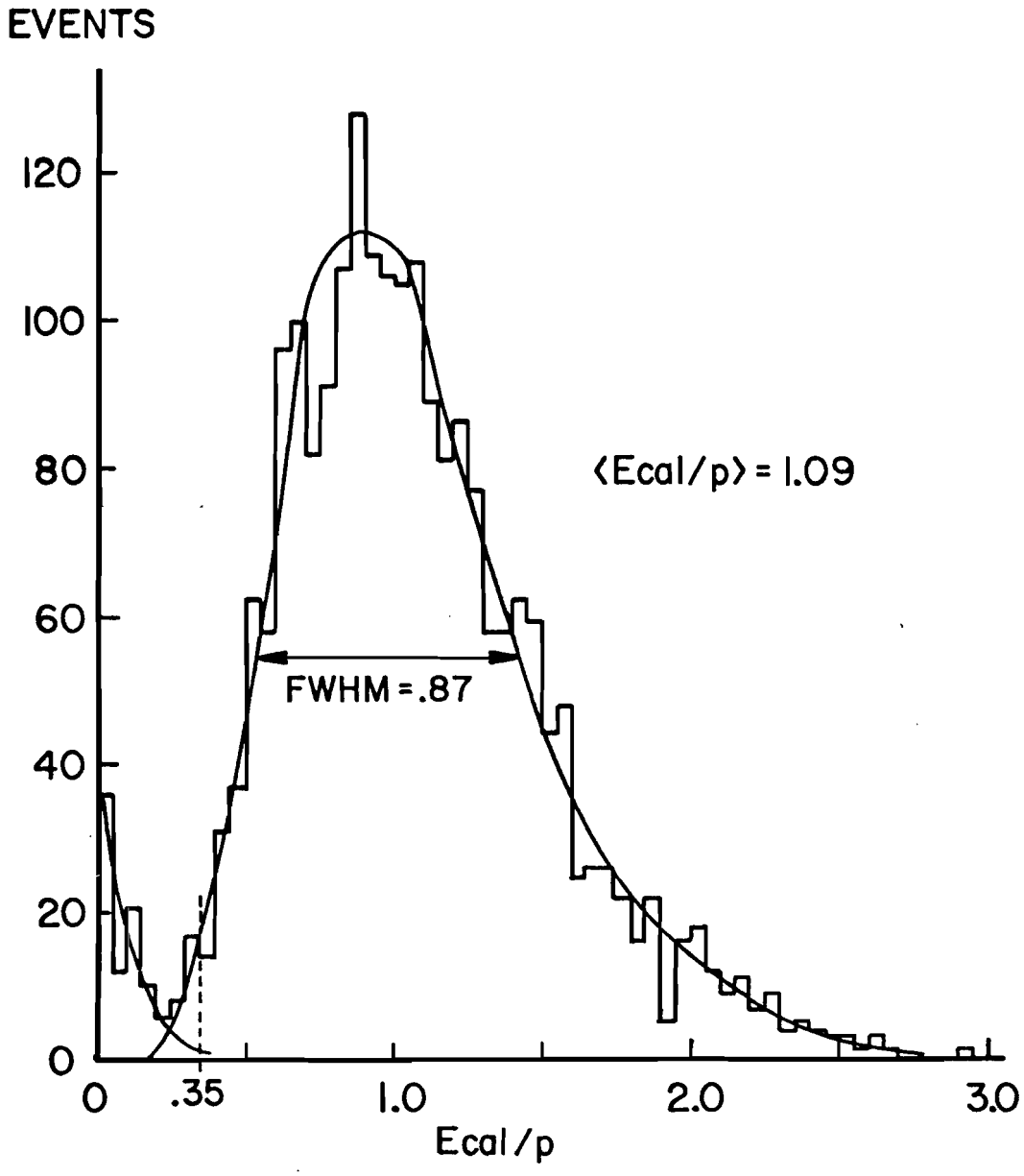

FIGURE 21

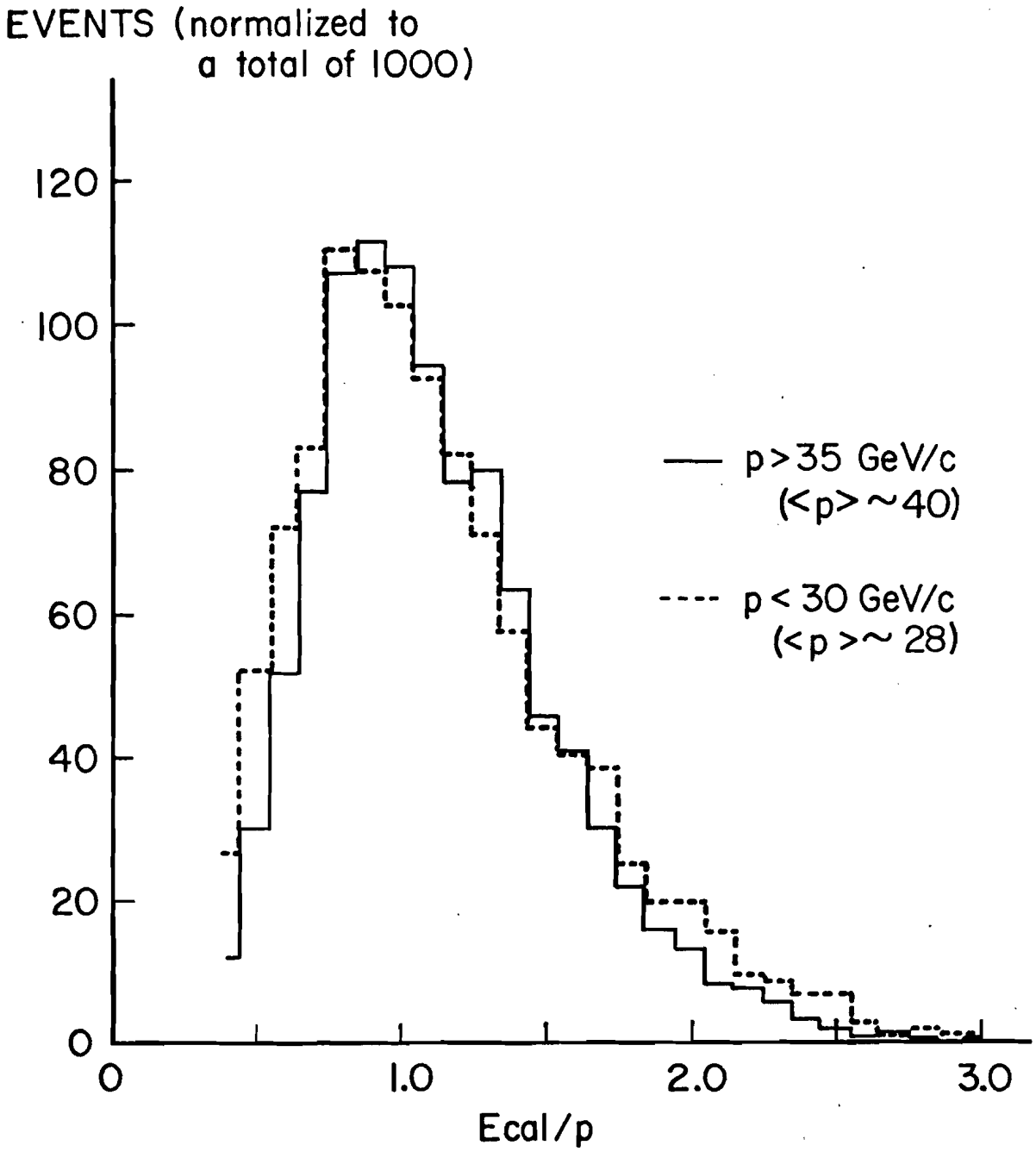
EVENTS (normalized to
a total of 1000)
120
100
80
60
40
20
0
0
1.0
2.0
3.0
Ecal/p
p>35 GeV/c
(<p>~40)
p<30 GeV/c
(<p>~28)

FIGURE 22

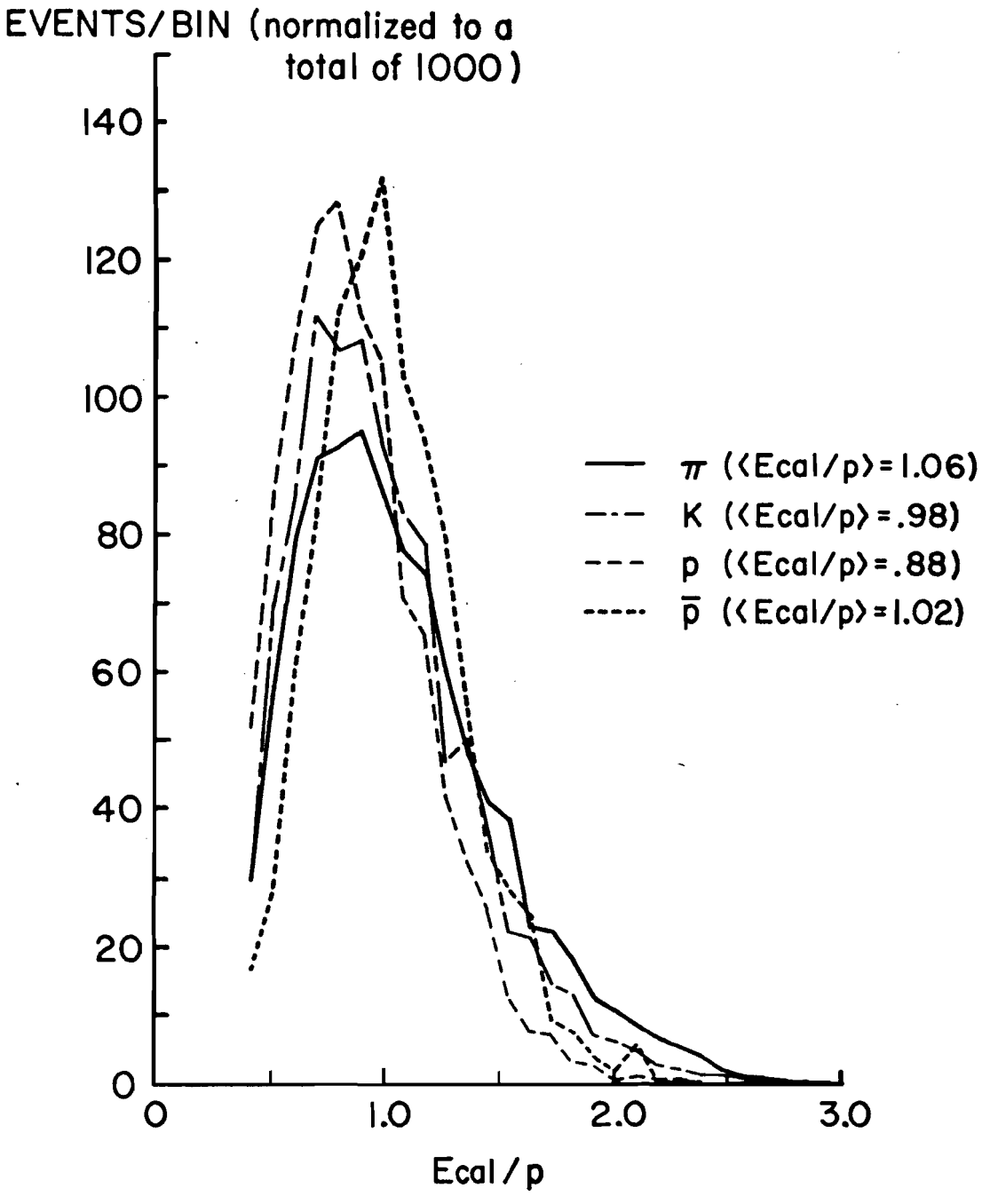
EVENTS/BIN (normalized to a total of 1000)
140
120
100
80
60
40
20
0
0
1.0
2.0
3.0
Ecal/p
π (⟨Ecal/p⟩=1.06)
K (⟨Ecal/p⟩=.98)
p (⟨Ecal/p⟩=.88)
p̄ (⟨Ecal/p⟩=1.02)

FIGURE 23

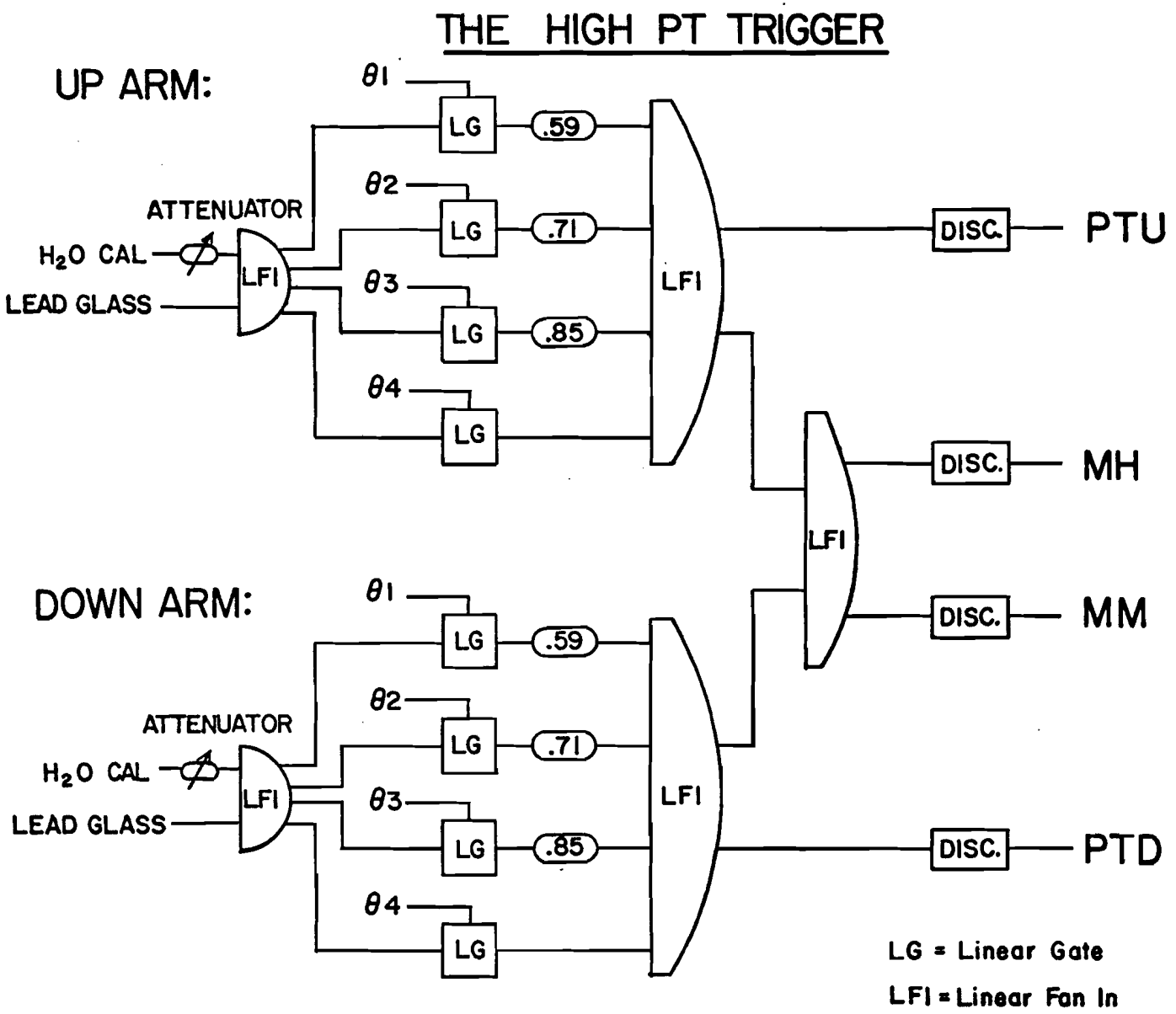
THE HIGH PT TRIGGER
UP ARM:
θ1
LG
.59
θ2
LG
.71
ATTENUATOR
H2O CAL
LFI
LEAD GLASS
θ3
LG
.85
θ4
LG
LFI
DISC.
PTU
LFI
DISC.
MH
DISC.
MM
DOWN ARM:
θ1
LG
.59
θ2
LG
.71
ATTENUATOR
H2O CAL
LFI
LEAD GLASS
θ3
LG
.85
θ4
LG
LFI
DISC.
PTD
LG = Linear Gate
LFI = Linear Fan In

FIGURE 24

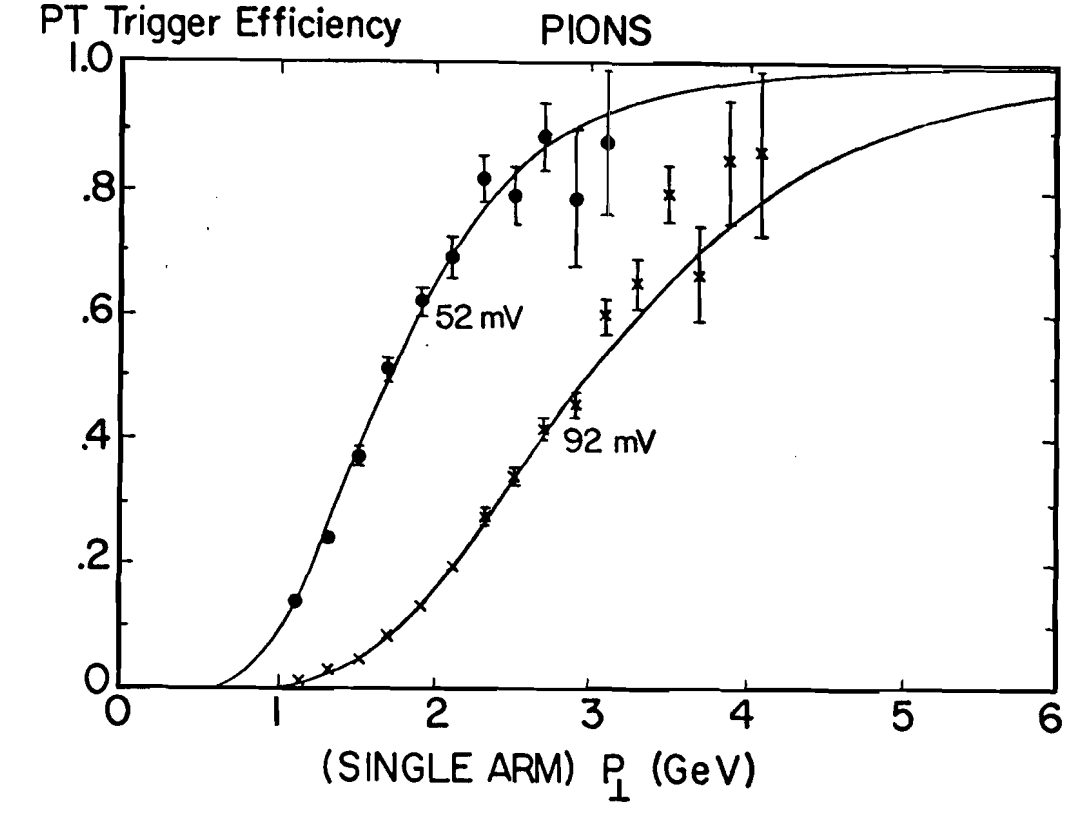
PT Trigger Efficiency
PIONS
1.0
.8
.6
.4
.2
0
52 mV
92 mV
0
1
2
3
4
5
6
(SINGLE ARM) $P_\perp$ (GeV)

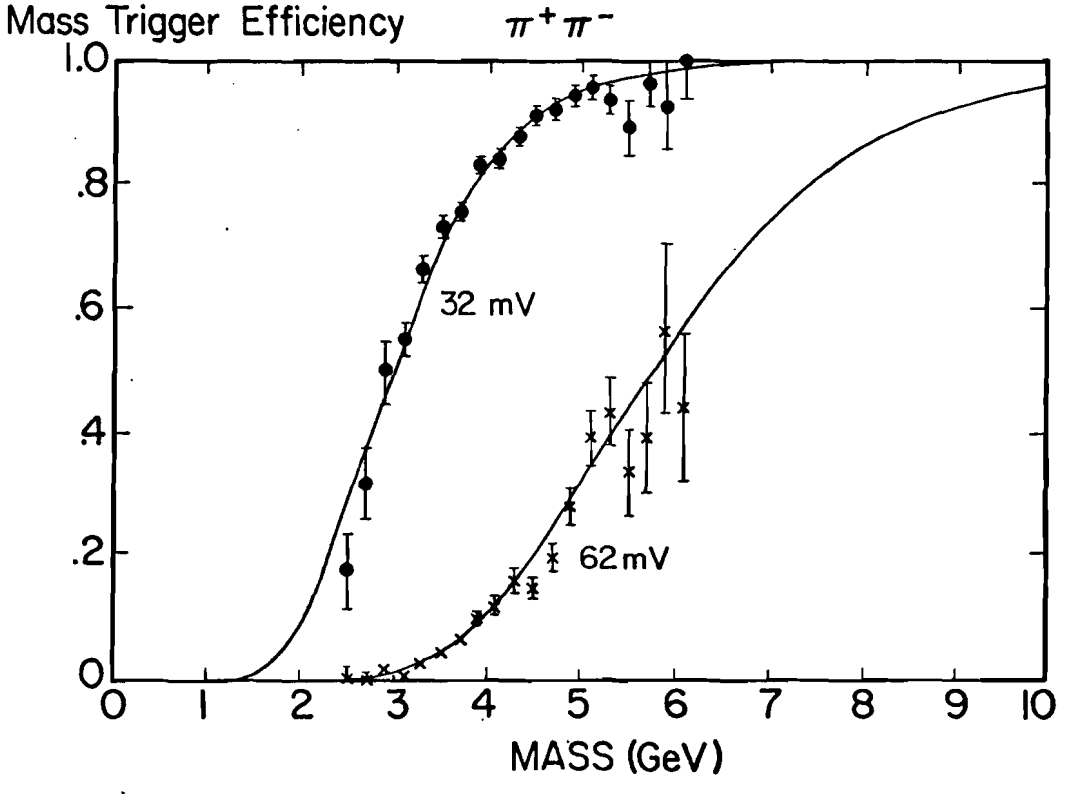
Mass Trigger Efficiency
$\pi^+\pi^-$
1.0
.8
.6
.4
.2
0
32 mV
62mV
0
1
2
3
4
5
6
7
8
9
10
MASS (GeV)

FIGURE 25

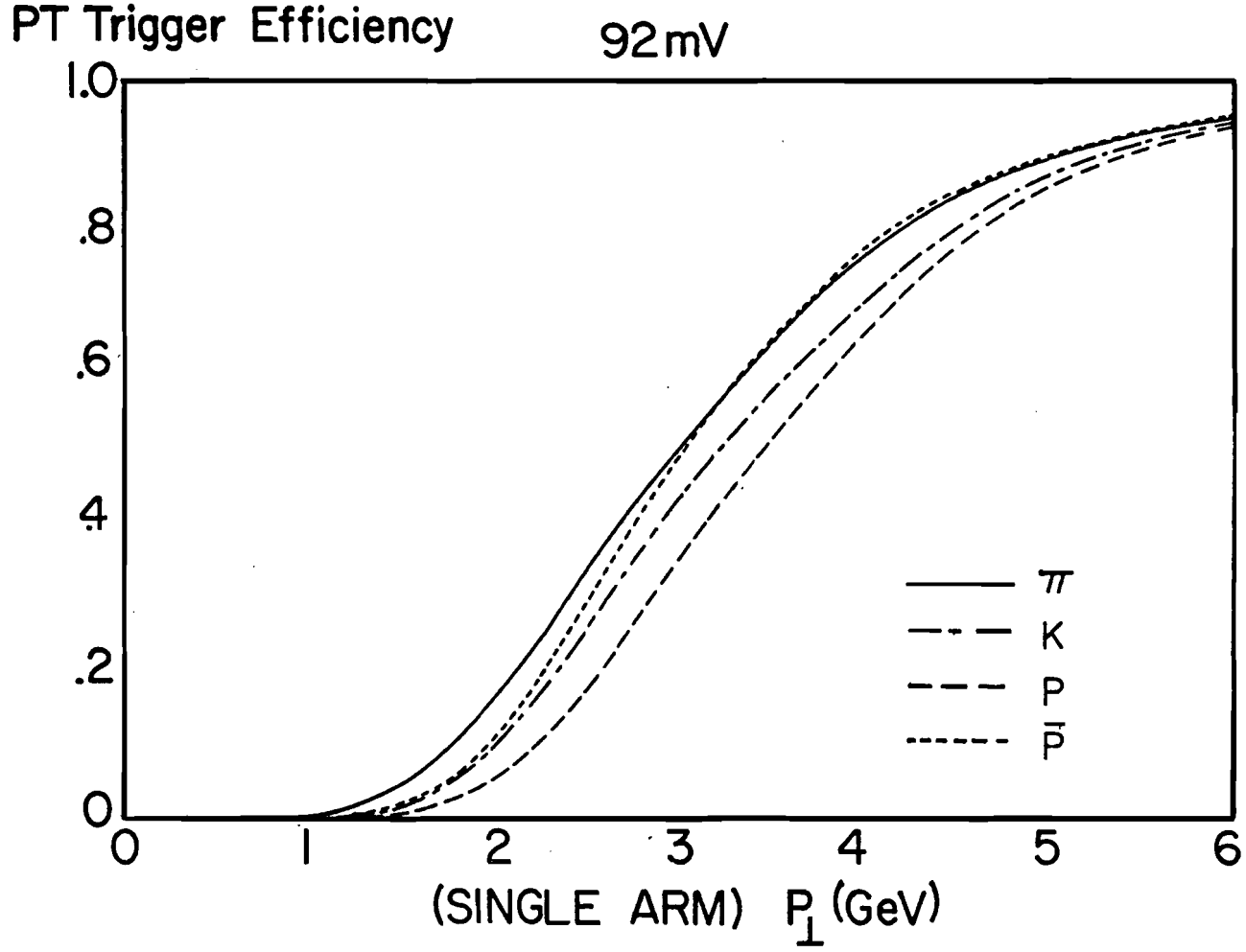
PT Trigger Efficiency
92mV
1.0
.8
.6
.4
.2
0
0
1
2
3
4
5
6
(SINGLE ARM) $P_\perp$ (GeV)
π
K
P
$\bar{P}$

FIGURE 26

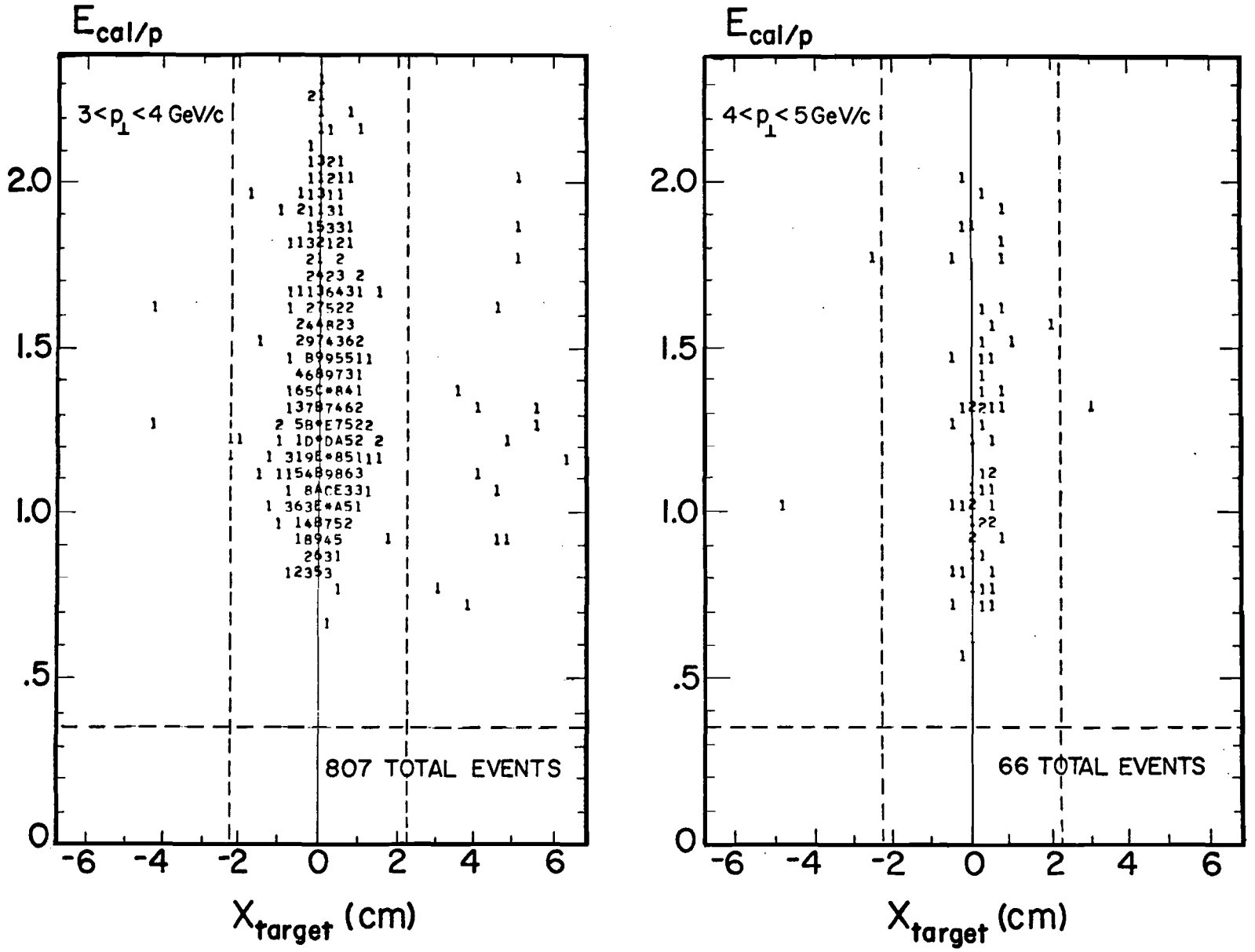
E cal/p
3<p⊥<4 GeV/c
807 TOTAL EVENTS
X target (cm)
E cal/p
4<p⊥<5 GeV/c
66 TOTAL EVENTS
X target (cm)

FIGURE 27

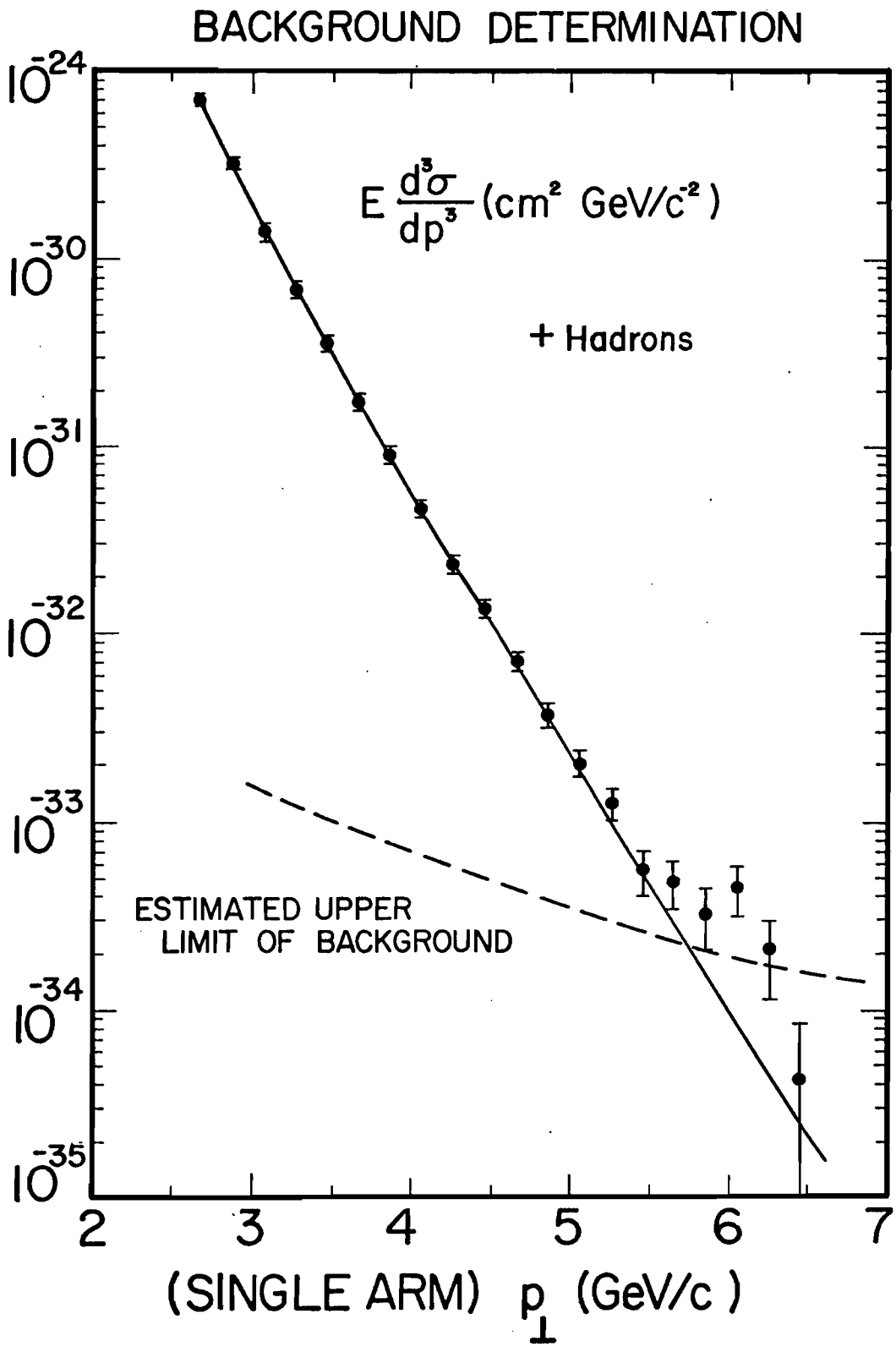
BACKGROUND DETERMINATION
10^{-24}
10^{-30}
10^{-31}
10^{-32}
10^{-33}
10^{-34}
10^{-35}
$E\frac{d^3\sigma}{dp^3}$ (cm² GeV/c⁻²)
+ Hadrons
ESTIMATED UPPER
LIMIT OF BACKGROUND
2
3
4
5
6
7
(SINGLE ARM) $p_\perp$ (GeV/c)

FIGURE 28

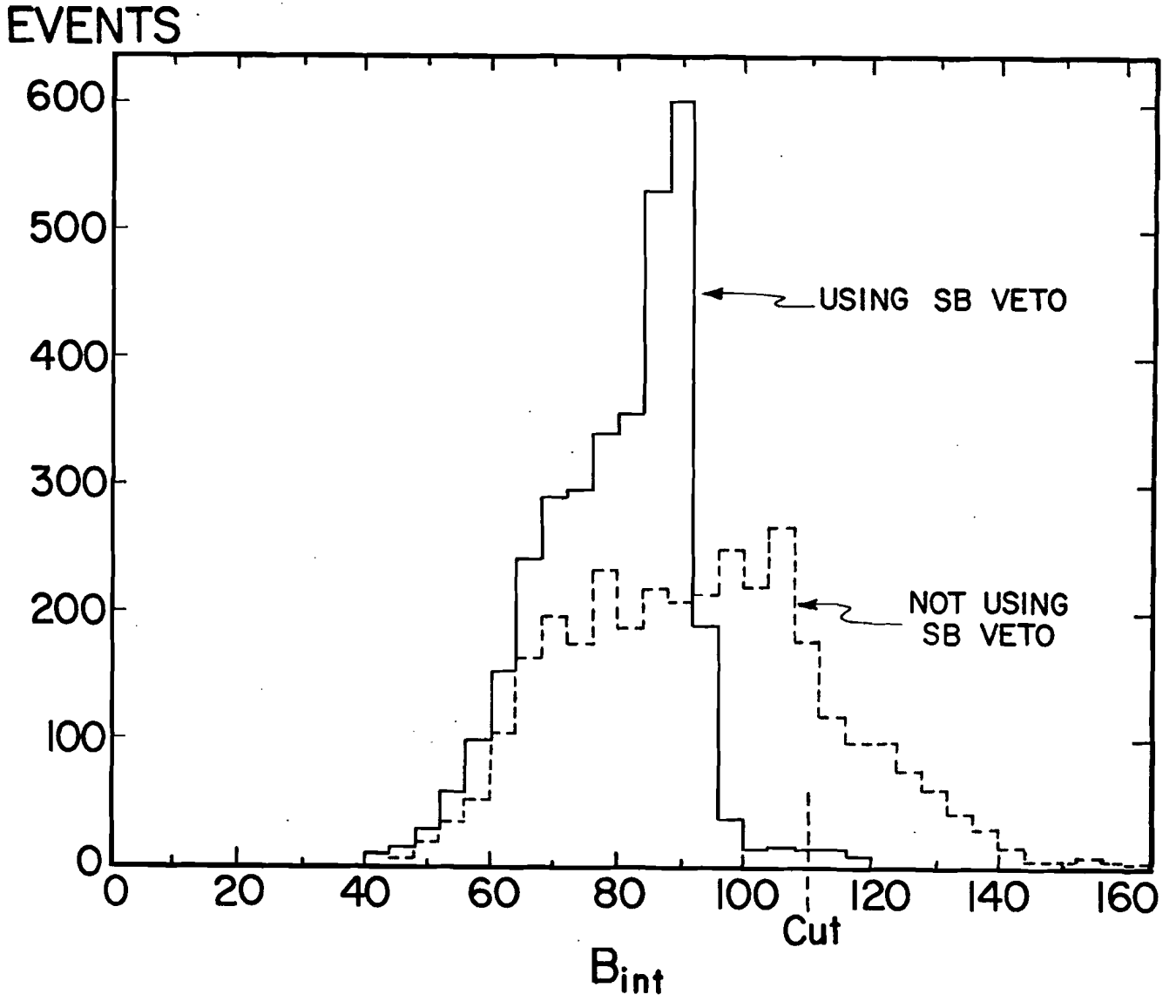
EVENTS
600
500
400
300
200
100
0
0
20
40
60
80
100
120
140
160
Cut
B_{int}
USING SB VETO
NOT USING
SB VETO

FIGURE 29

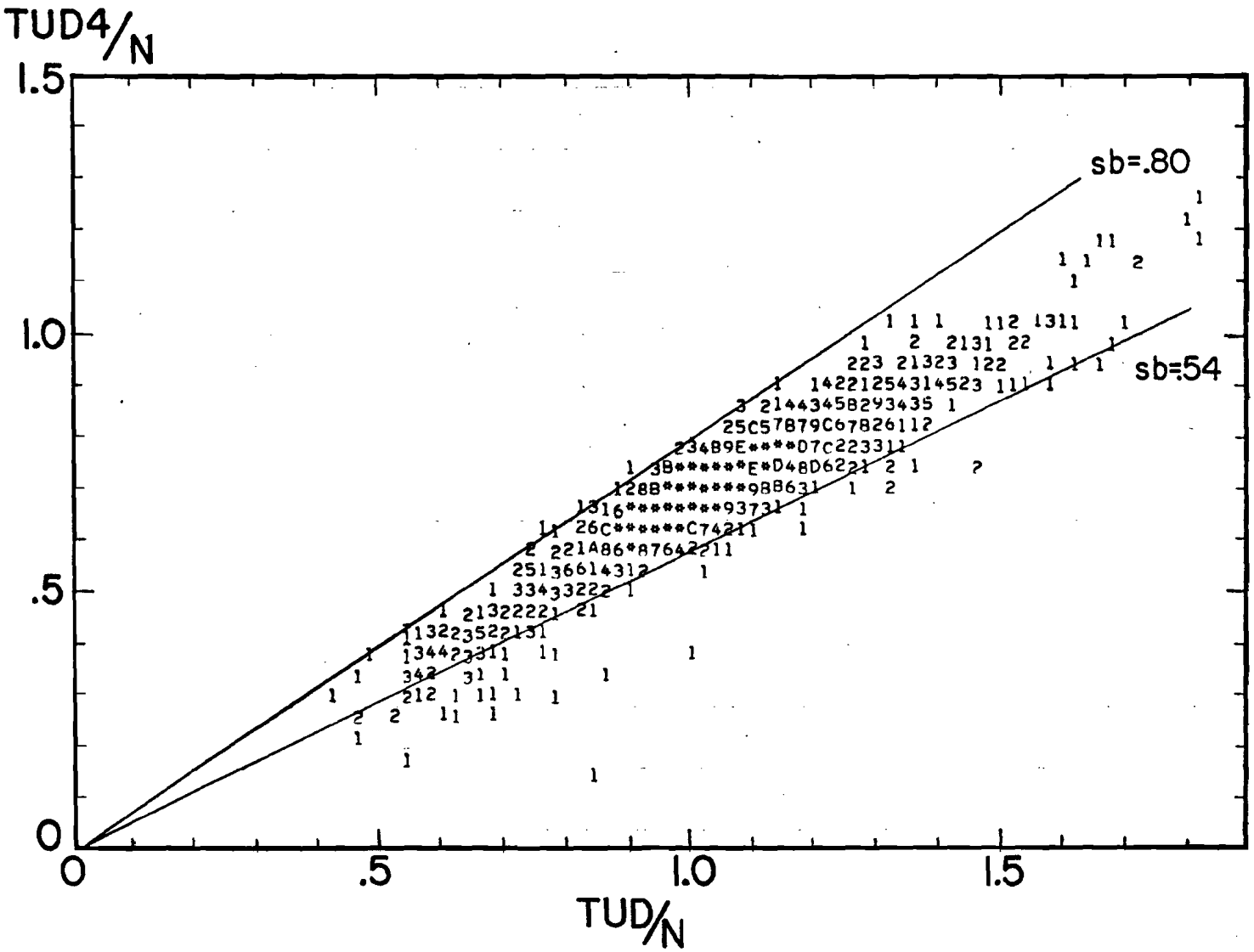

FIGURE 30

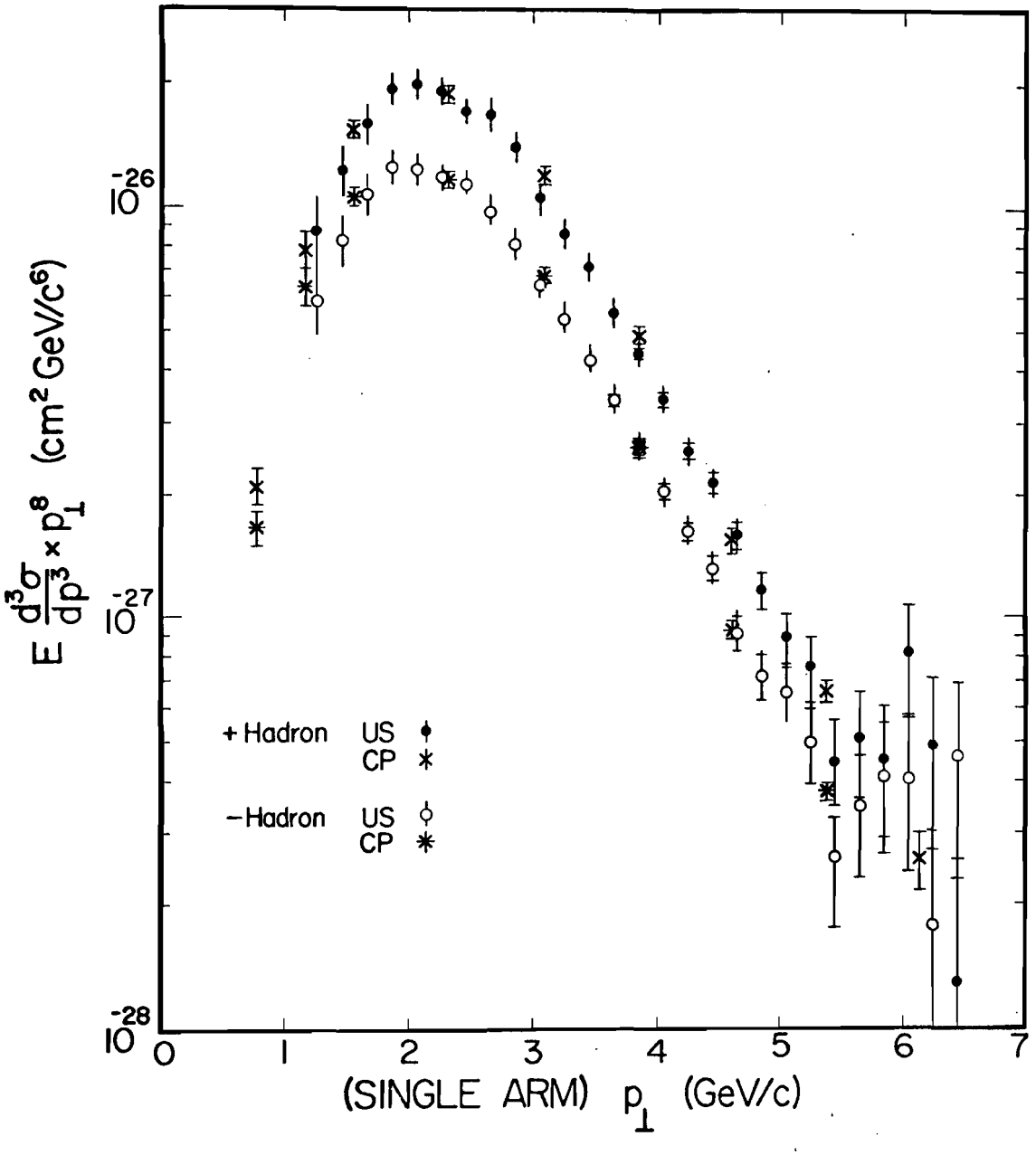
$E\frac{d^3\sigma}{dp^3} \times p_\perp^8$ (cm^2 GeV/c^6)
10^{-26}
10^{-27}
10^{-28}
0
1
2
3
4
5
6
7
(SINGLE ARM) $p_\perp$ (GeV/c)
+ Hadron US
CP
− Hadron US
CP

FIGURE 31

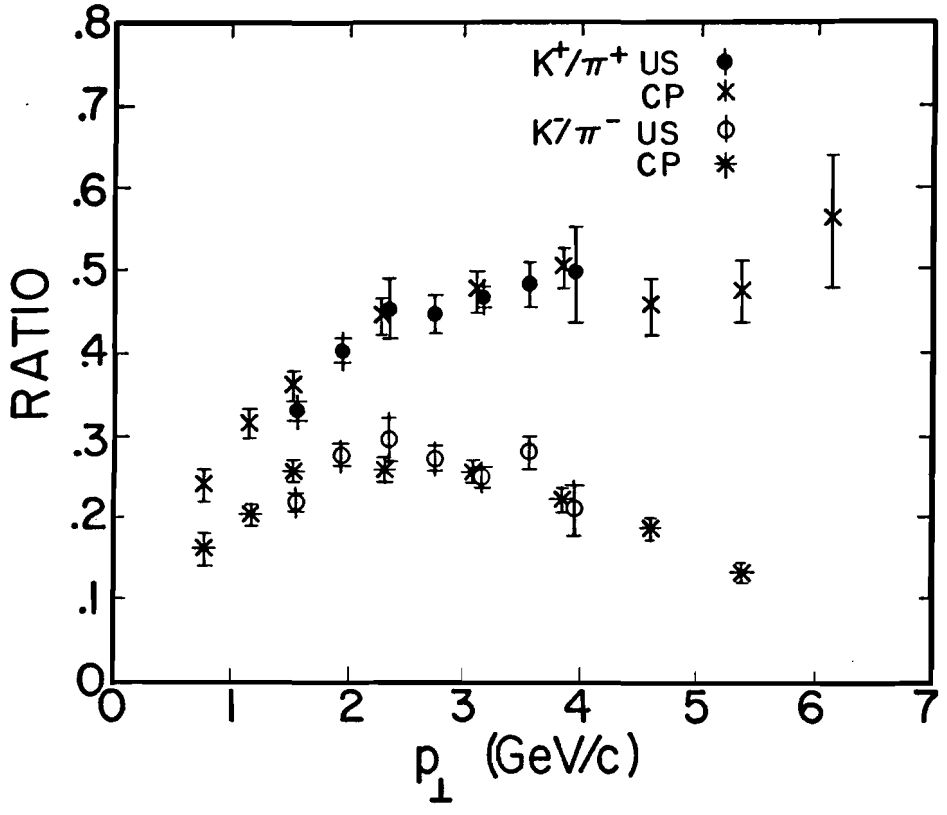
RATIO
K^+/π^+ US
CP
K^-/π^- US
CP
$p_\perp$ (GeV/c)

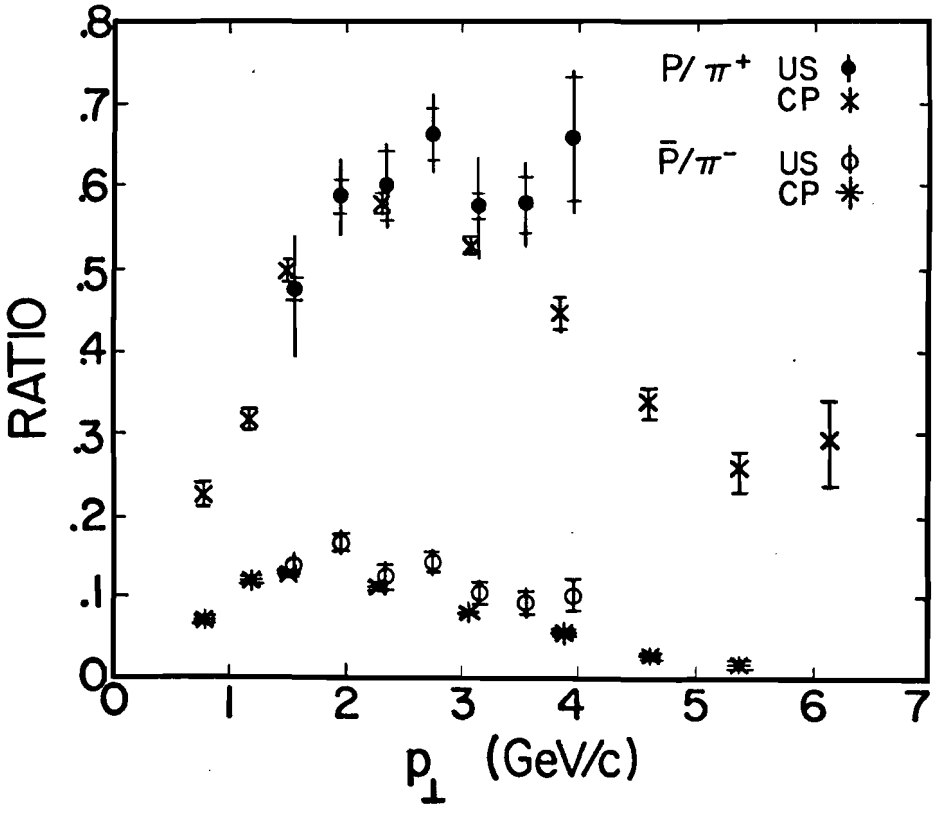
RATIO
P/π^+ US
CP
$\bar{P}/\pi^-$ US
CP
$p_\perp$ (GeV/c)

FIGURE 32

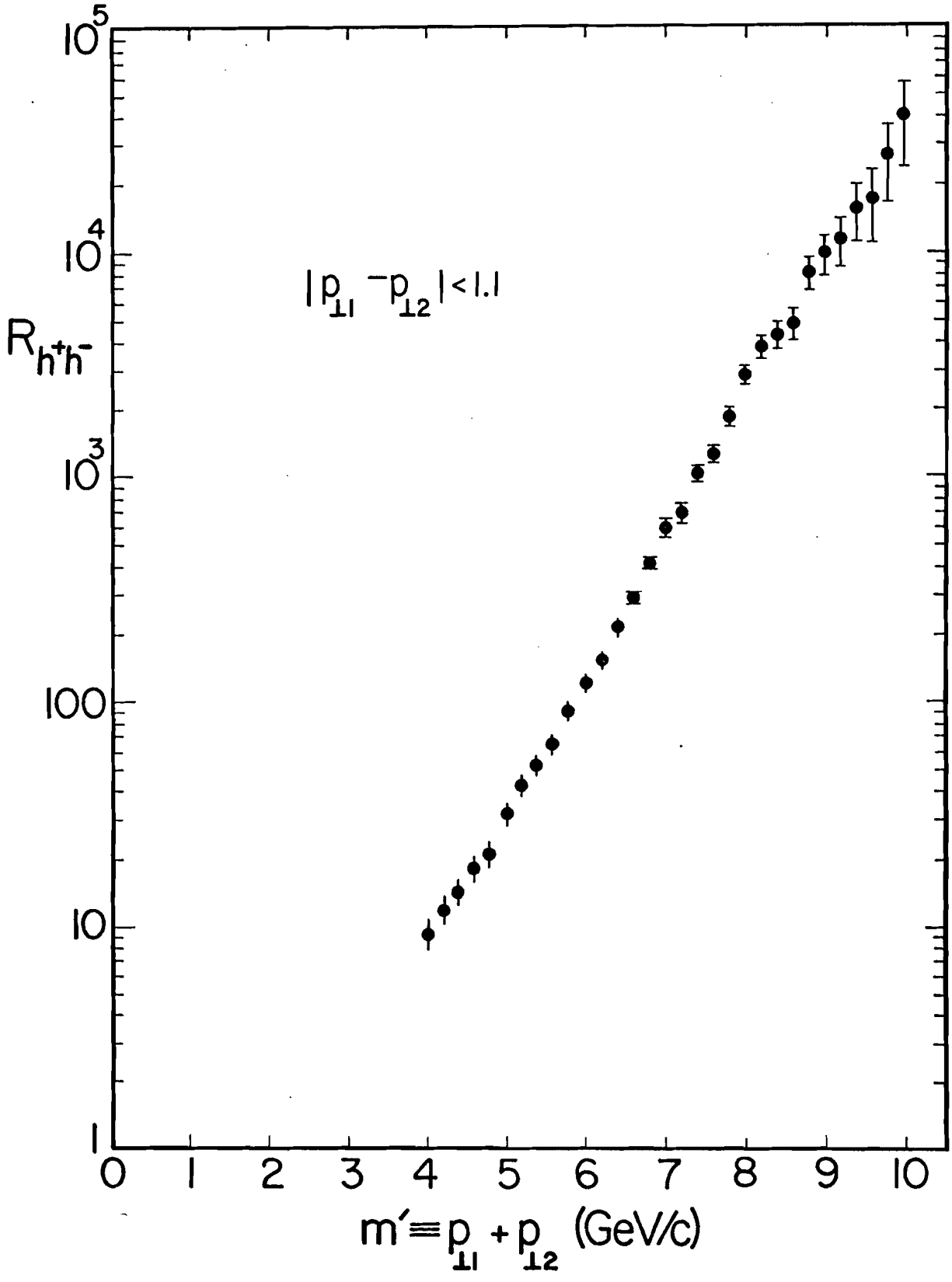
10^5
10^4
10^3
100
10
1
$R_{h^+h^-}$
$|p_{\perp 1} - p_{\perp 2}| < 1.1$
0
1
2
3
4
5
6
7
8
9
10
$m' \equiv p_{\perp 1} + p_{\perp 2}$ (GeV/c)

FIGURE 33

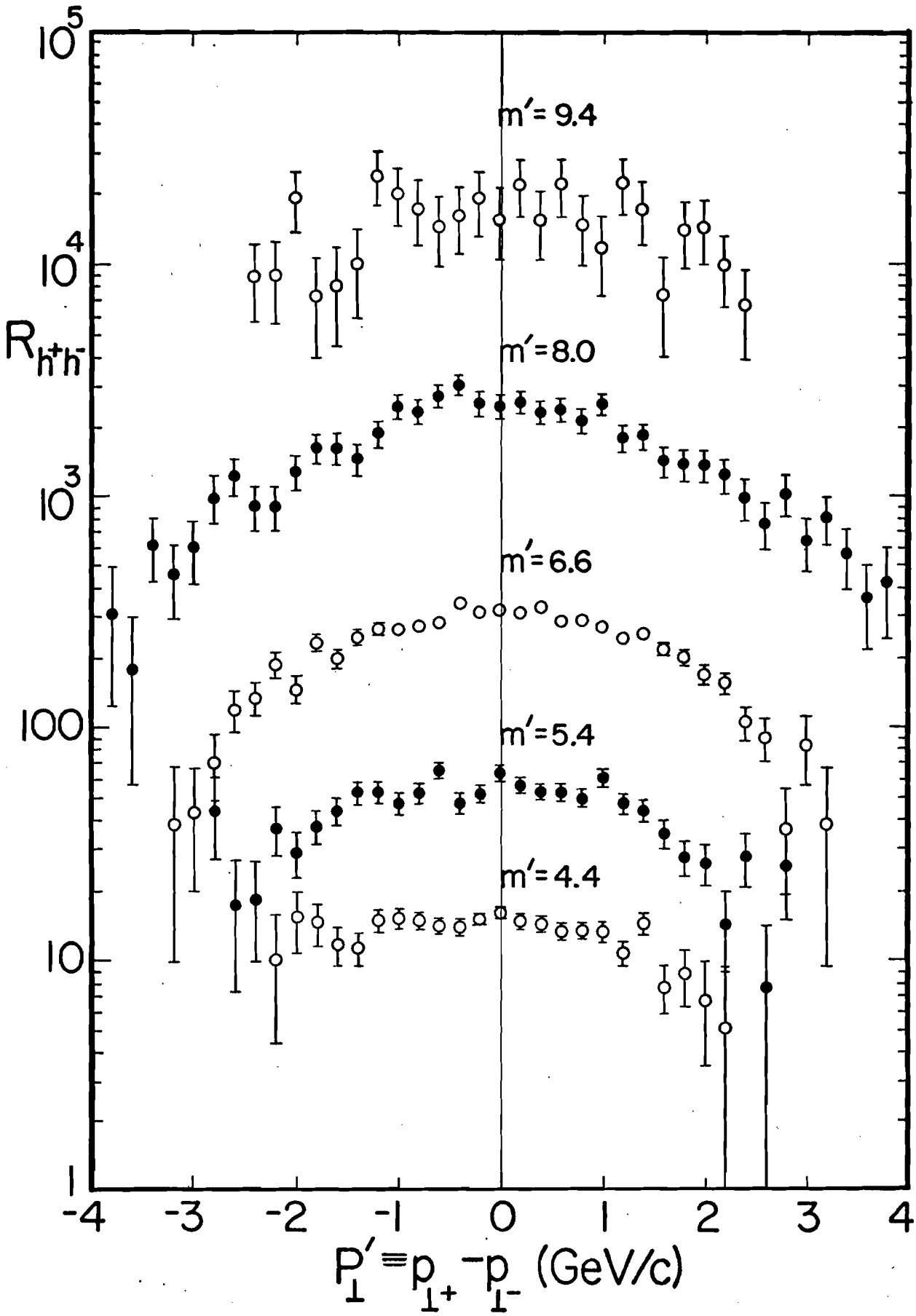
10^5
10^4
10^3
100
10
1
$R_{h^+h^-}$
m′= 9.4
m′=8.0
m′=6.6
m′=5.4
m′=4.4
-4
-3
-2
-1
0
1
2
3
4
$P_\perp' \equiv p_{\perp+} - p_{\perp-}$ (GeV/c)

FIGURE 34

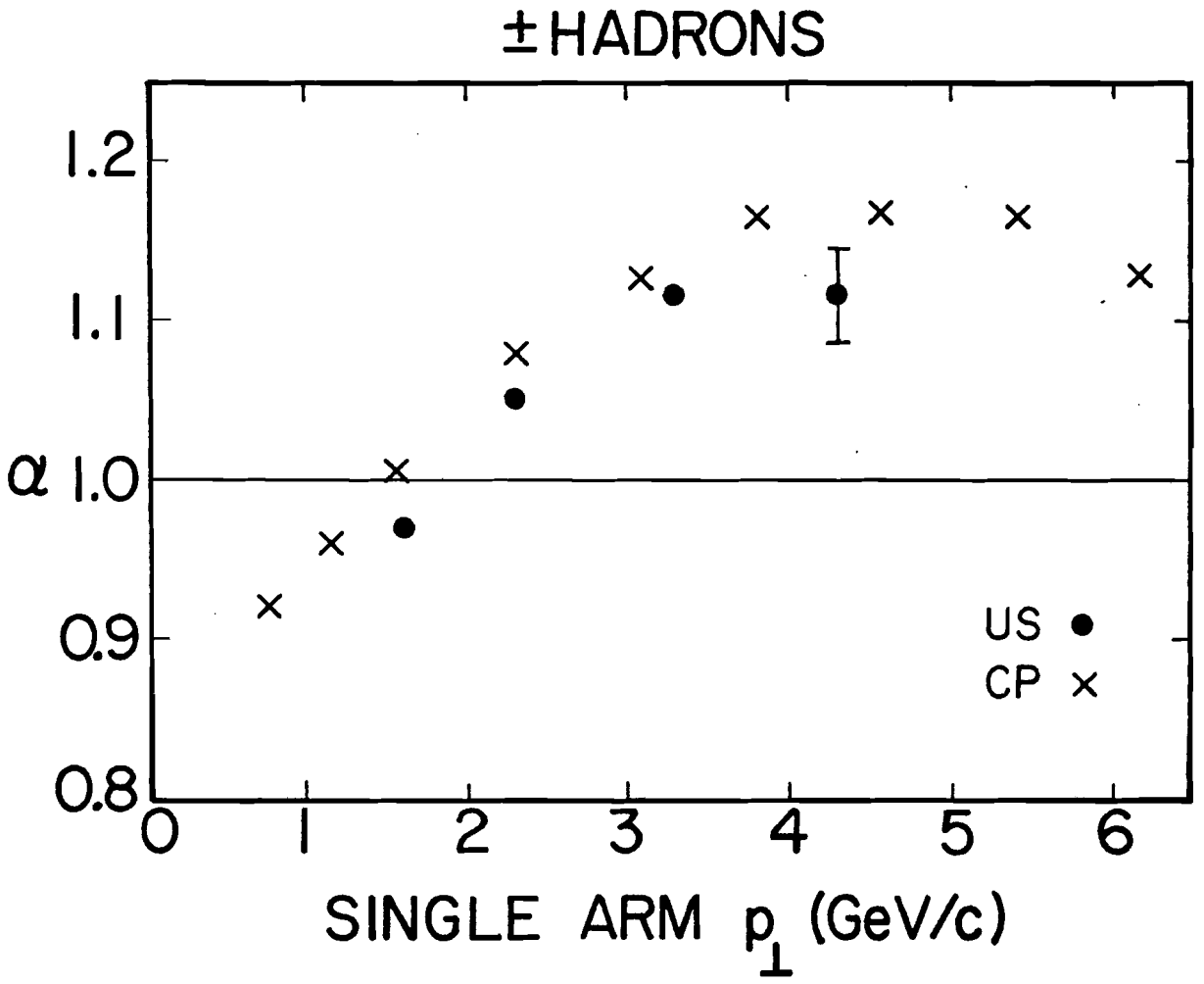

FIGURE 35

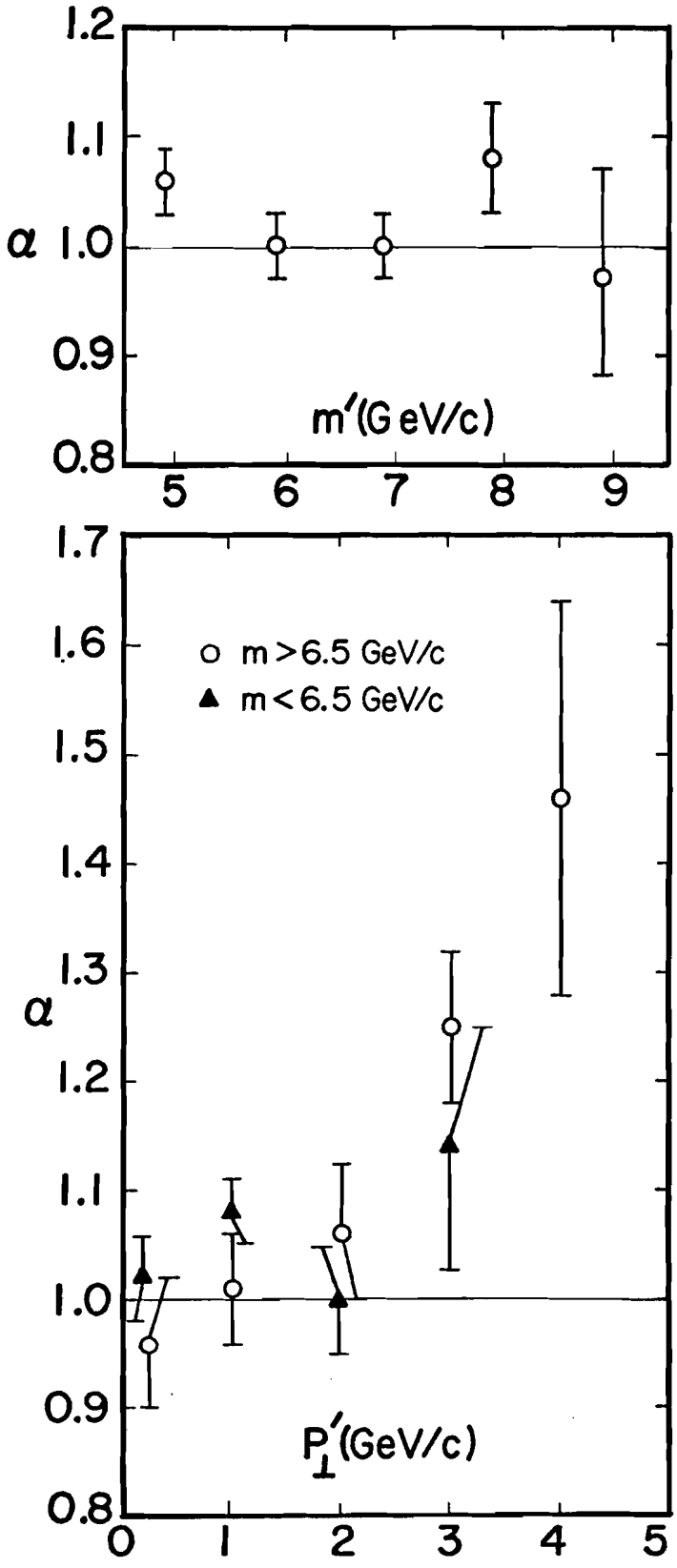
1.2
1.1
α 1.0
0.9
0.8
m′(GeV/c)
5
6
7
8
9
1.7
1.6
1.5
1.4
1.3
α
1.2
1.1
1.0
0.9
0.8
o m>6.5 GeV/c
▲ m<6.5 GeV/c
P⊥′(GeV/c)
0
1
2
3
4
5

FIGURE 36

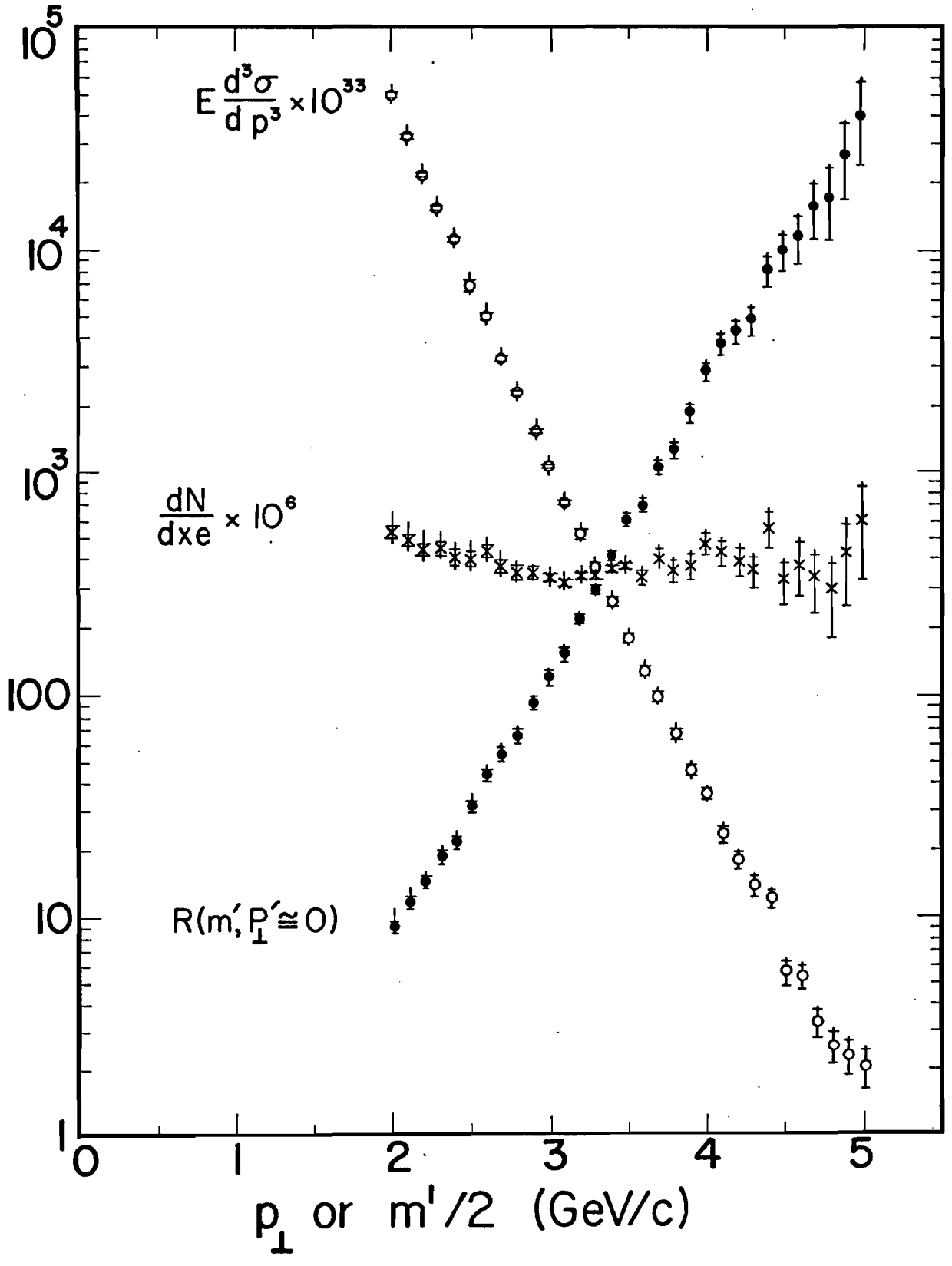
10^5
10^4
10^3
100
10
1
$E\frac{d^3\sigma}{dp^3}\times 10^{33}$
$\frac{dN}{dxe}\times 10^6$
$R(m', P_\perp' \cong 0)$
0
1
2
3
4
5
$p_\perp$ or $m'/2$ (GeV/c)

FIGURE 37

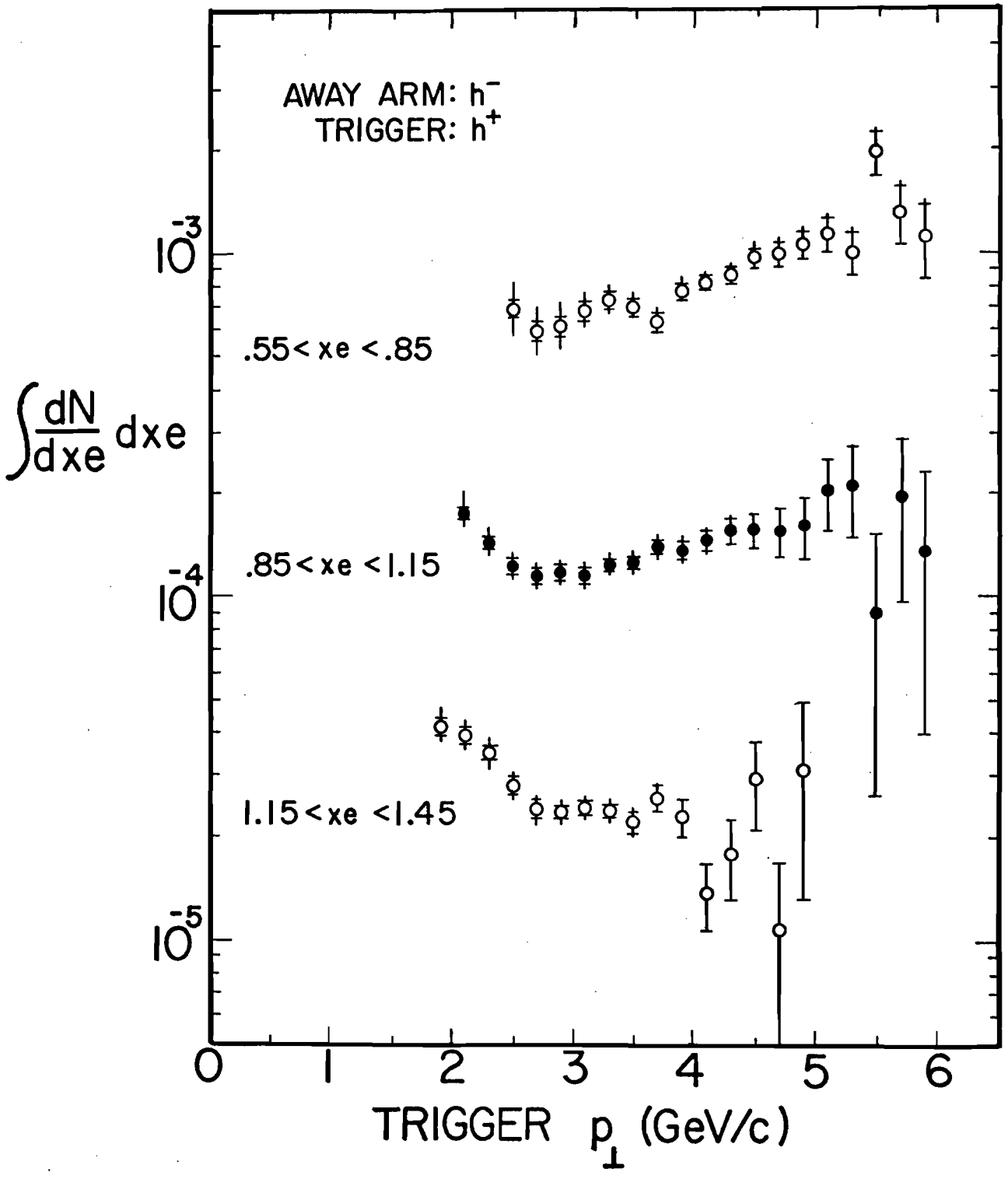
AWAY ARM: h⁻
TRIGGER: h⁺
.55< xe <.85
.85< xe <1.15
1.15< xe <1.45
∫ dN/dxe dxe
10⁻³
10⁻⁴
10⁻⁵
0
1
2
3
4
5
6
TRIGGER p⊥ (GeV/c)

FIGURE 38

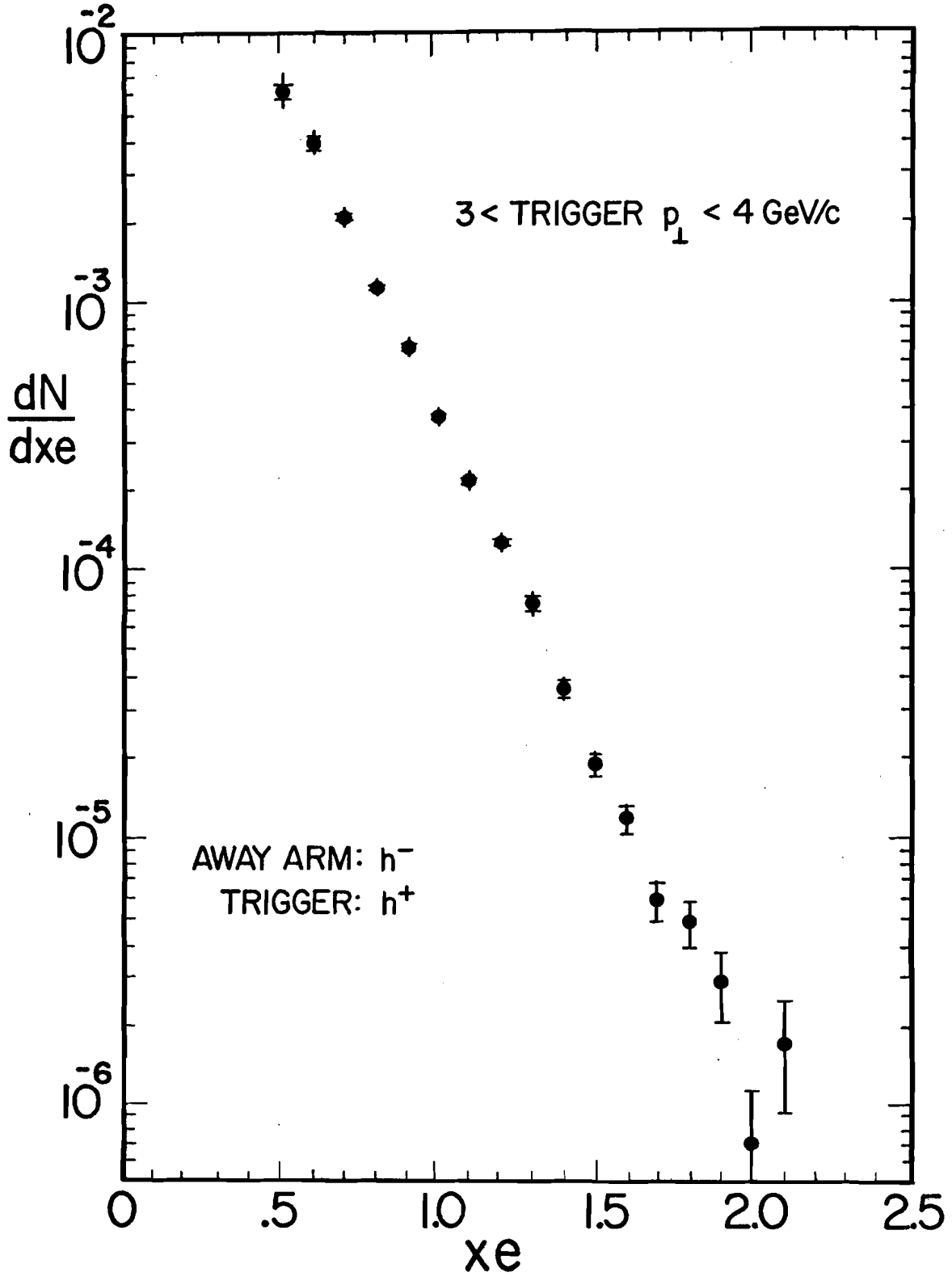
10^{-2}
10^{-3}
10^{-4}
10^{-5}
10^{-6}
dN/dxe
3< TRIGGER $p_\perp$ < 4 GeV/c
AWAY ARM: h^-
TRIGGER: h^+
0
.5
1.0
1.5
2.0
2.5
xe

FIGURE 39

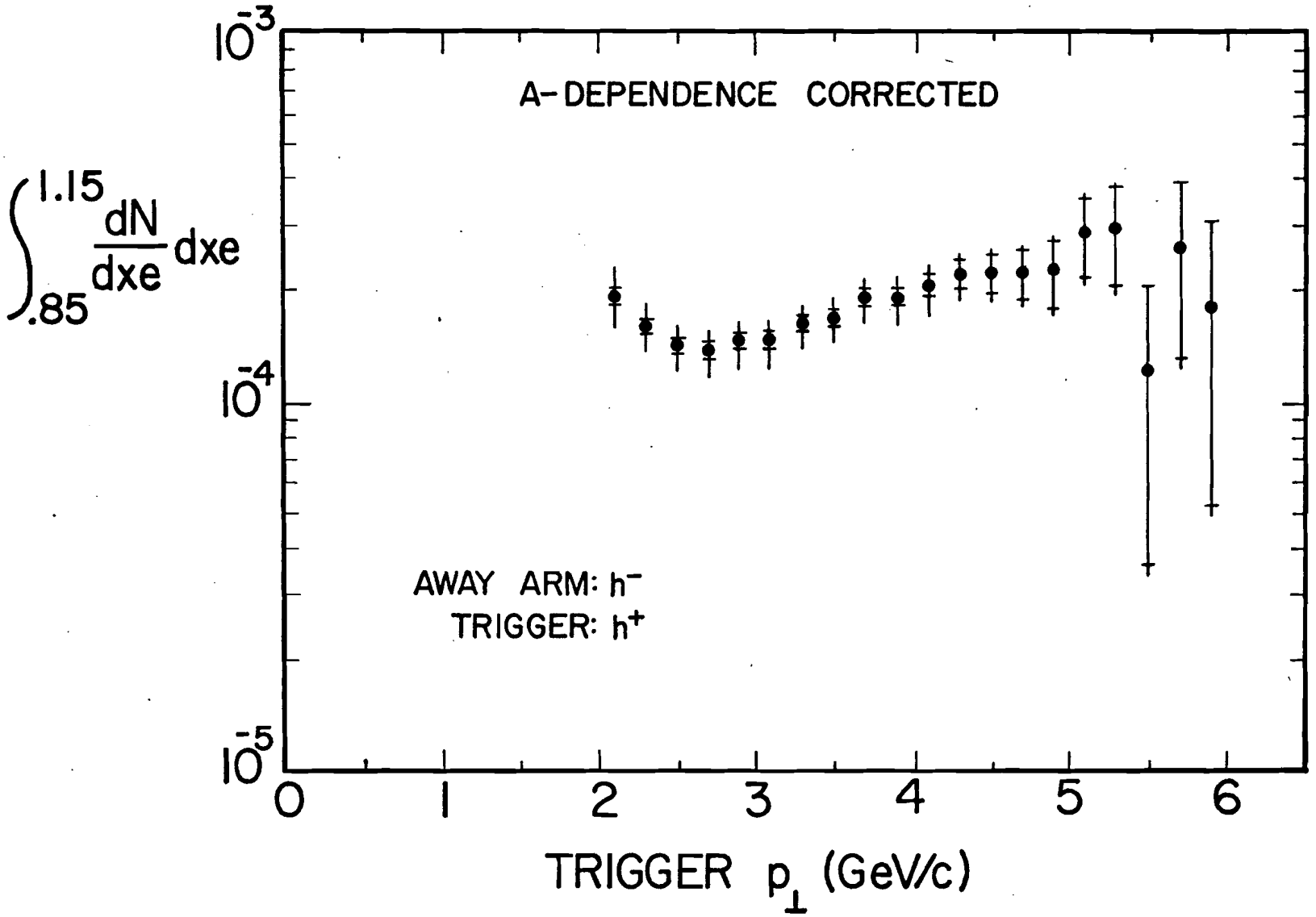
A-DEPENDENCE CORRECTED
$\int_{.85}^{1.15} \frac{dN}{dxe} dxe$
10^{-3}
10^{-4}
10^{-5}
AWAY ARM: h^-
TRIGGER: h^+
0
1
2
3
4
5
6
TRIGGER $p_\perp$ (GeV/c)

FIGURE 40

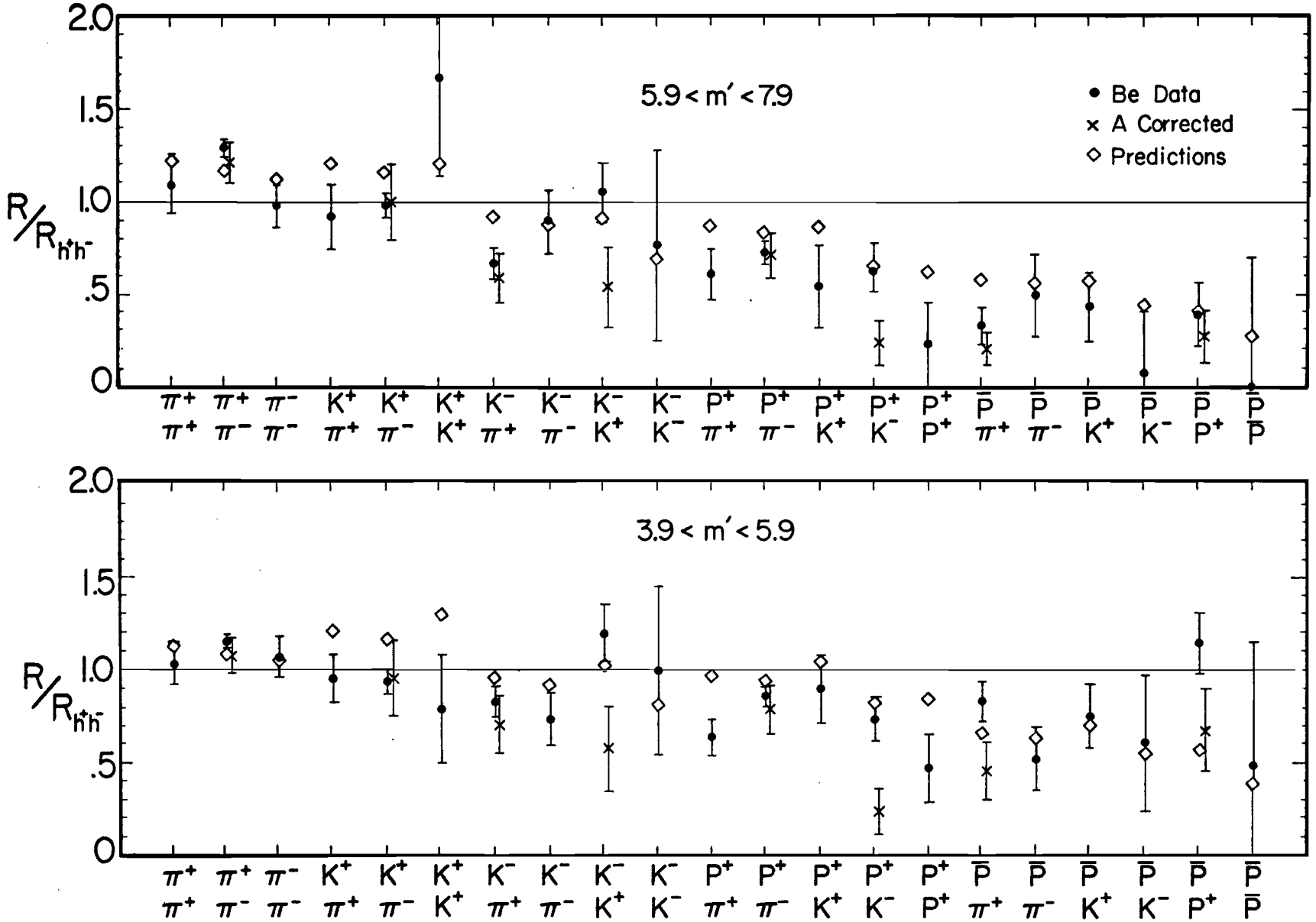
2.0
1.5
1.0
.5
0
R/R_{h⁺h⁻}
5.9 < m′ < 7.9
• Be Data
× A Corrected
◇ Predictions
3.9 < m′ < 5.9
π⁺ π⁺ π⁻ K⁺ K⁺ K⁺ K⁻ K⁻ K⁻ K⁻ P⁺ P⁺ P⁺ P⁺ P⁺ P̄ P̄ P̄ P̄ P̄ P̄
π⁺ π⁻ π⁻ π⁺ π⁻ K⁺ π⁺ π⁻ K⁺ K⁻ π⁺ π⁻ K⁺ K⁻ P⁺ π⁺ π⁻ K⁺ K⁻ P⁺ P̄

FIGURE 41

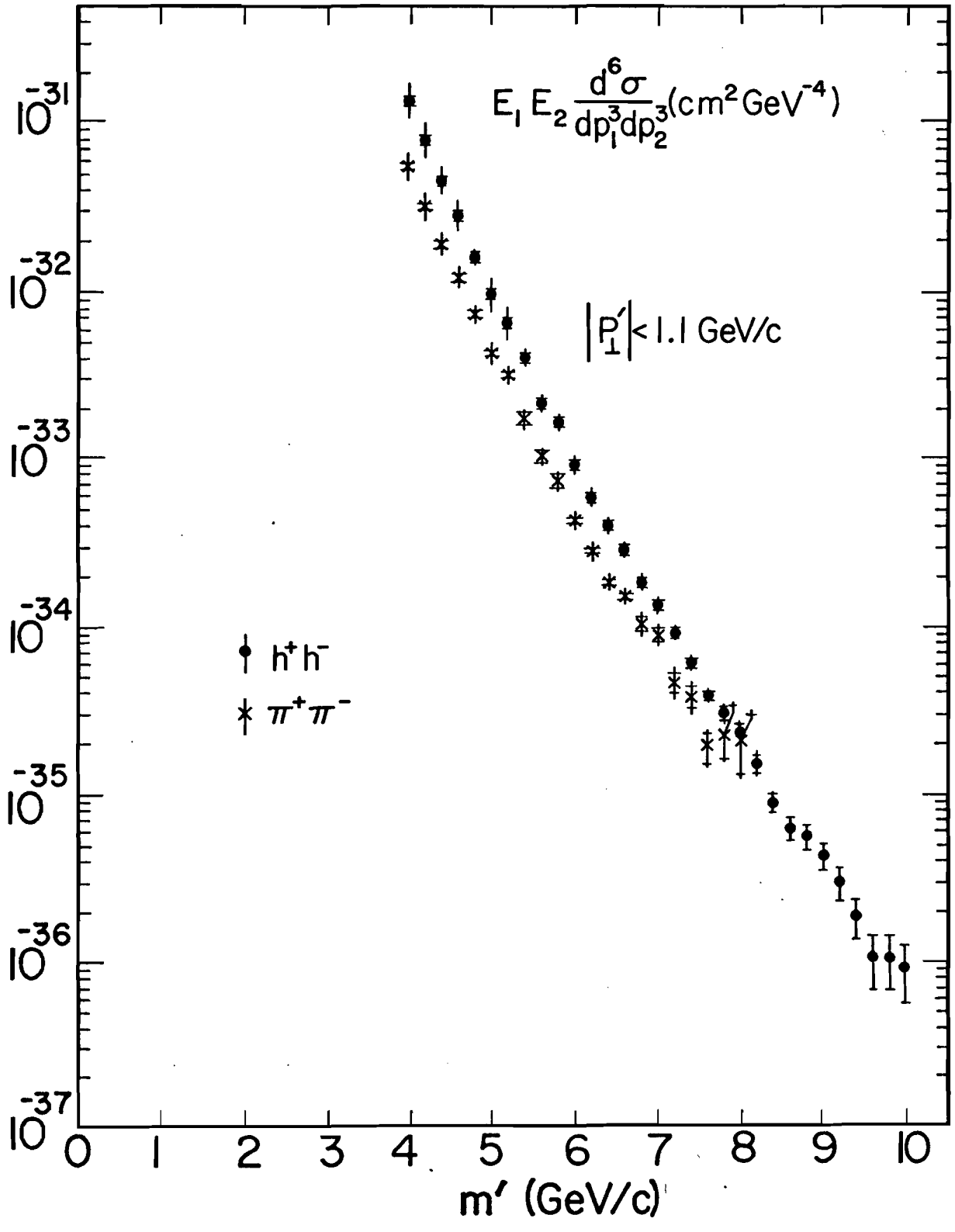
$E_1 E_2 \frac{d^6\sigma}{dp_1^3 dp_2^3} (cm^2 GeV^{-4})$
$|P_\perp'| < 1.1$ GeV/c
h^+h^-
$\pi^+\pi^-$
10^{-31}
10^{-32}
10^{-33}
10^{-34}
10^{-35}
10^{-36}
10^{-37}
0 1 2 3 4 5 6 7 8 9 10
m′ (GeV/c)

FIGURE 42

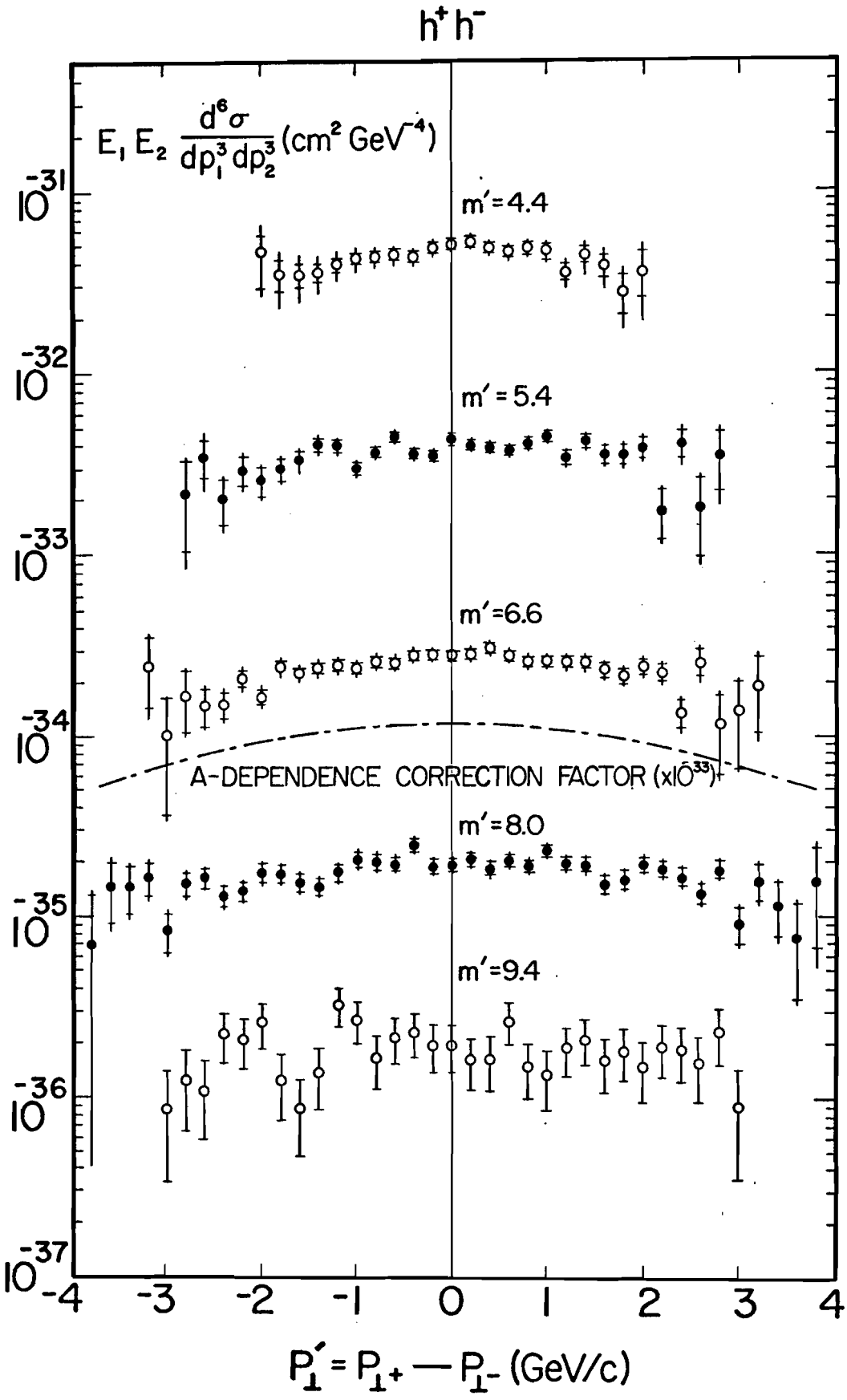
h⁺h⁻
E₁ E₂ d⁶σ/dp₁³dp₂³ (cm² GeV⁻⁴)
m′=4.4
m′=5.4
m′=6.6
A-DEPENDENCE CORRECTION FACTOR (x10⁻³³)
m′=8.0
m′=9.4
10⁻³¹
10⁻³²
10⁻³³
10⁻³⁴
10⁻³⁵
10⁻³⁶
10⁻³⁷
-4
-3
-2
-1
0
1
2
3
4
P′⊥ = P⊥+ — P⊥- (GeV/c)

FIGURE 43

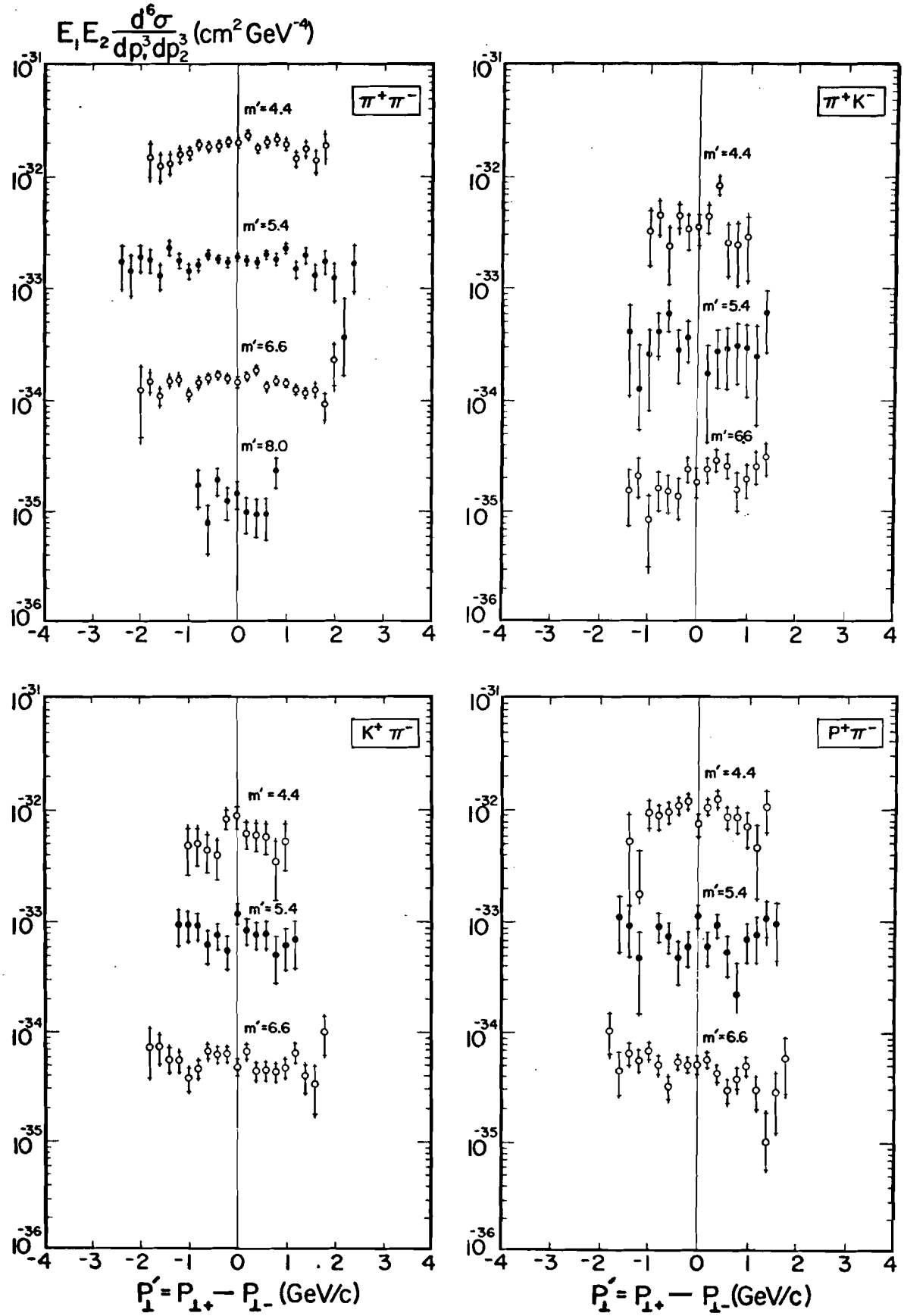
$E_1E_2\frac{d^6\sigma}{dp_1^3dp_2^3}$ (cm^2 GeV^{-4})
$\pi^+\pi^-$
m'=4.4
m'=5.4
m'=6.6
m'=8.0
π^+K^-
m'=4.4
m'=5.4
m'=6.6
$K^+\pi^-$
m'=4.4
m'=5.4
m'=6.6
$P^+\pi^-$
m'=4.4
m'=5.4
m'=6.6
$P_\perp' = P_{\perp+} - P_{\perp-}$ (GeV/c)
$P_\perp' = P_{\perp+} - P_{\perp-}$ (GeV/c)

FIGURE 44

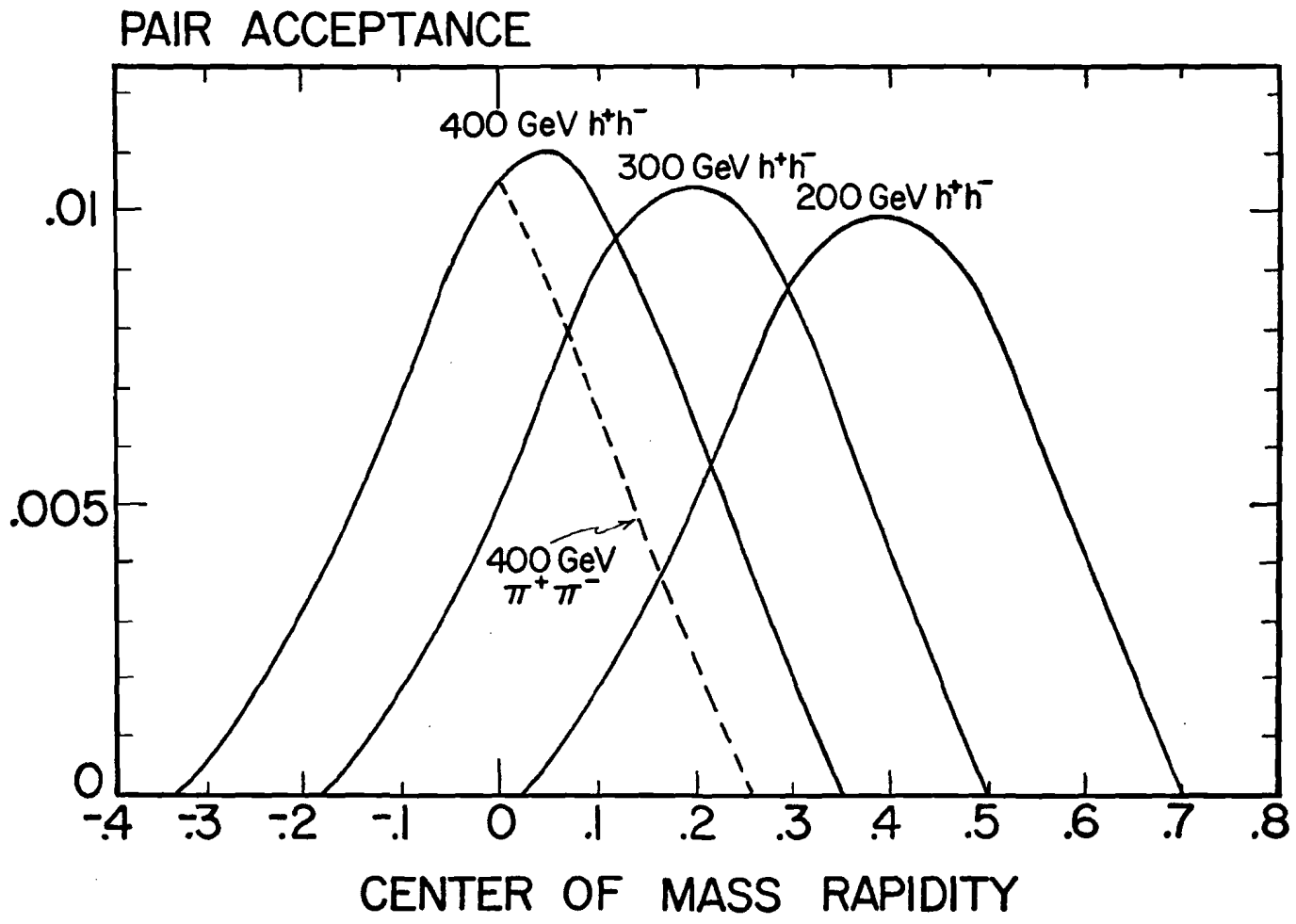
PAIR ACCEPTANCE
400 GeV h⁺h⁻
300 GeV h⁺h⁻
200 GeV h⁺h⁻
400 GeV π⁺π⁻
.01
.005
0
-.4
-.3
-.2
-.1
0
.1
.2
.3
.4
.5
.6
.7
.8
CENTER OF MASS RAPIDITY

FIGURE 45

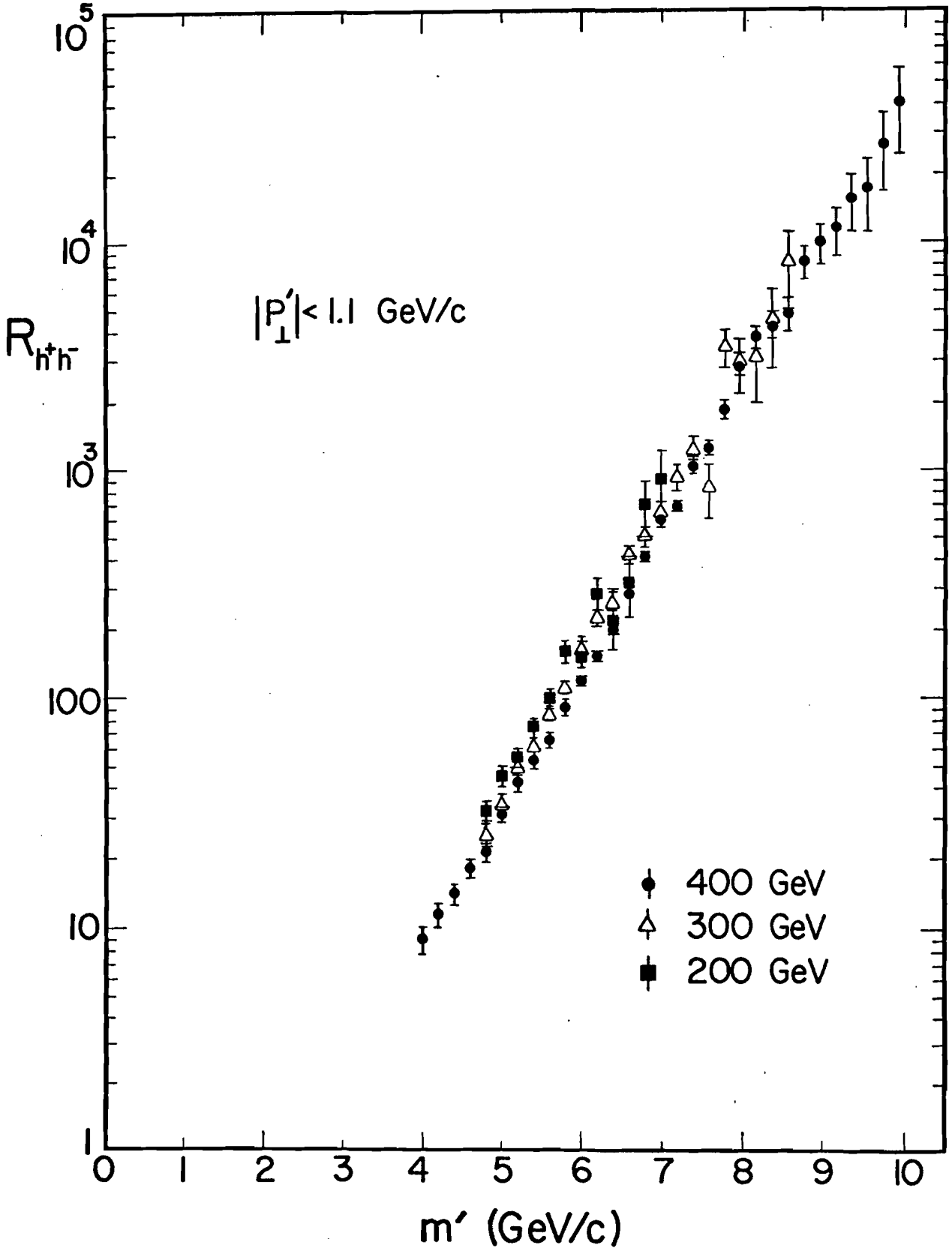
10^5
10^4
10^3
100
10
1
$R_{h^+h^-}$
$|P_\perp'| < 1.1$ GeV/c
400 GeV
300 GeV
200 GeV
0
1
2
3
4
5
6
7
8
9
10
m′ (GeV/c)

FIGURE 46

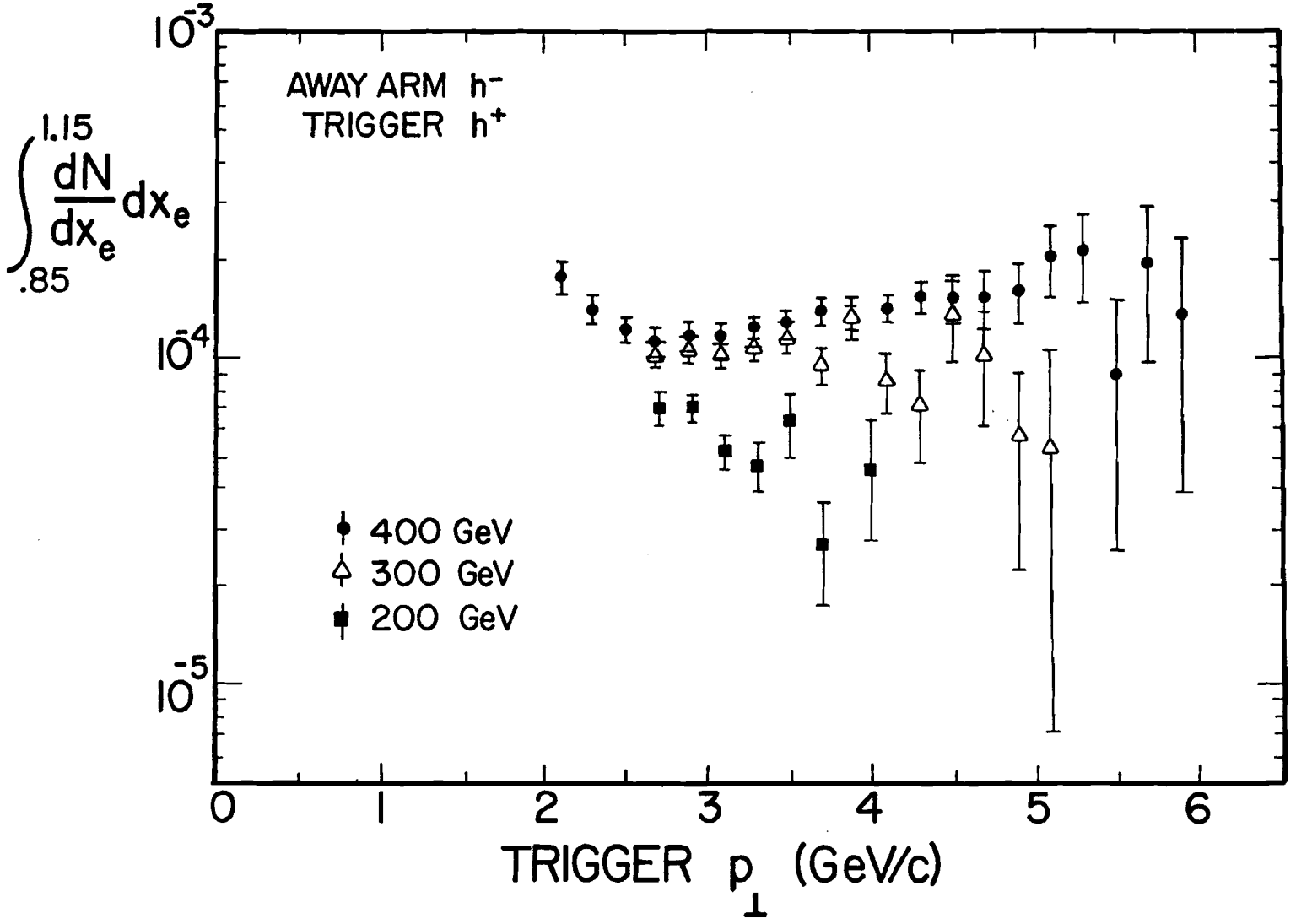
AWAY ARM h⁻
TRIGGER h⁺
$\int_{.85}^{1.15} \frac{dN}{dx_e} dx_e$
400 GeV
300 GeV
200 GeV
10^{-3}
10^{-4}
10^{-5}
0
1
2
3
4
5
6
TRIGGER $p_\perp$ (GeV/c)

FIGURE 47

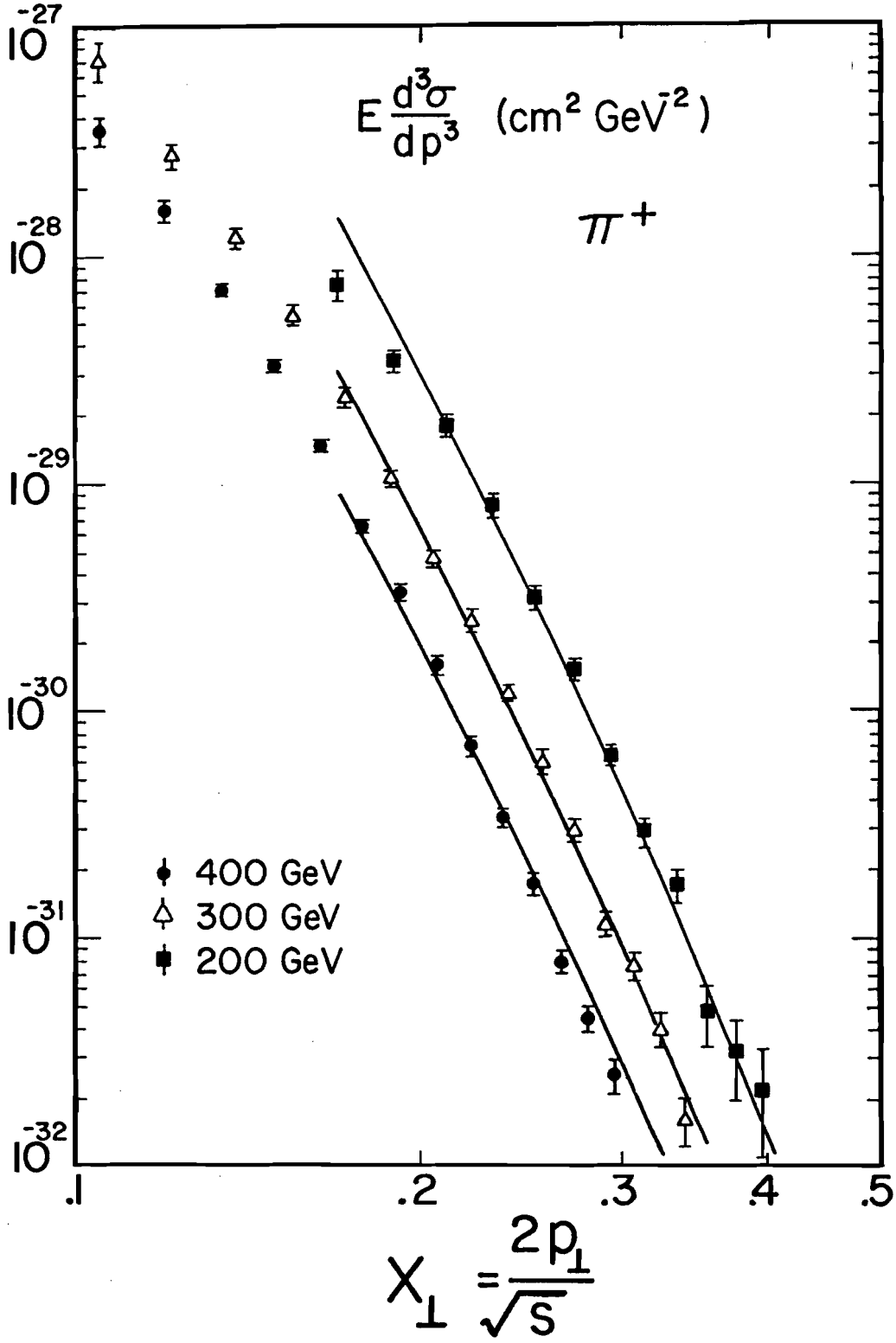
$E\frac{d^3\sigma}{dp^3}$ (cm^2 GeV^{-2})
π^+
400 GeV
300 GeV
200 GeV
10^{-27}
10^{-28}
10^{-29}
10^{-30}
10^{-31}
10^{-32}
.1
.2
.3
.4
.5
$X_\perp = \frac{2p_\perp}{\sqrt{s}}$

FIGURE 48

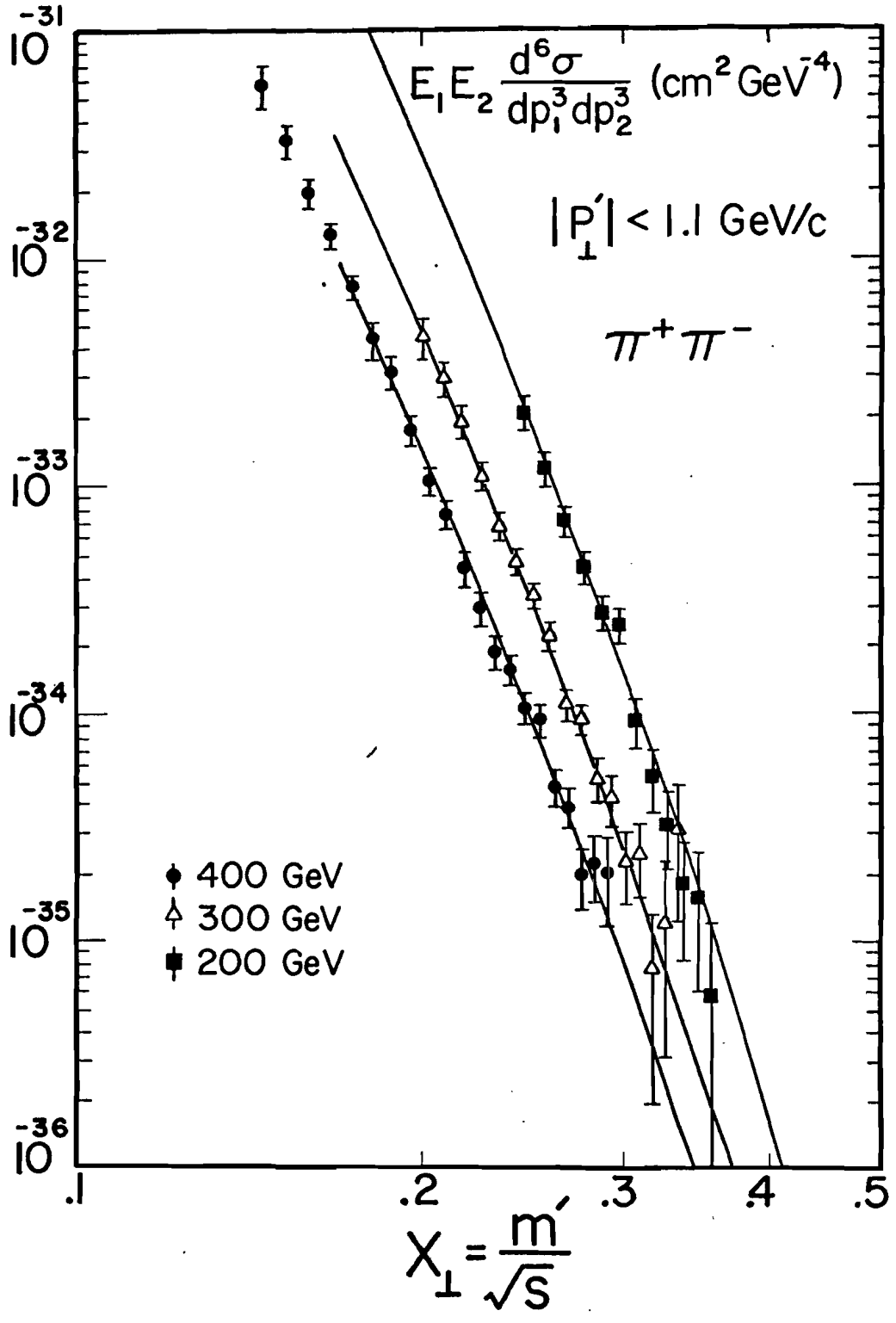
$E_1 E_2 \frac{d^6\sigma}{dp_1^3 dp_2^3}$ (cm^2 GeV^{-4})
$|P_\perp'| < 1.1$ GeV/c
$\pi^+\pi^-$
400 GeV
300 GeV
200 GeV
10^{-31}
10^{-32}
10^{-33}
10^{-34}
10^{-35}
10^{-36}
.1
.2
.3
.4
.5
$X_\perp = \frac{m'}{\sqrt{s}}$

FIGURE 49

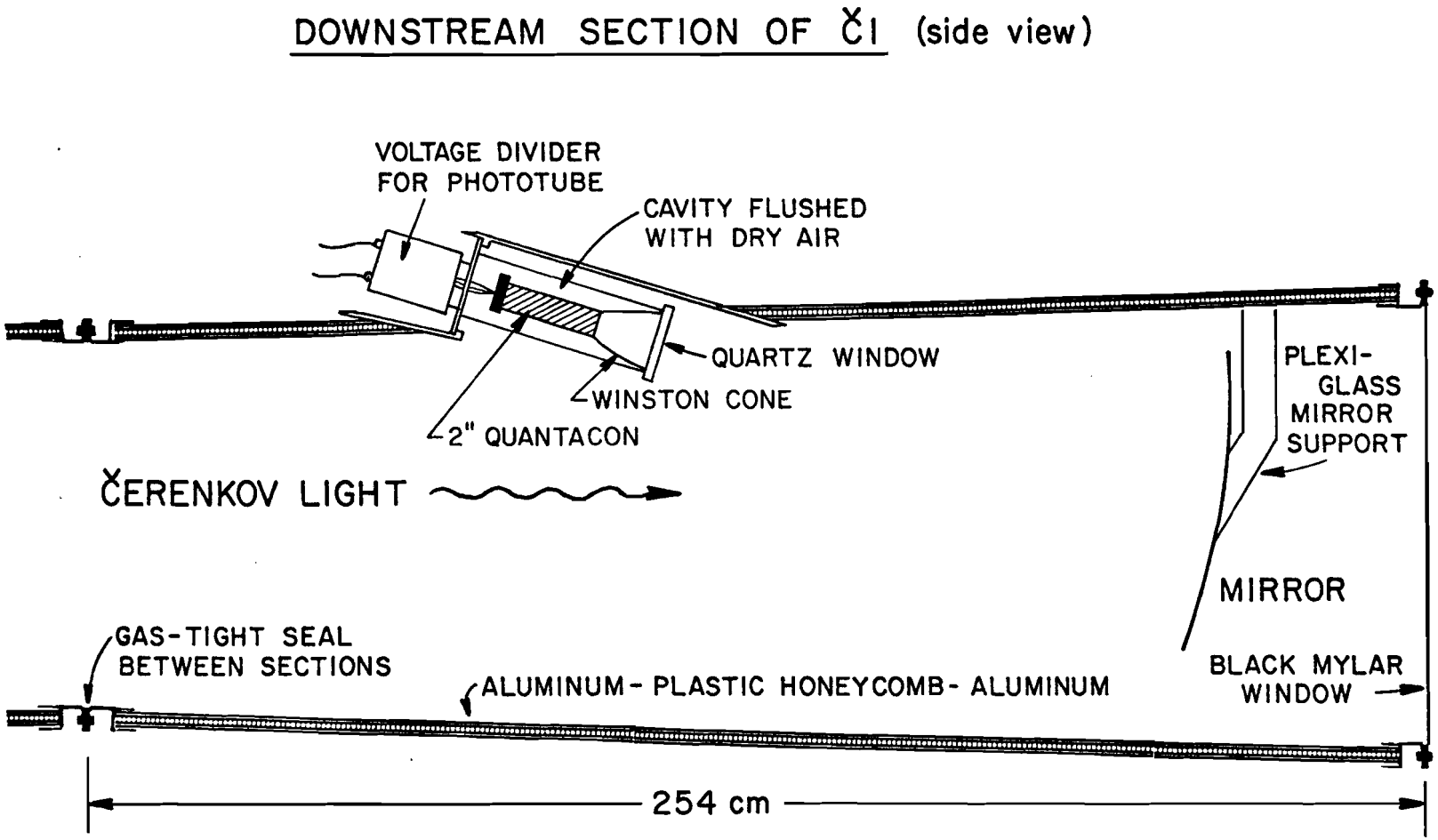
DOWNSTREAM SECTION OF ČI (side view)
VOLTAGE DIVIDER FOR PHOTOTUBE
CAVITY FLUSHED WITH DRY AIR
QUARTZ WINDOW
WINSTON CONE
2" QUANTACON
ČERENKOV LIGHT
PLEXI-GLASS MIRROR SUPPORT
MIRROR
GAS-TIGHT SEAL BETWEEN SECTIONS
ALUMINUM - PLASTIC HONEYCOMB - ALUMINUM
BLACK MYLAR WINDOW
254 cm

FIGURE 50

THE INTERFEROMETER (top view)

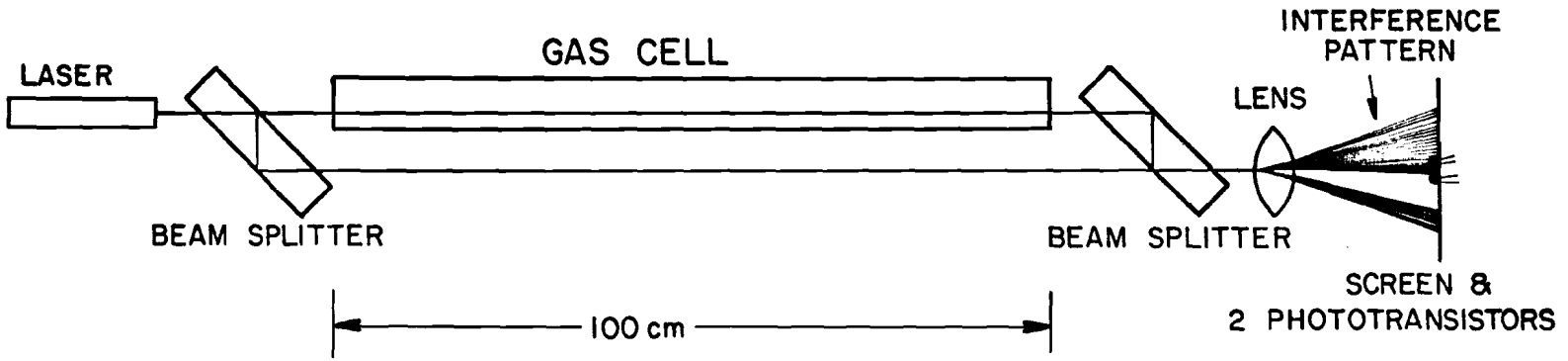

FIGURE 51